ELECTROMAGNETIC INTERFERENCE IN ELECTRONIC CIRCUITS AND SYSTEMS

by

MOHAMMAD ALI TASSOUDJI

B.S.E. Elec. Eng., University of Michigan, Ann Arbor
May 1987

M.S.E. Elec. Eng., University of Michigan, Ann Arbor
May 1989

Submitted to the Department of
Electrical Engineering and Computer Science
in Partial Fulfillment of the Requirements for the Degree of

DOCTOR OF PHILOSOPHY

at the

MASSACHUSETTS INSTITUTE OF TECHNOLOGY

May 1994

Signature of Author _____
Department of Electrical Engineering and Computer Science
May 12, 1994

Certified by _____
Professor Jin Au Kong
Thesis Supervisor

Accepted by _____
Frederic R. Morgenthaler
Chairman, Departmental Committee on Graduate Students

Eng.

ELECTROMAGNETIC INTERFERENCE IN ELECTRONIC CIRCUITS AND SYSTEMS

by

MOHAMMAD ALI TASSOUDJI

Submitted to the Department of Electrical Engineering and Computer Science
on May 12, 1994 in partial fulfillment of the requirements for the
Degree of Doctor of Philosophy

ABSTRACT

This thesis examines the effects of electromagnetic interference (EMI) and coupling in circuits and systems. The coupling phenomenon is investigated in nonuniform transmission lines and adjacent via structures in microelectronic circuits. Radiation from metallic enclosures with apertures and lined with resistive materials is analyzed. Electromagnetic interference on a larger scale is studied in the Instrument Landing System receivers, where both in–band and out–of–band interference sources are considered.

The method for modeling and analyzing vias in multilayered integrated circuits is based upon microwave network theory. The whole via structure, consisting of a vertical via passing through different layers and transitions from the microstrip lines or striplines to the vertical via, is divided into cascaded subnetworks. The parameters for each subnetwork are obtained from electromagnetic field analysis. The vertical via is modeled with equivalent magnetic frill arrays, and the transitions are characterized with the finite–difference time–domain (FD–TD) technique. For the electromagnetic coupling between two vias the even– and odd–mode approach is incorporated. Closed–form expressions for the coupled noises on the passive via are derived. Results are presented both in the frequency domain and the time domain. Validation of the model has been carried out by measurements on a 4–layer structure.

A method based on the wave transmission matrix to deal with nonuniform multiconductor transmission line systems is presented. The wave transmission matrix is employed to characterize the multiconductor transmission lines. The nonuniform

transmission line is treated as a series of many small segments of uniform transmission lines connected in cascade. The boundary conditions for linear and nonlinear terminations are derived. The formulation for this method and calculation approaches are discussed in detail. Numerical results are presented and compared of with previous work, which confirms the validity of the method.

The radiation properties of metallic enclosures are studied with a two dimensional FD–TD method. Rectangular enclosures with apertures on the walls and lined with resistive material on the inside are considered. The radiation properties of these structures are examined by varying the size and position of the holes and resistive material in the enclosure. In order to accurately model the finite conductivity of the metallic walls, an efficient formulation for including highly conducting sheets in FD–TD for a wide frequency band is derived.

The EMI phenomenon in Instrument Landing System (ILS) receivers is analyzed. The potential in–band and out–of–band interfering sources are identified. The the desired and interfering signal strengths are computed with an electromagnetic propagation model. An interference analysis based upon safety standards, consistent with the receiver model, is performed. Finally, the interference analysis results for various configurations are combined for a channel capacity assessment.

Thesis Supervisor: Professor Jin Au Kong
Professor of Electrical Engineering

ACKNOWLEDGEMENTS

I am eternally grateful to my advisor, Prof. Jin Au Kong, who has provided me with all kinds of support, without which the completion of my studies would have been impossible. His warmth, sensitivity and wisdom during our discussions and other occasions shall remain fondly appreciated.

I am deeply indebted to Bob Shin for his guidance and stimulating discussions. With his unique insight, he has guided me through my research and pushed me forward to improve every aspect of my work.

Thanks are due to Eric Yang for his advice and answering my questions on computer and other matters and also for introducing me to the world of radionavigation.

I am thankful to Prof. Steve Leeb, my thesis reader, for his suggestions and for being on my thesis and area examination committees.

I would like to express my appreciation to Qizheng Gu for giving me the opportunity to work on the modeling of via structures and multiconductor transmission lines.

I wish to thank Lars Bomholt for editing this thesis and for his invaluable comments on its presentation.

Throughout my work in Prof. Kong's research group, I have had the good fortune of being surrounded with excellent people. I thank all of you. I owe it all to you.

I am particularly thankful to Murat Veysoglu, who with his friendship and kindness tolerated my ups and downs and my frequent questions during the past five years.

Special thanks go to my mother, father and sisters for their love and support and their faith in me throughout my life.

To my sister Shohreh

Contents

List of Figures

Chapter 1

Introduction

1.1 Description of the Thesis

The subject of this thesis is the analysis of electromagnetic interference and coupling in electronic circuits and systems. All electronic and electrical equipment is a potential source of electromagnetic interference (EMI). Similarly, such equipment will not function as designed at some electromagnetic ambient. For EMI to exist there must be a source of emission, a path for the coupling of emission and a circuit unit or system sensitive to the received noise.

In electronic circuits the sources of interference are usually power lines, signal lines, and current carrying ground connections. In high speed circuits with short pulse duration and fast rise time connections can no longer be considered as conducting wires, but behave as transmission lines or waveguides. Physical discontinuities or nonuniformities in the connections cause severe emission and coupling to other parts of the circuit. High frequency analysis of these discontinuities is therefore a necessity.

Vias constitute one of the most commonly–used class of interconnects in multi-

layered integrated circuits, where they connect two conducting strips of signal line in different layers to each other. In Chapter 2 an approach of modeling these structures is presented. The whole via structure is divided into cascaded subnetworks, including a vertical via passing through different layers and transitions from the microstrip lines and/or striplines to the vertical via. The parameters of each subnetwork are obtained from electromagnetic field analysis based on geometrical layout of each part. Numerical results in the frequency domain and the time domain are analyzed and validation of the model has been carried out by both measurements and the finite–difference time–domain (FD–TD) method.

The coupling or crosstalk phenomenon of EMI for conductors in close proximity is demonstrated in nonuniform multiconductor transmission lines and adjacent via structures in microelectronic circuits. An efficient method for analyzing coupling noises on adjacent vias has been developed in Chapter 3. The analysis is based on equivalent magnetic frill array models combined with the even– and odd–mode technique. For two adjacent vias, the closed-form formulas for the reflection and the transmission on the active via and for the near–end and far–end coupled noises on the passive via are analytically derived. The validity of these formulas is confirmed by measurements on experimental models.

In very large scale integrated digital circuits and systems, multiconductor transmission lines are used as signal interconnections between chips, chip carriers, circuit boards, or subsystems. To analyze nonuniform multiconductor line system a method based on the wave transmission matrix is presented in Chapter 4. This method has not only the ability to treat nonuniformity, but also the advantage of efficiently

handling nonlinear terminations. The nonuniform transmission line is modeled as a cascade of many small segments of uniform transmission lines. The boundary conditions are formulated with linear loads in spectral domain and with nonlinear loads in time domain. Calculation approaches and numerical results are investigated and compared with previous work to confirm the validity of the method.

The use of equipment enclosures and packages to shield against emissions and external energy is a common practice. High field intensities within such enclosures will affect equipment reliability and degradation in the performance of the enclosed circuitry. Clearly this is increasingly pertinent in cases of heavy shielding where resonator–like structures with high quality factors (Q) result. Moreover, in these cases, any energy leakage may be highly frequency selective with substantial associated field strength. Chapter 5 focuses on the use of resistive material within the enclosure walls for absorbing some of contained RF energy, thereby avoiding high Q enclosures and reducing the likelihood of significant field buildup within enclosure. The energy leakage from perforations (holes, slots) on the walls is also being studied. In order to accurately model the finite conductivity of the metallic walls, an efficient formulation for including highly conducting sheets in FD–TD for a wide frequency band is derived.

In the above cases the cause of EMI problems are all within the system itself. In a large class of EMI problems, however, the interfering noise comes from an outside source. The EMI phenomenon for this type of interference in Instrument Landing System (ILS) receivers is the subject of Chapter 6. The analysis is centered around the development of a computer simulation tool for ILS electromagnetic in-

terference problems. First the potential in–band and out–of–band interfering sources are identified. The desired and interfering signal strengths are then computed using an electromagnetic propagation model. An interference analysis based upon safety standards, which are consistent with the receiver model, is performed. Finally, the interference analysis results for various configurations are combined to make a channel capacity assessment.

1.2 Background

Modeling and Analysis of Via Structures in Multilayer Integrated Circuits

In order to provide shorter interconnections between different components of a high performance computer system, modern integrated circuits have incorporated multilayer structures. The interconnects in a multilayer packages include not only conventional planar striplines and microstrip lines but vertical transmission lines or so–called vias as well. The study of signal propagation properties on vias is indispensable to the understanding of the performance of multilayer integrated circuits.

Unlike striplines and microstrip lines, vias do not have parallel ground planes to support well–guided electromagnetic waves. They usually pass through small holes in ground planes between individual layers in integrated circuits. The two ends of the via perpendicularly contact the conducting strip of the signal lines in different layers. Therefore, signal distortion is likely to occur when propagating through vias and through the transitions from vias to horizontal signal lines. In the past, vias in printed circuit boards have been analyzed using lumped element circuit models. They

provide simple and accurate predictions when the lengths of the vias are relatively short and the operating speed is low. For the analysis of high–performance integrated circuit packages, it is desirable to have a comprehensive circuit model that can handle shorter signal pulse duration and rise time and at the same time remain as simple as these empirical formulas.

Moreover, there is also emission which can couple to the adjacent via elements in the circuit. To date, the analysis of coupled noise between adjacent vias has received very little attention. The major reasons include the complexity of multi–via structures and the difficulty of modeling and analyzing them accurately over a broad frequency range.

A general three–dimensional via structure can be decomposed into planar transmission line segments such as microstrip lines and/or stripline segments, vertical via and transitions between the planar lines and the vertical via. The equivalent network of the vertical segment and the corresponding network parameters is obtained from a magnetic frill model. The analysis of adjacent vias and the corresponding formulation for the transmission and reflection on the vias are based on odd– and even–mode approach. Numerical results for several via structures with different parameters are analyzed. From these results, we can quantitatively explain how the parameters, such as spacing between the vias and the number of layers, affect the coupled noises. To validate the formulation and verify the numerical results experimental measurements have been performed and in addition, calculations using the finite–difference time–domain numerical method are made for comparison.

Analysis of Nonuniform Multiconductor Transmission Line Systems

Multiconductor transmission lines are commonly used as signal interconnections between chips, chip carriers, circuit boards, or subsystems in integrated circuits. As the operating speed of the circuits and the systems increases, the behavior of the multiconductor transmission lines employed as high speed signal carriers will have significant impact on the performance of the circuits or the systems. A multiconductor transmission line usually consists of cylindrical and/or strip conductors embedded in an inhomogeneous medium and one or several of the conductors serving as the ground. Inhomogeneous transmission lines can not support pure TEM waves but quasi–TEM waves at low frequencies. Even if the medium is homogeneous, at higher frequencies due to the conducting loss and higher order mode propagation, the lines are not TEM in nature. Since a rigorous analysis of a multiconductor transmission line is very involved, the analyses in most of previous works and in this study are based on the quasi–TEM approximation. In fact, this is a very good approximation when the transverse dimensions of the line are small as compared with the operating wavelength. In addition to simplifying the analysis of the multiconductor lines, the quasi–TEM approximation is also desired for handling the line terminations which are usually described by circuit quantities (voltages and currents) rather than by the more general field quantities. As the frequency of operation gets higher, the modes start to deviate from the quasi–TEM modes and one must analyze the problem with a rigorous full–wave approach.

The general approach on the analysis of the multiconductor line is as follows: utilizing the electromagnetic field theory to characterize the multiconductor line by

developing transmission line parameter matrices, such as the capacitance, inductance, resistance and conductance matrices per unit length of the line, and to establish a mathematical model, i.e., a set of equations governing the behavior of the line system; and then using a preferable method, for example the modal analysis, to solve the equations analytically and/or numerically and to obtain the system responses in the time and frequency domains through corresponding boundary conditions. In our study the emphasis is on analyzing the responses of the multiconductor transmission line in the frequency domain and assuming that the parameter matrices of the line are available.

When the dominant mode in the multiconductor transmission lines is quasi–TEM, the mathematical model which fully describes the line systems in the time domain or in the frequency domain is the well known telegrapher equations. For uniform multiconductor transmission lines, the corresponding telegrapher equations are most commonly solved by using the so–called modal analysis in the time domain or in the frequency domain. However, for a lossy or frequency–dependent line, usually the modal analysis in the frequency domain is used since in this case N different quasi–TEM modes propagating on a transmission line with N signal conductors and one ground conductor can only be defined in the frequency domain. In the modal analyses, the kernel of the approach is to decouple the telegrapher equations by utilizing the method of characteristics, and then based on given boundary conditions the problem can be solved. The modal analyses can not directly deal with nonuniform multiconductor line problems, but incorporating with other techniques, such as the perturbation method, it is still possible to use the modal analysis in the time do-

main for some nonuniform systems. However, the more efficient method for handling the nonuniform transmission lines are the network matrix parameter methods in the frequency domain. In our study the wave transmission matrix is employed to characterize the multiconductor transmission lines and the telegrapher equations, therefore, can easily be turned into algebraic equations. The nonuniform transmission line is treated as many small segments of uniform transmission lines connected in cascade. The boundary conditions are formulated with linear loads in spectral domain and with nonlinear loads in time domain.

Electromagnetic fields in Metallic Enclosures Lined with Resistive Material

The use of equipment enclosures to shield against emissions and external energy is a common practice. The motivation for studying such structures is that computers are now operating at faster speeds and consuming more power resulting in significantly increased levels of power at higher frequencies. Also typical metallic enclosure configurations have dimensions which are electrically resonant at frequencies in the hundreds of megahertz range. Any energy leakage from these structures may be highly frequency selective with substantial associated field strength.

The study on metallic enclosures focuses on the use of resistive material within the enclosure walls for absorbing some of contained RF energy, thereby avoiding high Q enclosures and reducing the likelihood of significant field buildup within enclosure. The energy leakage from perforations (holes, slots) on the walls is also being studied. The radiation properties of these structures are examined by varying the size and

position of the holes in the enclosure.

One of the goals of this study is to determine the efficiency and effect of resistive material in lowering the energy leakage of the metallic enclosures and observing their resonant behavior. Another goal is to investigate the effect of perforations in the enclosure by varying their size and location. The method employed in the analysis is the finite–difference time–domain technique. The reasons this technique was selected include the relative ease of implementation for complicated geometries with dielectrics, the requirement of only simple arithmetic operations in the solution process, and the flexibility for time– and frequency–domain analyses. It is based on discretization of electric and magnetic fields over rectangular grids together with the finite difference approximation of the spatial and temporal derivatives appearing in the differential form of Maxwell's equations.

Analysis of Electromagnetic Interference to Airborne ILS Receivers

ILS is the current navigational landing system used in the United States and internationally. It was developed in the 1940's and has been the standard precision–approach guidance system used by the airline carriers as well as general aviation community all over the world. In the United States, there are currently nearly 1000 civilian runways that are fully or partially equipped with ILS. However, the rapid growth of air travel in recent years has far strained the system capacity. Studies and actual assignment efforts have indicated that there is a potential frequency congestion problem.

Frequency congestion of and interference with the ILS frequency band is a growing problem for the FAA as more navigational and non–navigational facilities are

being installed. It is becoming increasingly difficult for the FAA to conduct adequate ILS frequency management and assign new frequency channels that are suitable for precision landing purposes. In the past, through careful frequency management the FAA has avoided serious ILS congestion problems.

The out–of–band interference is a serious problem for the ILS because of heavy aviation and commercial usage around the localizer frequencies (near 100 MHz). Many industrial and scientific machineries are able to generate electromagnetic noise in this band; however, the most significant source is from commercial FM broadcasting stations.

In the U.S., the FM broadcast band is allocated between 88 and 108 MHz, the high–end of which is next to the ILS localizer frequencies. Therefore, no guard–band is provided for localizer protection. It is very difficult to have significant rejection capability built into the RF front–end of ILSs receivers. FM broadcasting stations have the highest density near major metropolitan areas, which also happen to have the highest density of airports and runways. Therefore, the possibility of multiple FM broadcasting transmitters falling right within the service volumes of an ILS is very high. Owing to Federal deregulation policy, FM broadcasting stations are encouraged to transmit at the highest power output of their respective licensing classes. The highest power level is usually on the order of 10 to 100 kW, which is several orders of magnitude higher than the localizer power, typically around 15 W. The above factors help explain why pilots occasionally observe that ILS receivers are easily overwhelmed by the FM power and rendered inoperable.

The objectives of this study is to develop a computer simulation tool for ILS

to: perform quantitative analyses of in–band (aviation band) and out–of–band electromagnetic interferences; make quantitative assessments of electromagnetic interferences within the ILS service volume, and predict channel capacities of ILS in congested geographical area.

Chapter 2

Modeling of a Single Via in Multilayered Integrated Circuits

2.1 Introduction

In order to provide shorter interconnections between different components of a high performance computer system, modern integrated circuits have incorporated multilayer structures. The interconnects in a multilayer package include not only conventional planar striplines and microstrip lines but vertical transmission lines or so–called vias as well. For example, in the Thermal Conduction Module (TCM) for IBM 3081 and 3090 series computers, the number of vias is rather significant compared to the number of planar interconnects. Therefore, the study of signal propagation properties on vias is indispensable to the understanding of the performance of multilayer integrated circuits.

Unlike striplines and microstrip lines, vias do not have parallel ground planes to support well–guided electromagnetic waves. They usually pass through small holes in ground (or reference) planes between individual layers in integrated circuits. The

two ends of the via perpendicularly contact the conducting strip of the signal lines in different layers as shown in Figure 2.1(a). Therefore, signal distortion is likely to occur when propagating through vias and through the transitions from vias to horizontal signal lines. In the past, vias in printed circuit boards have been analyzed using lumped element circuit models. In [1], the partial electric element circuit (PEEC) model developed by Ruehli [2] was applied to find the inductance of a short flat via connecting two striplines. More recently, integral–equation formulations for quasi–static analysis of various via geometries have been developed [3, 4]. Others [5, 6] use empirical formulas to construct equivalent circuits, which may include transmission line elements. Most of the formulas are only effective at low frequencies. They provide simple and accurate predictions when the lengths of the vias are relatively short and the operating speed is low. For the analysis of high–performance integrated circuit packages, it is desirable to have a comprehensive circuit model that can handle shorter signal pulse duration and rise time and at the same time remain as simple as these empirical formulas.

In this chapter an equivalent network model (NW model) for the single via structure is developed. The network is constructed from several subnetwork elements corresponding to different parts of the via structure connected in cascade. Assuming that the transition between these subnetworks are coaxial segments that only support TEM mode, we are able to cascade these two–port subnetworks. The parameters of the subnetworks are obtained by electromagnetic analysis based on the geometrical layout of each part. By dividing the structure into subnetworks, any modification in the circuit geometry can be easily incorporated in the corresponding subnetwork.

In Section 2.2 the groundwork for constructing an equivalent network of via structures is described. A general three–dimensional via structure can be decomposed into planar transmission line segments such as microstrip lines and/or stripline segments, vertical via and transitions between the planar lines and the vertical via. The analysis of the vertical via will be emphasized in this chapter. The equivalent network of the vertical segment and the corresponding network parameters obtained from a magnetic frill model are discussed in detail in Section 2.3. Based on the analytical formulas developed in Section 2.3, transmission and reflection properties of a single layer via and multilayer vias are analyzed. In Section 2.4 the results are presented and compared with the finite–difference time–domain (FD–TD) numerical method and measurements. The transition from transmission line to vertical via is addressed in Section 2.5. In Section 2.6, the propagation characteristics of the entire via structure is described in the frequency and the time domains.

2.2 Modeling as Equivalent Networks

The via structure shown in Figure 2.1(a) consists of a multilayer substrate with embedded ground planes and microstrip lines on the top and bottom layers connected through the vertical via, which is a cylindrical conductor passing through circular holes in the ground planes. This via structure can be decomposed into subsections. These are the microstrip lines, transitions and the vertical via as shown in Figure 2.1(b). Each of them can be considered as a two-port network and described by a 2×2 matrix. As seen in Figure 2.1(b) all the two-port subnetworks are connected in cascade, therefore it will be convenient to use the wave transmission matrix

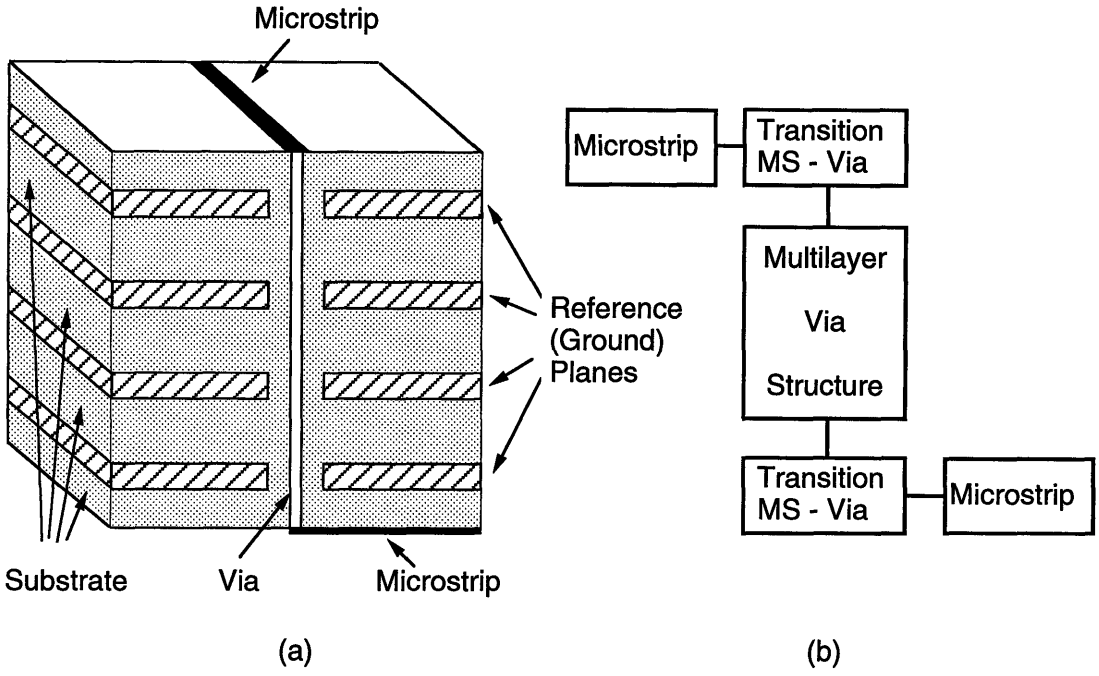

Figure 2.1: Configuration and constitution of via structure.

$[A_i]$ to represent each of these subnetworks. The matrix expression for the entire via structure is simply the product of the matrices $[A_i]$,

$$[A] = [A_1][A_2]...[A_i]...[A_n]. \tag{2.1}$$

For example, the via structure in Figure 2.1(b) may be characterized by

$$\begin{bmatrix} A_{11} & A_{12} \\ A_{21} & A_{22} \end{bmatrix} = \begin{bmatrix} A_{11T} & A_{12T} \\ A_{21T} & A_{22T} \end{bmatrix}_{MS-V} \begin{bmatrix} A_{11V} & A_{12V} \\ A_{21V} & A_{22V} \end{bmatrix} \begin{bmatrix} A_{11T'} & A_{12T'} \\ A_{21T'} & A_{22T'} \end{bmatrix}_{V-MS} \tag{2.2}$$

where $[A_T]_{MS-V}$ and $[A_{T'}]_{V-MS}$ are the wave transmission matrices of the transition from the microstrip line to via, and vice versa, and $[A_V]$ is the wave transmission matrix of the vertical via.

As will be seen in Section 2.3, the vertical via segment can be further decom-

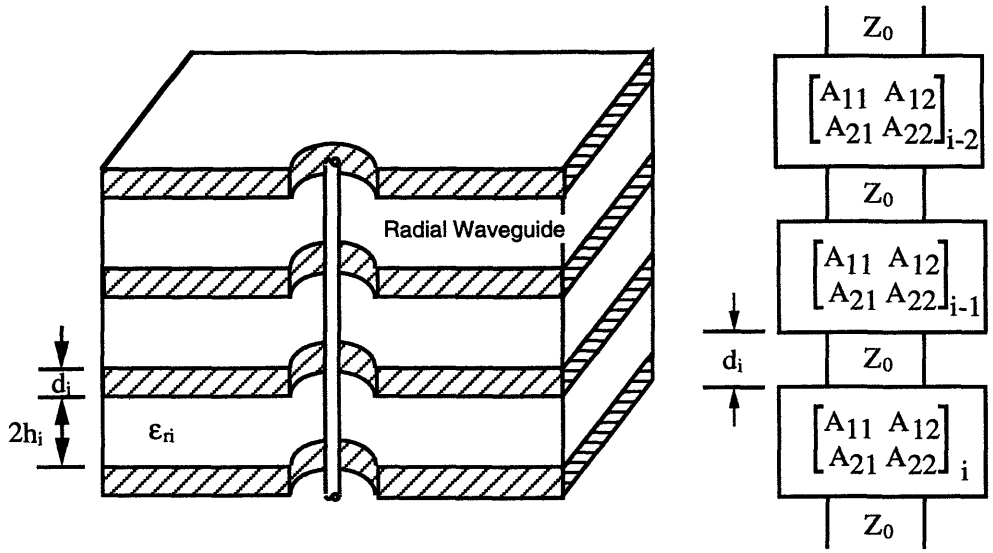

Figure 2.2: The vertical via and its equivalent network model.

posed into subnetworks. The flexibility of such a modeling scheme enables one to implement any variation in the structure by modifying the appropriate subnetwork. This is in contrast with other methods such as full-wave analysis or FD–TD which requires the re-formulation or re-calculation of the overall structure whenever there is a variation in the original structure.

2.3 Analysis and Modeling of the Vertical Via

The vertical part of the via structure is isolated in Figure 2.2(a). Under the assumption that the ground planes have finite thickness, the vertical via is considered to consist of coaxial line segments and radial waveguides. The equivalent network is shown in Figure 2.2(b). Since the spacing between the ground planes and the

dielectric substrates in each layer are not necessarily the same, every matrix in the network model is not identical. The impedance of each coaxial line segment also varies in accordance with the diameter of the holes in the ground planes and the filling material.

The network parameters or the elements of the wave transmission matrix $[A_i]$ in the model are based upon the analysis of a basic unit in the multilayer vertical via as shown in Figure 2.3(a). In essence this is a one layer via with coaxial line segments on its ends. To facilitate the analysis, the coaxial line segments are assumed to be extended to infinity. The equivalent circuit for the single layer via as shown in Figure 2.3(b) is modeled as a π type network in order to exploit the symmetry of the structure. Since the configuration of Figure 2.3(a) is symmetric about the mid-plane M, the elements in the π network can be obtained by analyzing the half structures resulting from placing ideal electric and magnetic walls in turn on the plane M.

In the case of an electric wall placed on the plane M, the resulting configuration as shown in Figure 2.4(a) is equivalent to a parallel-plate antenna. The corresponding circuit representation is the original π network short-circuited in the middle as depicted in Figure 2.4(b). The admittance Y_{sc} at plane A observed from the coaxial line side is the same as the input admittance of a parallel-plate antenna. Otto [10] derived the input admittance of the parallel-plate antenna by using a frill model of magnetic current neglecting the effect of TM modes in the coaxial line. The following is a brief description of the magnetic frill model to obtain the admittance Y_{sc}. Here the radii of the via and the via hole in the ground plane are a and b respectively, and the separation between the ground plane and the electric wall is h. Initially,

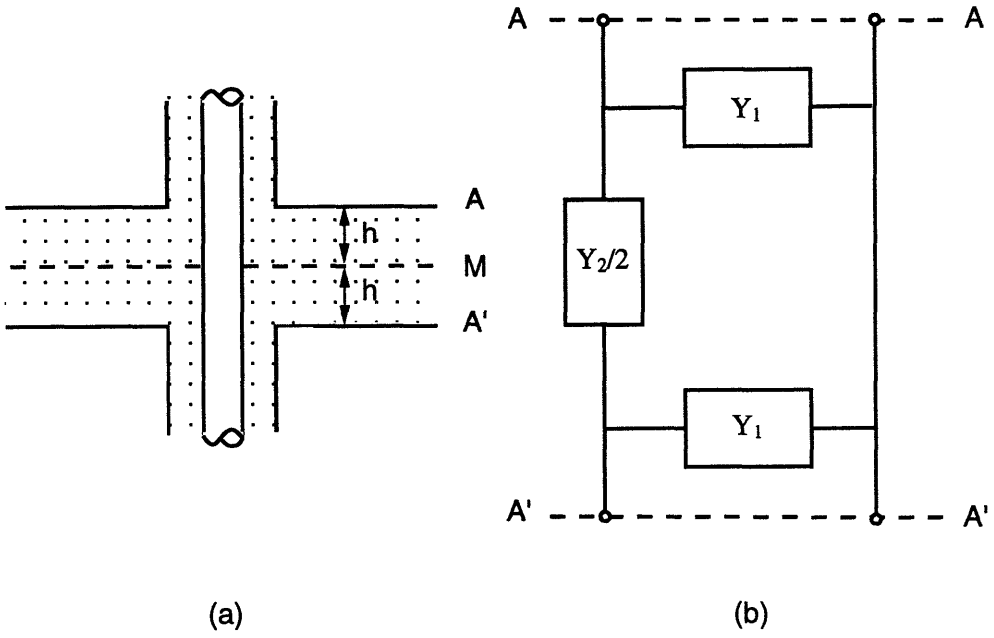

Figure 2.3: Basic unit in multilayer via and its equivalent network.

a semi-infinite rod antenna fed by a coaxial line is considered. The radius of the inner conductor is a, same as the rod, and the outer radius is b. By virtue of the equivalence principle the semi-infinite perfectly conducting rod, which represents the via conductor, is excited by a frill of magnetic current $M_0(z) = M_0\delta(z)$. The frill of magnetic current M_0 is located at the aperture where the coaxial line passes through the ground plane and has the form

$$M_0 = \begin{cases} -\dfrac{2V}{r\ln(b/a)} & a \le r \le b \\ 0 & \text{elsewhere} \end{cases} \tag{2.3}$$

where V is the voltage at the aperture ($z = 0$) on the coaxial line and is usually considered as a known excitation. Using image theory, the structure can be transformed into a periodic array of magnetic frills M_0 located at $z = \pm 2mh$ ($m = 0, 1, 2, ...$), with the parallel plates removed, as depicted in Figure 2.4(c). Mathematically it can be

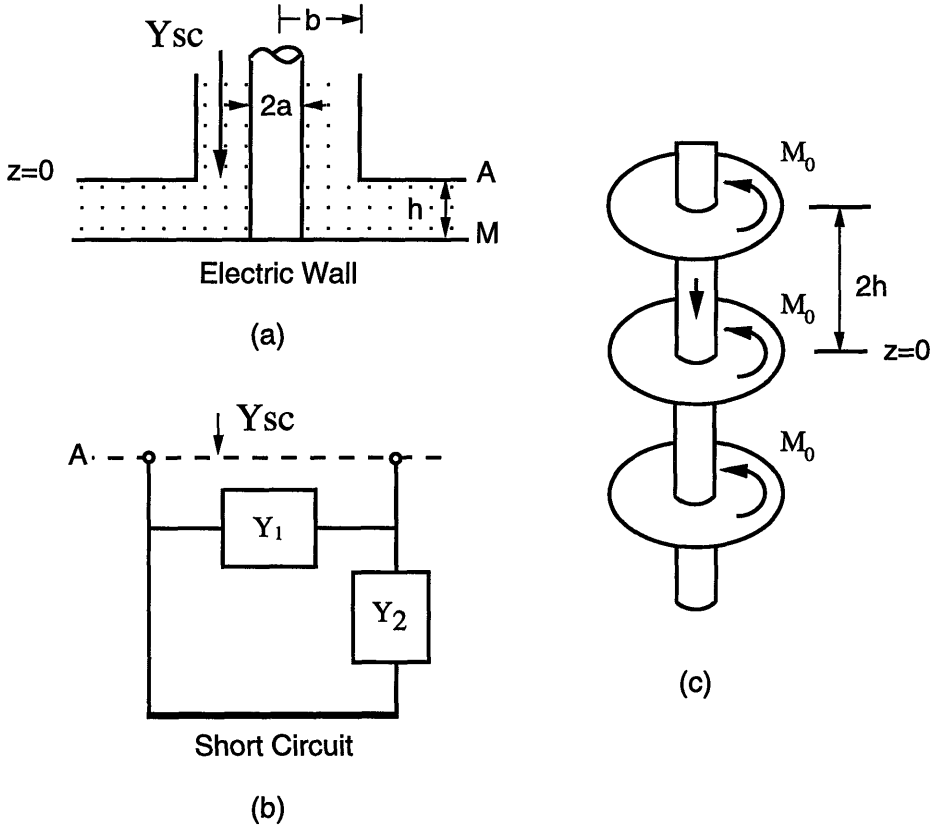

Figure 2.4: Configuration for an electric wall placed on plane M and its equivalent and magnetic frill array model. (a) Configuration, (b) equivalent circuit and (c) magnetic frill array model.

expressed as

$$M_{sc}(z, 2h) = \sum_{m=-\infty}^{+\infty} M_0 \delta(z - m(2h)). \tag{2.4}$$

Using the integral representation of input admittance of infinitely-long cylindrical antenna and the concept of periodic frill array, the complex input admittance of

the parallel plate antenna or Y_{sc} can be derived and has the form

$$Y_{sc} = -\frac{2\pi j\sqrt{\epsilon_r}}{\eta_0 \ln(\frac{b}{a})}\cot(kh) - \frac{2\pi j\sqrt{\epsilon_r}}{\eta_0 k\, h[\ln(\frac{b}{a})]^2}\left\{\frac{\pi}{2}\frac{H_0^{(2)}(kb)}{H_0^{(2)}(ka)}[J_0(kb)Y_0(ka) - J_0(ka)Y_0(kb)]\right.$$
$$\left. -2\sum_{m=1}^{\infty}\frac{1}{q_m^2}\left[\frac{K_0(q_m kb)}{K_0(q_m ka)}\left(I_0(q_m ka)K_0(q_m kb) - I_0(q_m kb)K_0(q_m ka)\right)\right]\right\} \qquad (2.5)$$

where k is the wavenumber, ϵ_r is the relative dielectric constant of the filling material, and J_0, Y_0, I_0, K_0 and $H_0^{(2)}$ are Bessel functions, modified Bessel functions and Hankel function of the second kind, respectively. Also

$$q_m = \sqrt{\left(\frac{m\pi}{kh}\right)^2 - 1} \qquad (2.6)$$

and $\eta_0 = \sqrt{\frac{\mu_0}{\epsilon_0}}$, the intrinsic impedance of free space.

The expression (2.5) is slightly different from that found in [10]. The following identity [11] is used to simplify one of the series sum,

$$1 - 2\sum_{m=1}^{\infty}\frac{1}{q_m^2} = kh\cot(kh).$$

From the equivalent network of Figure 2.4(b), it is apparent that the admittance Y_{sc} can be expressed in terms of the elements Y_1 and Y_2 as

$$Y_{sc} = Y_1 + Y_2. \qquad (2.7)$$

The configuration for a magnetic wall replacing the electric wall at the plane M is shown in Figure 2.5(a). The corresponding equivalent circuit is an open-circuit

network (Figure 2.5(b)). The admittance Y_{oc} at $z = 0$ looking from the coaxial side can be determined in a similar manner as for Y_{sc}. By the image theory, the equivalent periodic frill array model now consists of alternating magnetic current frills, as shown in Figure 2.5(c). The mathematical expression of this frill array is

$$\begin{aligned} M_{oc} &= \sum_{m=-\infty}^{\infty} (-1)^m M_0 \delta\left(z - m(2h)\right) \\ &= \sum_{l=-\infty}^{\infty} M_0 \delta\left(z - 2l(2h)\right) - \sum_{l=-\infty}^{\infty} M_0 \delta\left(z - (2l+1)(2h)\right) \\ &= 2\sum_{l=-\infty}^{\infty} M_0 \delta\left(z - l(4h)\right) - \sum_{m=-\infty}^{\infty} M_0 \delta\left(z - m(2h)\right). \end{aligned} \tag{2.8}$$

Comparing (2.8) with (2.4), the frill array $M_{oc}(z, 2h)$ can be decomposed into two equivalent short-circuit frill arrays with a common excitation voltage at $z = 0$ but spacings of $4h$ and $2h$, respectively. Equation (2.8) can then be expressed as

$$M_{oc}(z, 2h) = 2M_{sc}(z, 4h) - M_{sc}(z, 2h). \tag{2.9}$$

Since the voltage at $z = 0$ is a known excitation, the admittance Y_{oc} is directly proportional to the current at $z = 0$ flowing on the inner conductor of the coaxial line. The current at $z = 0$ can be obtained from the equivalent magnetic frill array M_{oc}, and because of linearity is the superposition of the currents induced by the equivalent short-circuit frill arrays $2M_{sc}(z, 4h)$ and $M_{sc}(z, 2h)$. Thus Y_{oc} can also be expressed as the superposition of short-circuit admittances

$$Y_{oc} = 2Y'_{sc} - Y_{sc} \tag{2.10}$$

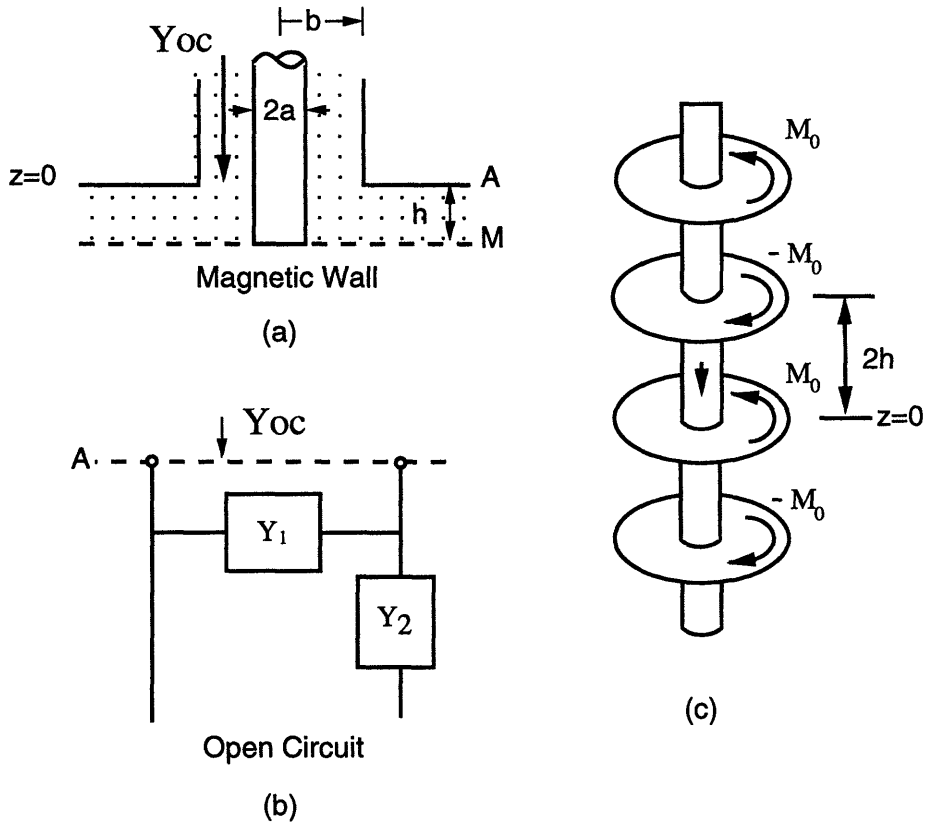

Figure 2.5: Configuration for a magnetic wall placed on plane M and its equivalent and magnetic frill array model. (a) Configuration, (b) equivalent circuit and (c) magnetic frill array model.

where Y_{sc} is given by (2.5) and Y'_{sc} is a short-circuit admittance corresponding to the inner conductor terminated by electric wall with separation $2h$ instead of h. Y'_{sc} can further be written in the form of

$$\begin{aligned} Y'_{sc} &= -\frac{2\pi j\sqrt{\epsilon_r}}{\eta_0 \ln(\frac{b}{a})}\cot(2kh) \\ &\quad -\frac{\pi j\sqrt{\epsilon_r}}{\eta_0 k\, h[\ln(\frac{b}{a})]^2}\left\{\frac{\pi}{2}\frac{H_0^{(2)}(kb)}{H_0^{(2)}(ka)}[J_0(kb)Y_0(ka) - J_0(ka)Y_0(kb)]\right. \\ &\quad -2\sum_{l=1}^{\infty}\left[\frac{1}{q_{2l-1}^2}\frac{K_0(q_{2l-1}kb)}{K_0(q_{2l-1}ka)}\left(I_0(q_{2l-1}ka)K_0(q_{2l-1}kb) - I_0(q_{2l-1}kb)K_0(q_{2l-1}ka)\right)\right. \\ &\quad \left.\left.+\frac{1}{q_{2l}^2}\frac{K_0(q_{2l}kb)}{K_0(q_{2l}ka)}\left(I_0(q_{2l}ka)K_0(q_{2l}kb) - I_0(q_{2l}kb)K_0(q_{2l}ka)\right)\right]\right\}, \end{aligned} \tag{2.11}$$

where

$$q_l = \sqrt{\left(\frac{l\pi}{2kh}\right)^2 - 1}.$$

Substituting (2.5) and (2.11) into (2.10), and with $2\cot(2\theta) = \cot\theta - \tan\theta$, the following form of admittance Y_{oc} is obtained

$$\begin{aligned} Y_{oc} &= 2Y'_{sc} - Y_{sc} \\ &= \frac{2\pi j\sqrt{\epsilon_r}}{\eta_0 \ln(\frac{b}{a})}\tan(kh) + \frac{4\pi j\sqrt{\epsilon_r}}{\eta_0 k\, h[\ln(\frac{b}{a})]^2} \\ &\quad \cdot\left\{\sum_{n=0}^{\infty}\frac{1}{q_n^2}\frac{K_0(q_nkb)}{K_0(q_nka)}\left[I_0(q_nka)K_0(q_nkb) - I_0(q_nkb)K_0(q_nka)\right]\right\}, \end{aligned} \tag{2.12}$$

where

$$q_n = \sqrt{\left(\frac{(2n+1)\pi}{2kh}\right)^2 - 1}. \tag{2.13}$$

The first terms in (2.5) and (2.12) are recognized as the input admittances of the coaxial line TEM mode; the other terms in these two equations are related to radial waveguide modes.

It is evident from the equivalent network Figure 2.5(b) that Y_{oc} is equal to element Y_1, i.e.,

$$Y_1 = Y_{oc} \tag{2.14}$$

By substituting (2.14) into (2.7), Y_2 can be written as

$$Y_2 = Y_{sc} - Y_{oc}. \tag{2.15}$$

From (2.14), (2.15) and network theory, the admittance matrix of the π-network of Figure 2.3(b) is

$$\begin{bmatrix} Y_{11} & Y_{12} \\ Y_{21} & Y_{22} \end{bmatrix} = \begin{bmatrix} Y_1 + \frac{Y_2}{2} & -\frac{Y_2}{2} \\ -\frac{Y_2}{2} & Y_1 + \frac{Y_2}{2} \end{bmatrix} = \begin{bmatrix} \frac{Y_{sc}+Y_{oc}}{2} & -\frac{Y_{sc}-Y_{oc}}{2} \\ -\frac{Y_{sc}-Y_{oc}}{2} & \frac{Y_{sc}+Y_{oc}}{2} \end{bmatrix} \tag{2.16}$$

and its corresponding wave transmission matrix is

$$\begin{bmatrix} A^s_{11V} & A^s_{12V} \\ A^s_{21V} & A^s_{22V} \end{bmatrix} = \frac{1}{\overline{Y}_{sc} - \overline{Y}_{oc}} \begin{bmatrix} 1 + \overline{Y}_{sc} + \overline{Y}_{oc} + \overline{Y}_{sc}\overline{Y}_{oc} & -1 + \overline{Y}_{sc}\overline{Y}_{oc} \\ 1 - \overline{Y}_{sc}\overline{Y}_{oc} & -1 + \overline{Y}_{sc} + \overline{Y}_{oc} - \overline{Y}_{sc}\overline{Y}_{oc} \end{bmatrix} \tag{2.17}$$

where

$$\overline{Y}_{sc} = \frac{Y_{sc}}{Y_0} \quad \text{and} \quad \overline{Y}_{oc} = \frac{Y_{oc}}{Y_0} \tag{2.18}$$

and Y_0 is the characteristic admittance of the coaxial line.

The wave transmission matrix in Equation (2.17) characterizes a single layer vertical via. In the case of an n-layer via as depicted in Figure 2.2(a), the wave transmission matrix takes the form

$$\begin{bmatrix} A_{11V} & A_{12V} \\ A_{21V} & A_{22V} \end{bmatrix} = \begin{bmatrix} A_{11C} & A_{12C} \\ A_{21C} & A_{22C} \end{bmatrix}_1 \prod_{i=1}^{n} \left\{ \begin{bmatrix} A^s_{11V} & A^s_{12V} \\ A^s_{21V} & A^s_{22V} \end{bmatrix}_i \begin{bmatrix} A_{11C} & A_{12C} \\ A_{21C} & A_{22C} \end{bmatrix}_{i+1} \right\}. \tag{2.19}$$

The $[A^s_V]_i$ $(i = 1, 2, ..., n)$ have the same form as (2.17) with the parameters $\overline{Y}_{sc,i}$ and $\overline{Y}_{oc,i}$ depend on the dimensions and properties of layer i, and $[A_C]_l$ $(l = 1, 2, ..., n+1)$ is the wave transmission matrix of the lth segment of the coaxial line,

$$[A_C]_l = \begin{bmatrix} e^{j\theta_l} & 0 \\ 0 & e^{-j\theta_l} \end{bmatrix}. \tag{2.20}$$

In (2.20) the elements are normalized to the corresponding characteristic impedance of the coaxial line. θ_l is the electrical length of the lth segment

$$\theta_l = \frac{2\pi}{\lambda_{gl}} d_l \tag{2.21}$$

where λ_{gl} is the guide wavelength in the lth coaxial line segment and d_l is its physical length.

For a uniform vertical via in which the dimensions and filling material of each

layer as well as all the segments of the coaxial line are identical, i.e., $\theta_l = \theta$, expression (2.19) becomes

$$\begin{bmatrix} A_{11V} & A_{12V} \\ A_{21V} & A_{22V} \end{bmatrix} = \begin{bmatrix} e^{j\theta/2} & 0 \\ 0 & e^{-j\theta/2} \end{bmatrix} \begin{bmatrix} A^s_{11V}e^{j\theta} & A^s_{12V} \\ A^s_{21V} & A^s_{22V}e^{-j\theta} \end{bmatrix}^n \begin{bmatrix} e^{j\theta/2} & 0 \\ 0 & e^{-j\theta/2} \end{bmatrix} \tag{2.22}$$

Once the total transmission matrix $[A_V]$ has been calculated, the reflection coefficient Γ_v and the transmission coefficient T_v at the input of the vertical via are

$$\Gamma_v = S^v_{11} = \frac{A_{21V}}{A_{11V}}, \tag{2.23}$$

and

$$T_v = S^v_{21} = \frac{1}{A_{11V}}. \tag{2.24}$$

So far, the analysis has been performed in the frequency domain. The reflected and transmitted time domain waveforms of a pulse signal propagating through the via can be obtained by means of Fourier transform.

2.4 Numerical and Experimental Validation

The network model of the vertical via portion of the structure presented in the previous section is obtained by neglecting the effect of TM modes in the coaxial line. Furthermore, the length of the coaxial line segments in the multilayer via is considered in the limiting case where it becomes zero. Under these assumptions, the NW model has been validated with experimental measurements and the finite-difference

time-domain numerical calculation.

The initial validation is for the case of a single layer vertical via, fed and terminated by a coaxial line as illustrated in Figure 2.3. The dimensions and the filling dielectric material correspond to realistic via structures in integrated circuits and are based on the ease of constructing the experimental model. The radius of the via which equals the inner conductor of the coaxial line is $a = 0.457$ mm, the radius of the apertures in the ground planes and also the outer radius of the coaxial line is $b = 1.524$ mm. The spacing between two ground planes is $2h = 1.524$ mm, and the relative permittivity ϵ_r of the filling material is 2.2. Due to the symmetry of the vertical via, its properties can solely be characterized by the reflection coefficient S_{11}^v and the transmission coefficient S_{21}^v. The magnitudes of S_{11}^v and S_{21}^v, for a single layer vertical via with the above dimensions and filling material, calculated using (2.5), (2.12), (2.17), (2.23), and (2.24) are presented in Figure 2.6 with solid lines.

An experimental model was built from RT/Duroid 5880 laminate and 141 ISO-CORE semi-rigid cable. The laminate board was cut to a size of 152.4 mm by 101.6 mm. A through hole with a diameter of 0.914 mm was made in the middle of the board. Circular pads centered at the through hole on both sides of the board with diameter of 3.048 mm were etched. A 15 cm long coaxial cable was used. Its outer conductor and dielectric on half of the cable was extracted. The other half with the inner conductor was passed through the via hole of the board. The outer portion was then placed back on the inner conductor that was extended from the laminate board. The outer conductors of the cable were then soldered to the copper on both sides of the RT/Duroid. SMA connectors were used at the ends of the semi-rigid

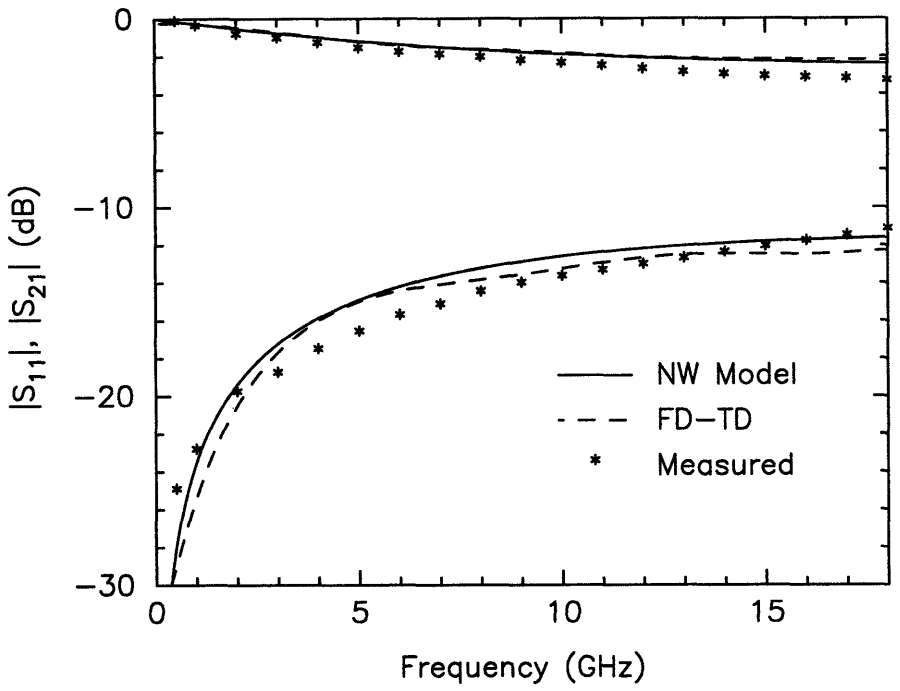

Figure 2.6: $|S_{11}|$ and $|S_{21}|$ of the single layer vertical via.

cable. Since the performance of the cable and connectors is good up to 18 GHz, this frequency range was chosen for the measurements. The results for transmission and reflection are shown in Figure 2.6 with asterisks. A good agreement between the calculated results obtained from the formulas given in Section 2.3 and the measurements is observed. In the experiment, the HP 8510B network analyzer system was used to measure the S parameters.

For further validation of the NW model the finite-difference time-domain (FD–TD) technique [12] is used to indirectly calculate the reflection and transmission coefficients. A second order absorbing boundary condition derived by Engquist and Majda [13] is used. In the FD–TD calculation, rectangular grids are employed, hence a coaxial line with square cross-section is used instead of a circular coaxial line. The inner conductor of the square coaxial line has a 0.914 mm by 0.914 mm cross-section,

and the inside dimension of the outer conductor is 2.743 mm by 2.743 mm. The filling material of the cable has a relative permittivity of 2.1. Using the approximate formula for the square coaxial line given in [14], the characteristic impedance of this coaxial line is 49.7 Ω. The calculated results are denoted in Figure 2.6 by dashed curves. There is good agreement for frequencies above 2 GHz, while at low frequencies the FD–TD accuracy decreases because the geometry enclosed by our computational domain becomes comparable to the wavelength. It can of course be improved by increasing the number of grids and keeping the same grid size, but this requires more computation time. On the other hand, it is not feasible to increase the grid size to enlarge the geometry, because in our case the grid size is limited by the via dimensions. Techniques such as nonuniform grids and different grid size in different frequency ranges can be used to improve the calculation accuracy and control the computation time. However, compared to the NW model the required computation times are in general very long. On a DECstation 3100, the execution time for calculating the single layer vertical via based on the NW model is less than 1 minute, while it takes over 2 hours using FD–TD within a domain of $60 \times 60 \times 60$ grids.

A 4-layer vertical via was also calculated and measured with each layer having the same dimensions and filling material as the single layer. The results are shown in Figure 2.7, where solid curves are obtained from (2.5), (2.12), (2.17), and (2.22)-(2.24), and the asterisks represent the measurement data. Once again, the results demonstrate that the calculation from the NW model are in very good agreement with the measurements.

The complexity of modeling the geometry for numerical approaches increases

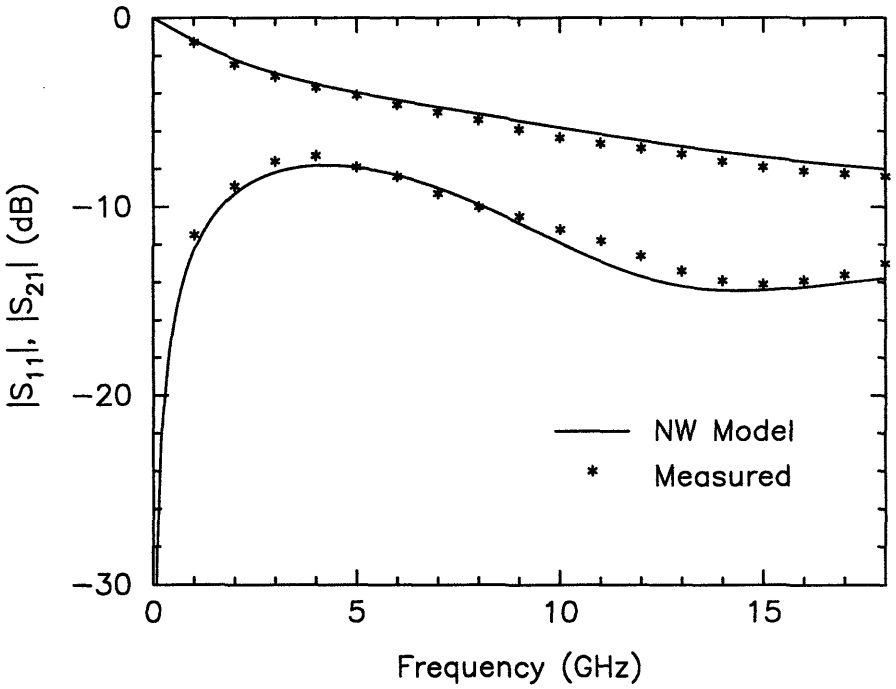

Figure 2.7: $|S_{11}|$ and $|S_{21}|$ of 4-layer vertical via.

with the number of layers. In contrast, this vertical via model provides an efficient way of predicting the performance of vertical vias with ten or even more layers just as easily as for one or two layers. As an example, a multilayer vertical via similar to the IBM 3081 TCM is considered. In this vertical via, the circular via has a radius of $a = 0.0625$ mm and goes through holes of radius $b = 0.1875$ mm in the ground planes. Each layer is composed of a ceramic filling with relative permittivity $\epsilon_r = 10.0$ and thickness $2h = 0.6$ mm. Figure 2.8 shows the frequency domain transmission and reflection coefficients of a 10-layer structure. It is obvious that reflection is generally high and transmission drops rapidly with respect to frequency. Oscillations in the reflection coefficient are observed, which are due to interference of multiple reflections from the junctions. The frequency dependence of the transmission coefficient has significant impact on how fast the circuit can operate. In Figure 2.9 and

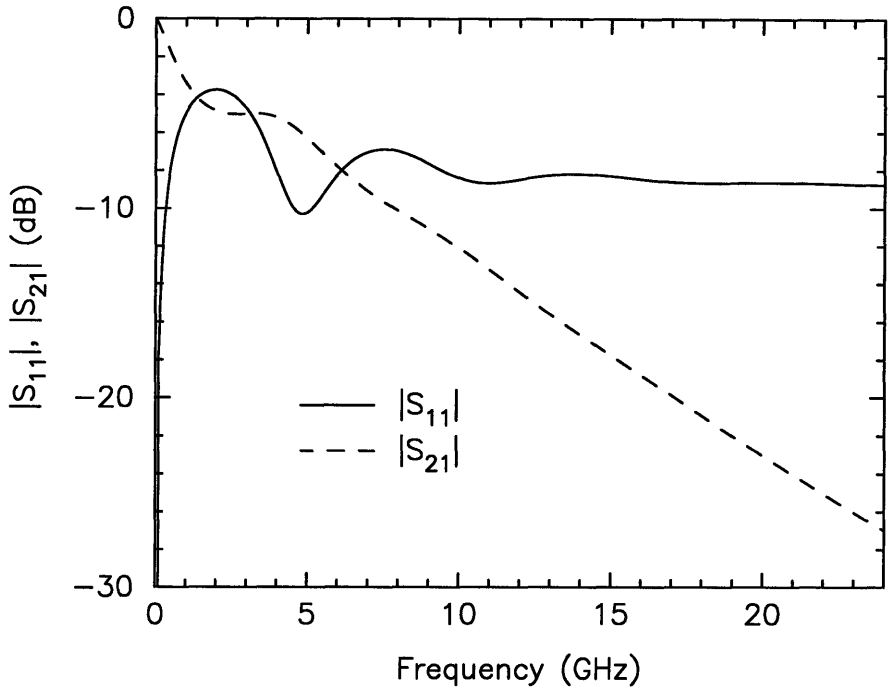

Figure 2.8: Frequency responses of $|S_{11}|$ and $|S_{21}|$ for a 10-layer vertical via.

Figure 2.10, the time domain responses of a 10-layer vertical via subject to trapezoidal pulses of 1 ns duration with 500 ps and 100 ps rise-time is compared, respectively. The relative peak amplitude of these pulses is 10. Note that at 100 ps rise-time the leading edge of the transmitted waveform, defined as the portion from 10 to 90% of the peak amplitude, suffers significant degradation and virtually loses the sharp edge needed for fast switching further down the interconnecting path. A deterioration of the transmitted signal is also observed when the number of layers increases. Hence it is clear that the physical configuration, material property, and number of layers of a vertical via can heavily impact the practical limit of how fast the integrated circuit can operate.

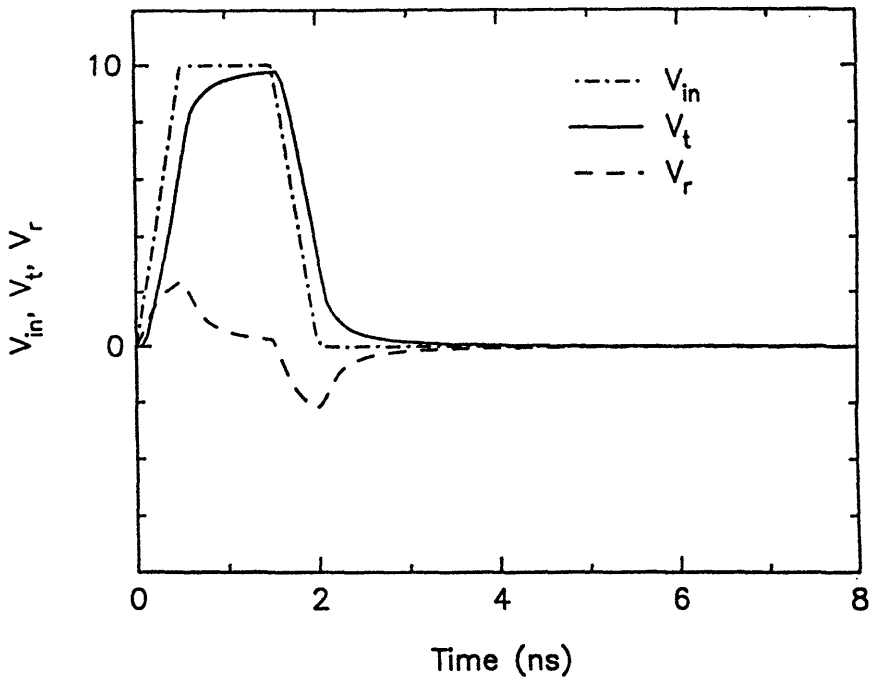

Figure 2.9: Time waveforms in the 10-layer vertical via for a trapezoidal pulse input with a rise-time of 500 ps.

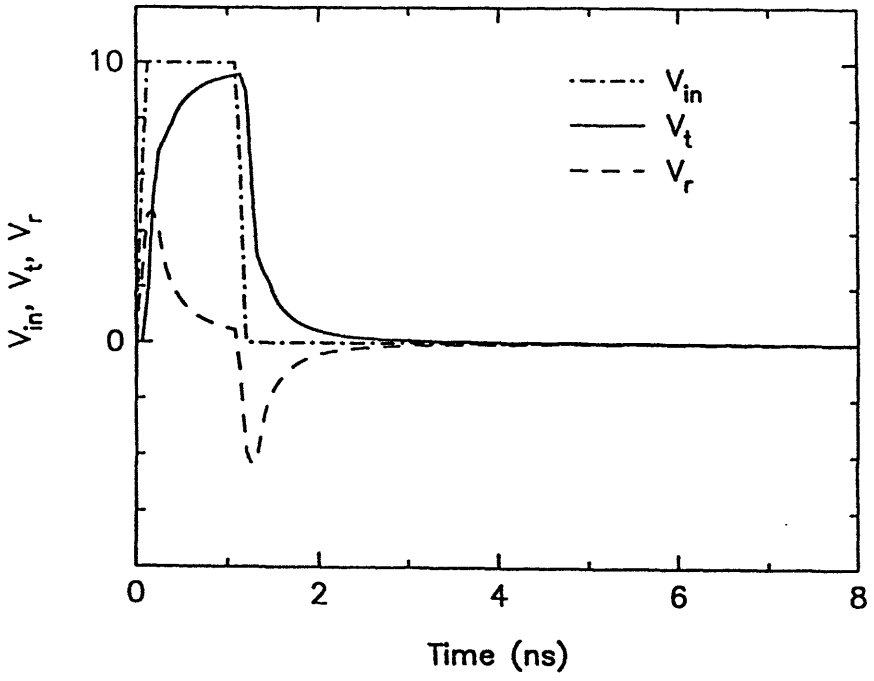

Figure 2.10: Time waveforms in the 10-layer vertical via for a trapezoidal pulse input with a rise-time of 100 ps.

2.5 Transitions from Transmission Line to Vertical Via

Any three-dimensional integrated circuit employing via structures is bound to encounter the transitions from microstrip or stripline to vertical via. The via structure shown in Figure 2.1(a) contains two microstrip-via transitions. In other cases, the via structures might contain stripline-via transitions or both types of transitions.

The ground plane is considered to have finite thickness and the portion of the vertical via passing through the hole in the ground plane is modeled as a segment of a coaxial line, consistent with the treatment in Section 2.3. The transition is then approximated as a junction between microstrip line or stripline and a coaxial line. The transitions are represented by two-port networks connected in cascade with the vertical via network. As shown in Figure 2.11, reference planes P_1 and P_2 on the microstrip and coaxial line are respectively chosen to be far enough away from the junction. Thus, the transition can be characterized by a scattering matrix as follows,

$$\begin{bmatrix} \frac{B_1(\omega)}{\sqrt{Z_1}} \\ \frac{B_2(\omega)}{\sqrt{Z_2}} \end{bmatrix} = \begin{bmatrix} S_{11}(\omega) & S_{12}(\omega) \\ S_{21}(\omega) & S_{22}(\omega) \end{bmatrix} \begin{bmatrix} \frac{A_1(\omega)}{\sqrt{Z_1}} \\ \frac{A_2(\omega)}{\sqrt{Z_2}} \end{bmatrix} \tag{2.25}$$

where A_i and B_i $(i = 1, 2)$ represent the incident and reflected voltage waves respectively on the microstrip and the coaxial line, and Z_i $(i = 1, 2)$ are the characteristic impedances of these two lines. The network parameters of the transition can be obtained indirectly from the reflection and transmission coefficients on the microstrip side when the coaxial side is terminated with different loads, such as matched load and short circuit. When the coaxial line is terminated with a load R_L at reference

plane P_2, the reflection coefficient Γ at reference plane P_1 on the microstrip is of the form,

$$\Gamma(\omega) = \frac{B_1(\omega)}{A_1(\omega)} = S_{11}(\omega) + \frac{S_{12}(\omega)S_{21}(w)\Gamma_L}{1 - S_{22}(\omega)\Gamma_L} \tag{2.26}$$

and the transmission coefficient T from plane P_1 to P_2 has the form

$$T(\omega) = \frac{B_2(\omega)/\sqrt{Z_2}}{A_1(\omega)/\sqrt{Z_1}} = S_{21}(\omega)\left(1 + \frac{S_{22}(\omega)\Gamma_L}{1 - S_{22}(\omega)\Gamma_L}\right). \tag{2.27}$$

Γ_L is the reflection coefficient of the load at plane P_2 on the coaxial line and has the form

$$\Gamma_L = \frac{R_L - Z_2}{R_L + Z_2}$$

The coefficients Γ and T can be numerically determined in the frequency domain through solving a set of coupled integral equations governing the current distribution on the microstrip and the inner conductor of the coaxial line. The coupled integral equations are derived from the analysis of electric field in the transition and boundary conditions [15] in terms of known dyadic Green's function of layered media [16]. Alternatively, the coefficients or the S parameters of the transition can be obtained by means of the FD–TD approach. In this case, however, it is preferable to calculate the S parameters based on (2.25) and exciting the transition from the microstrip line side and the coaxial line side, respectively, while the other end is terminated with a matched load. The reason is that any excitation in a zero- or low-loss system with discontinuities and shorted-circuit terminations will have long time responses

resulting from waves bouncing back and forth between the discontinuities and the terminals with slow decays. This will increase the computation time for FD–TD solutions.

In order to integrate the transmission matrix A_T^c of the transition depicted in Figure 2.11 to the via structure, it is necessary to shift the reference plane P_2 on the coaxial line to the ground plane ($z = 0$). Again, the assumption is that only the TEM mode exists on the coaxial line. Hence the final transmission matrix of the transition is

$$\begin{bmatrix} A_{11T} & A_{12T} \\ A_{21T} & A_{22T} \end{bmatrix} = \begin{bmatrix} A^c_{11T} & A^c_{12T} \\ A^c_{21T} & A^c_{22T} \end{bmatrix} \begin{bmatrix} e^{-j\theta_c} & 0 \\ 0 & e^{j\theta_c} \end{bmatrix} \tag{2.28}$$

where θ_c is the electrical length of the distance l_c from the ground plane to the reference plane P_2.

In Figure 2.12, the magnitudes of S parameters calculated from the FD–TD approach and also the measurements for a transition between a microstrip line and a coaxial line are presented. The dimensions of the transition are $h = 0.751$ mm, width of microstrip $w = 2.135$ mm, $a = 0.475$ mm, $b = 1.524$ mm and $\epsilon_r = 2.2$. The maximum discrepancy between the computed and the measured results over the frequency range from 45 MHz to 18 GHz is less than 2.1 dB. A higher transmission loss in the experimental model is due to the long lengths of the microstrip and coaxial line which are 6 cm and 16 cm, respectively.

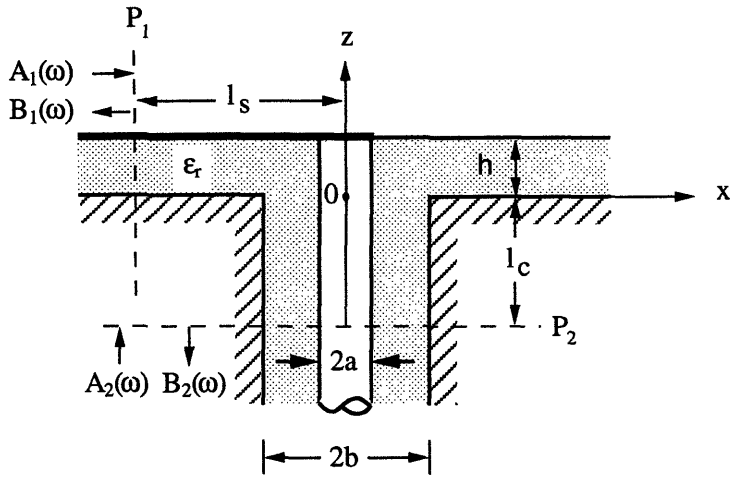

Figure 2.11: Configuration of the transition between microstrip line and coaxial line.

2.6 Simulation Results of Via Structure

To demonstrate the usage of the approaches described in the previous sections, the entire via structure consisting of two identical transitions and a 4-layer vertical via is simulated. The configuration is similar to that in Figure 2.1(a), except that the vertical via part consists of 4 identical layers instead of 3. The dimensions used in this simulation are exactly the same as those given in Section 2.4 and Section 2.5. The frequency response of the 4-layer via structure calculated from the NW model is shown in Figure 2.13 with solid lines. Measurement results are also presented for comparison. Over the range from 1 GHz to 18 GHz the maximum deviation between calculated and measured $|S_{11}|$ is about 1 dB. The discrepancy in the transmission coefficient $|S_{21}|$ is slightly higher, reaching 2 dB at 18 GHz. This can be attributed to the material and conductor losses in the experimental model.

A time-domain simulation of the 4-layer via structure under Gaussian pulse excitations is also performed. The reflected and transmitted waveforms simulated by

the NW model when Gaussian pulses with 50 ps and 25 ps pulse widths (measured at their half amplitude) propagate through the 4-layer via structure are depicted with solid lines in Figure 2.14 and Figure 2.15. In order to verify the simulation in the time domain and in the absence of corresponding experimental measurement, the FD–TD approach is applied to simulate the reflected and the transmitted waveforms in the same via structure, and the results are shown with dashed lines in Figure 2.14 and Figure 2.15. It can be seen that the waveforms obtained from the NW model and the FD–TD method match very well.

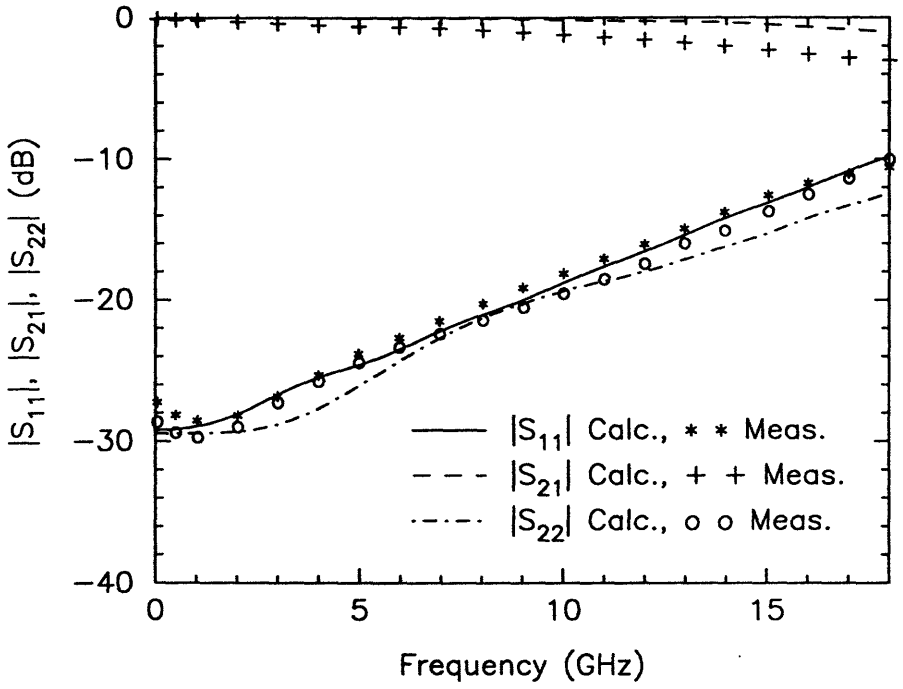

Figure 2.12: Magnitudes of S parameters for the transition between microstrip and coaxial line.

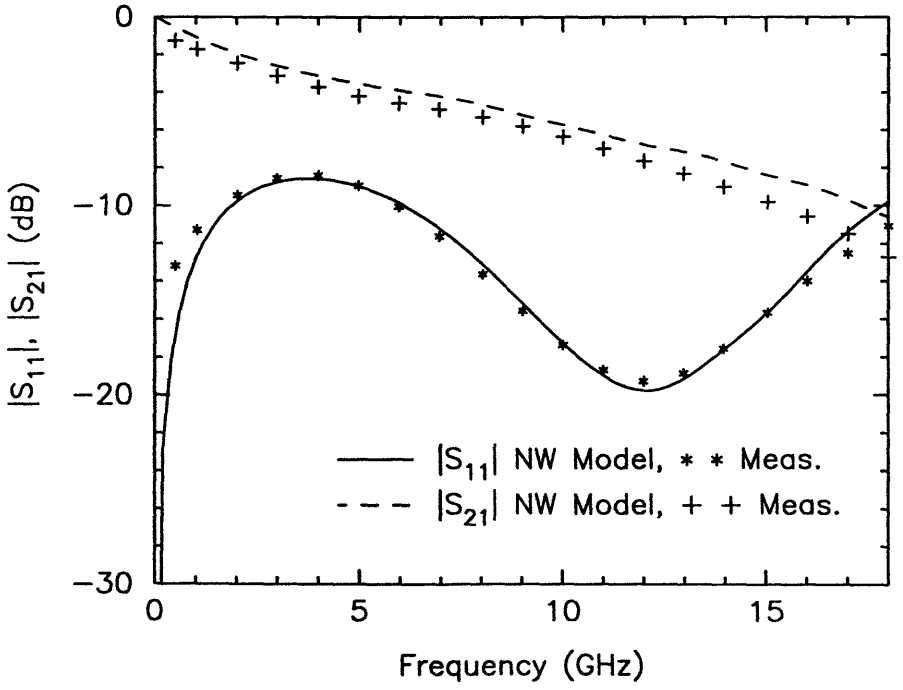

Figure 2.13: Magnitudes of S parameters for the 4-layer via structure with microstrip transitions.

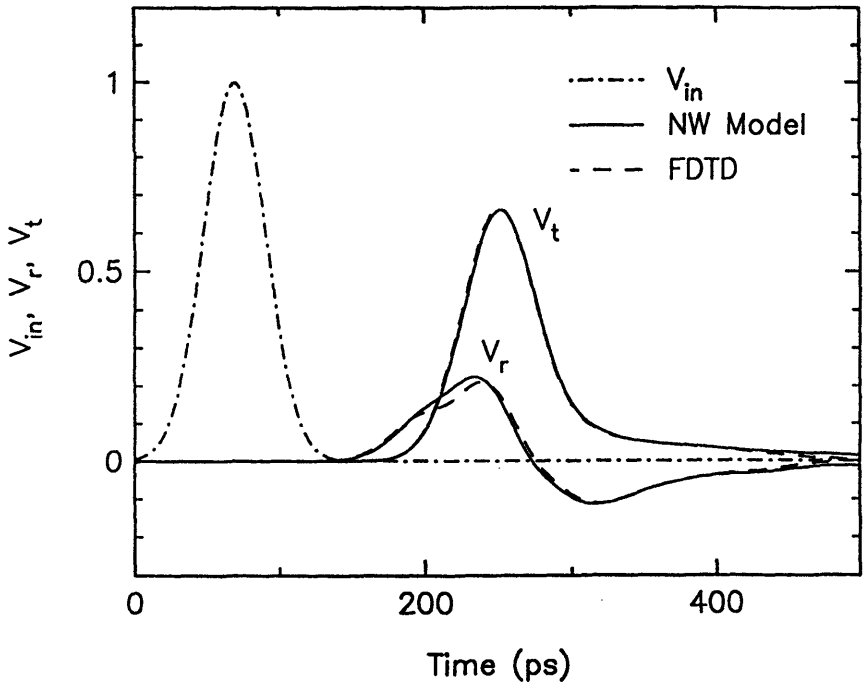

Figure 2.14: Time waveforms for the 4-layer via structure with microstrip transitions for a 50 ps Gaussian pulse input.

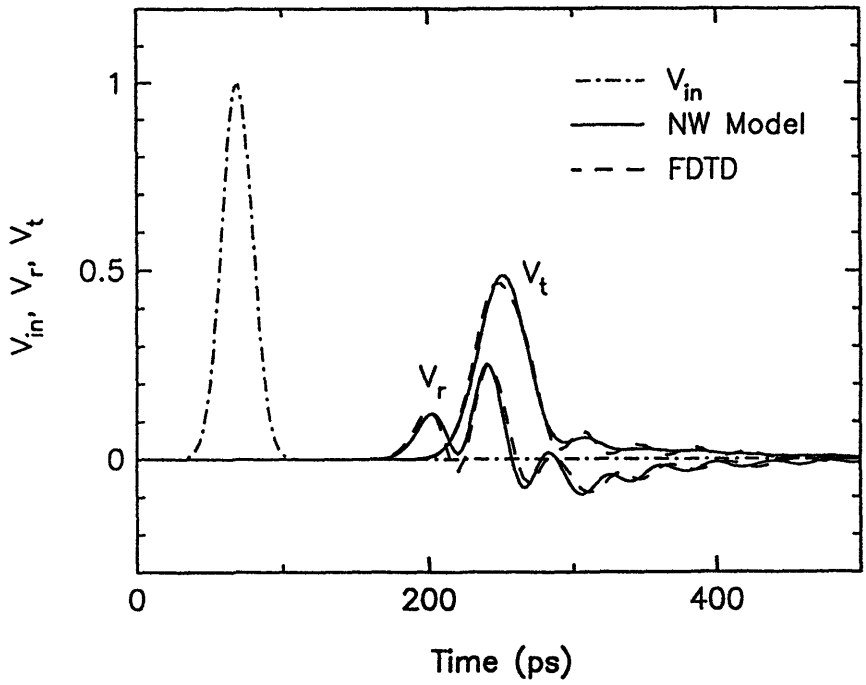

Figure 2.15: Time waveforms for the 4-layer via structure with microstrip transitions for a 25 ps Gaussian pulse input.

2.7 Conclusions

A modeling method for the via structure has been developed based on the equivalent network approach. The advantages of the new modeling method are its flexibility and short computation time. It is very easy to modify the NW model to accommodate the changes in circuit geometry because we are dealing with individual submatrices corresponding to building blocks of the circuit. By adding, removing, or combining submatrices, we can create the model for the new via structure. With its advantage of quick solutions and reconfigurability, the network model has the potential of a good engineering design tool.

The frequency range of validity of the via model is limited by the assumption used for deriving the parameters of the equivalent subnetwork. It varies with the dimensions and material properties of the via structure being modeled. Smaller via structures generally have a higher frequency limit. In the examples mentioned in this chapter, the dimensions of the via structure are quite large, about the order of 1 mm. The analytical results agree well with those obtained from the FD–TD calculation up to frequencies of about 25 GHz and also match very well with measurements.

Chapter 3

Crosstalk Between Adjacent Vias in Multilayered Digital Circuits

3.1 Introduction

In high-speed digital circuits, high frequency phenomena affect the characteristics of interconnections in the circuits. Physical discontinuities or nonuniformities in the connections may cause severe reflections when they can no longer be considered as conducting wires, but behave as transmission lines and/or waveguides. In multilayered digital circuits, vias constitute one of the most commonly-used class of interconnects.

Vias are not good carriers of high-speed signals. They cause signal distortion and reflections as well as severe degradation in the high frequency components. The analysis and modeling of a single via have been presented in Chapter 2, and some quasi-static or quasi-TEM analyses of single via configurations have been discussed in [3, 4, 5, 6]. To date, the analysis of crosstalk between adjacent vias has received very little attention. The major reasons include the complexity of multi-via structures and the difficulty of modeling them accurately over a broad frequency range. Numerical

techniques that apply to arbitrary three dimensional geometries such as the FD–TD, the boundary–element method [7], or the PEEC approach [8] are commonly used to analyze such structures.

In this study two adjacent identical vias is considered. The approach and the corresponding formulation for the transmission and reflection on the active via as well as the near-end and far-end coupled noises on the passive via are described in Section 3.2. The derivation of input admittances is shown in Section 3.3. Numerical results for several two-via structures with different parameters are presented in Section 3.4. These results show the effects of parameters such as spacing between the vias and the number of layers on the crosstalk. To validate the formulation and verify the numerical results, a two-via test model was constructed and its frequency domain characteristics measured. The measurements and the comparison with the calculated results are described and shown in Section 3.5.

3.2 Analysis and Formulation

To facilitate analysis, two adjacent vias are isolated from the complex multi-via interconnection environment. The simplified configuration is shown in Figure 3.1. This allows the identification of the basic coupling phenomena between adjacent vias which eventually may help in the interpretation of data associated with the actual complex environment. It is assumed that the two cylindrical vias have the same diameter $2a$, the via holes in the reference (ground) planes are identical with a diameter $2b$, the center-to-center spacing between the two vias is s, and the thicknesses of the layers and conducting reference planes are $2h$ and d, respectively. The relative permittivity

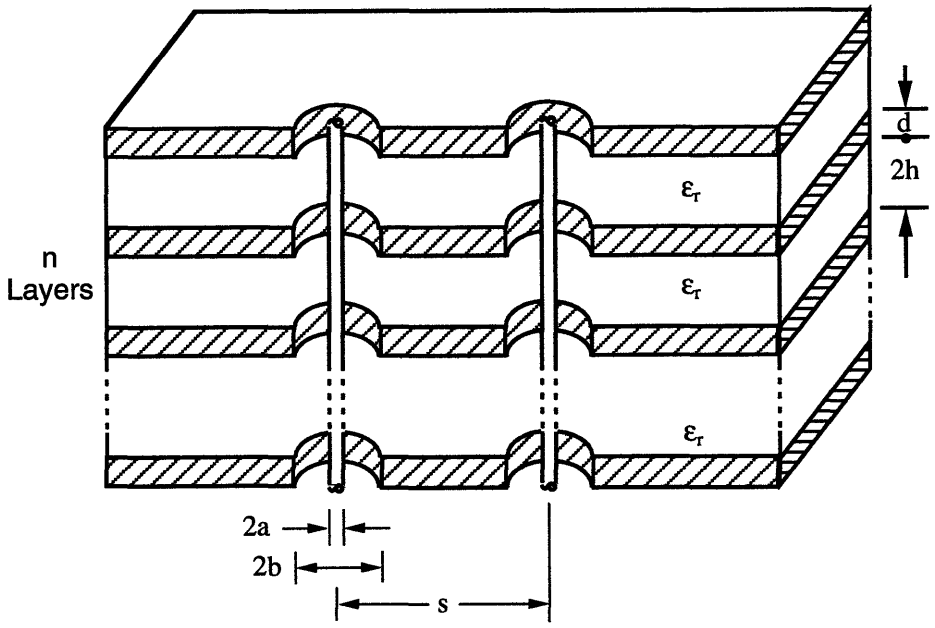

Figure 3.1: Configuration and constitution of the adjacent via structure.

of the multilayer integrated circuit substrate is ϵ_r. Both vias are connected to horizontal signal interconnects, such as microstrips, striplines or other planar transmission lines at each end of the vias. In this formulation, however, the crosstalk resulting from the two adjacent vertical vias as shown in Figure 3.1 is considered without including the influence of the transitions to the horizontal interconnects. The approach for including the effects of the transitions and the horizontal interconnects was described in Section 2.5.

The analysis of the configuration shown in Figure 3.1 can be carried out by means of the even- and odd-mode approach used for characterizing coupled transmission lines. The case where one of the vias is excited by an ideal voltage source with a voltage V is considered as the superposition of a balanced (even-mode) and an unbalanced (odd-mode) excitation, as depicted in Figure 3.2. The situation where the two

vias are excited in balance is equivalent to a single via structure with a magnetic wall placed halfway between the two vias on the plane M and excited with a voltage source of $V/2$. On the other hand, the case of the unbalanced excitation is equivalent to the balanced case with the magnetic wall replaced by an electric wall. The equivalent even- or odd-mode structure is illustrated in Figure 3.3(a). Using an approach similar to that presented in Chapter 2, equivalent cascaded network models can be developed for the even- and odd-mode single vias. These network models consist of segments of coaxial line and two-port subnetworks as shown in Figure 3.3(b). The segments of the coaxial line represent the parts of the via that pass through the reference planes of thickness d, and the two-port subnetworks characterize the radial-waveguide portions with a magnetic or electric wall at a distance $s/2$ from the via. The coaxial lines have a characteristic impedance Z_0 which is determined by the ratio of the via hole radius b to the via radius a. The two-port subnetworks are described by wave transmission matrices $[A^{e,o}_{j,k}]_i$, where the superscripts e and o stand for the even- and odd-mode cases, respectively. The elements $A^{e,o}_{jk}$ $(j,k = 1,2)$ in each wave transmission matrix will be derived in terms of equivalent magnetic frill arrays as follows.

The derivation is started with a single layer even-mode case as shown in Figure 3.4(a). This configuration can be represented by a $\pi-$type network with admittances Y^e_1 and Y^e_2 as shown in Figure 3.4(b). Following the method presented in Section 2.3, i.e., by alternately placing an electric and a magnetic wall on the middle plane M' between the two reference planes A and A', the expressions for Y^e_1 and Y^e_2 can be obtained. First, we consider the case with an electric wall on plane M', shown in Figure 3.5(a). The corresponding equivalent network has the form of Figure 3.5(b).

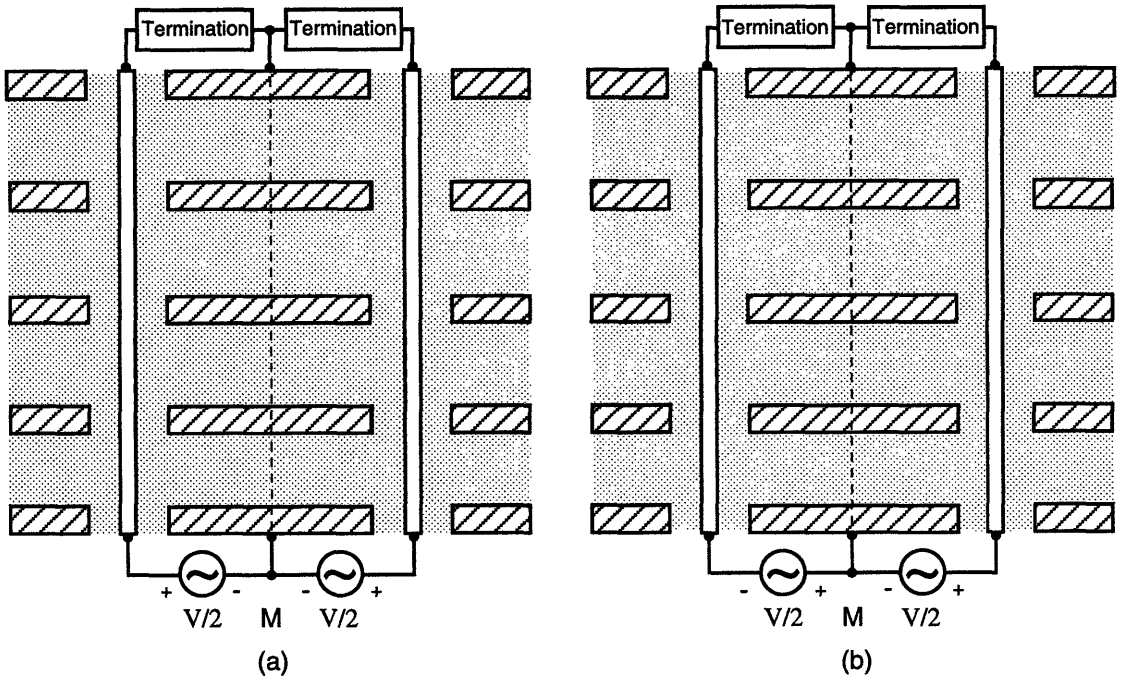

Figure 3.2: Two vias excited: (a) in balance (even-mode) and (b) unbalanced (odd-mode).

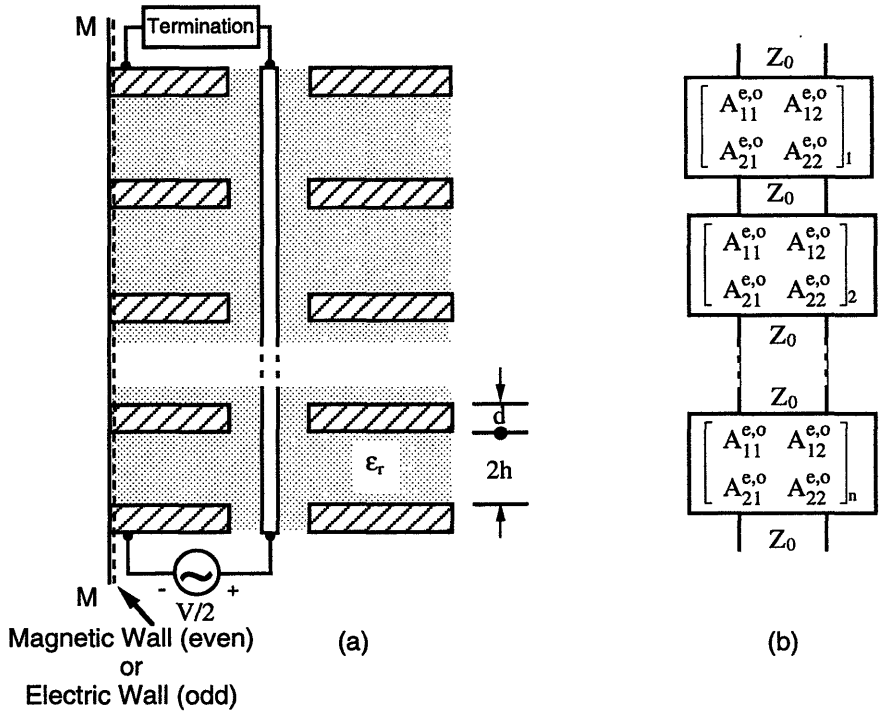

Figure 3.3: Equivalent even- or odd-mode single via structure (a) and their equivalent network model (b).

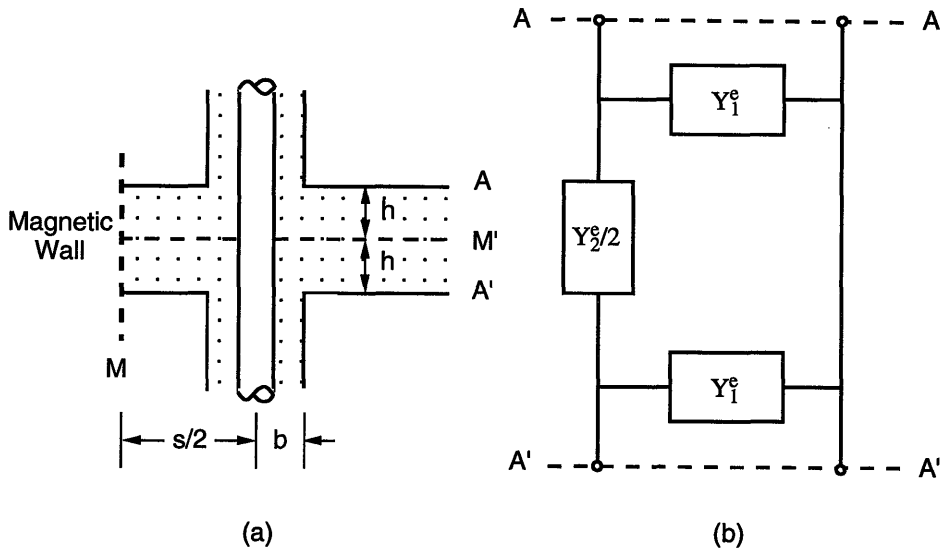

Figure 3.4: Configuration for even-mode one layer via (a) and its $\pi-$type equivalent network (b).

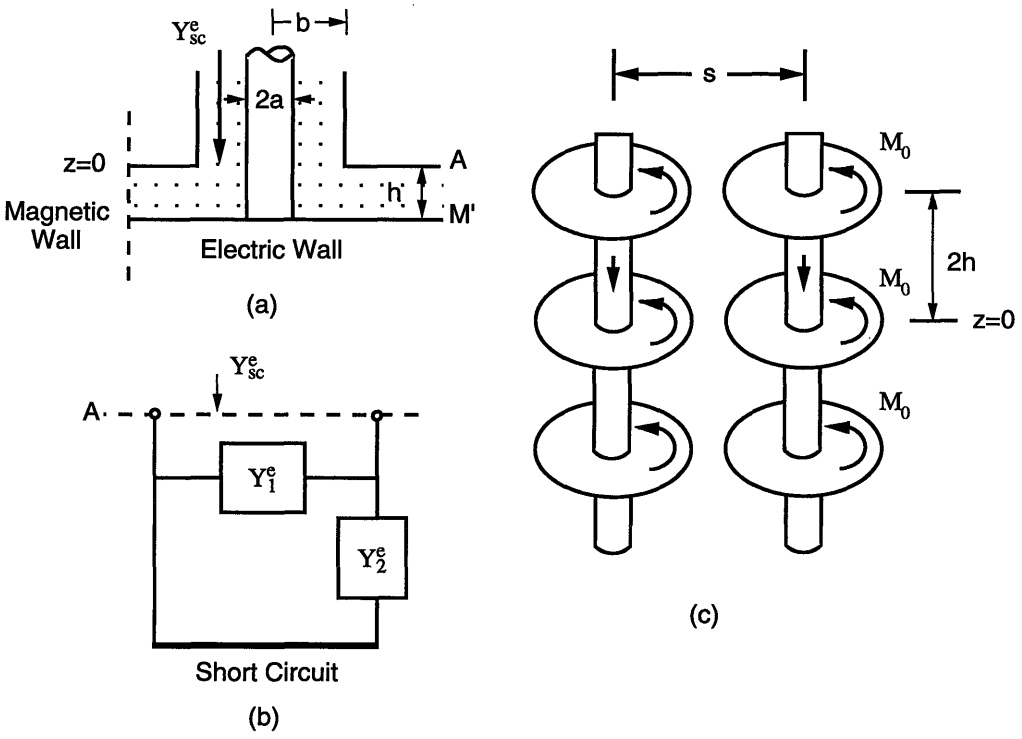

Figure 3.5: Configuration for even-mode one layer via with an electric wall on plane M (a), $\pi-$type equivalent circuit (b), and equivalent magnetic frill arrays (c).

Assuming that only the TEM mode exists in the coaxial line, then the electric field in the aperture where the coaxial line passes through the ground plane is approximately

$$E_r(r,\theta,0) = \frac{V}{r\ln(b/a)}, \qquad a \le r \le b \tag{3.1}$$

where V is the excitation voltage. The fields between the two reference planes and the current on the cylindrical conducting element are entirely determined by the aperture electric field E_r at plane A. The excitation field $E_r(r,\theta,0)$ can be considered as a magnetic current frill M_0 having the form,

$$M_0 = \begin{cases} -\dfrac{2V}{r\ln(b/a)} & a \le r \le b \\ 0 & \text{elsewhere.} \end{cases} \tag{3.2}$$

Applying the image theory at the electric and magnetic walls, an equivalent model is obtained which consists of two identical magnetic frill arrays in parallel as shown in Figure 3.5(c). Based on this model, the input admittance Y^e_{sc} as derived in the next section is

$$\begin{aligned} Y^e_{sc} = & -\frac{2\pi j\sqrt{\epsilon_r}}{\eta_0 kh\ln^2(b/a)}\Bigg\{kh\ln(b/a)\cot(kh) \\ & +\frac{\pi}{2}[Y_0(ka)J_0(kb) - Y_0(kb)J_0(ka)]\left[\frac{H_0^{(2)}(kb) + J_0(kb)H_0^{(2)}(ks)}{H_0^{(2)}(ka) + J_0(ka)H_0^{(2)}(ks)}\right] \\ & -2\sum_{m=1}^{\infty}\frac{1}{q_m^2}[K_0(q_mkb)I_0(q_mka) - K_0(q_mka)I_0(q_mkb)] \\ & \cdot\left[\frac{K_0(q_mkb) + I_0(q_mkb)K_0(q_mks)}{K_0(q_mka) + I_0(q_mka)K_0(q_mks)}\right]\Bigg\} \end{aligned} \tag{3.3}$$

where $k = 2\pi\sqrt{\epsilon_r}/\lambda$, ϵ_r is the dielectric constant of the substrate, and J_0, Y_0, I_0, K_0

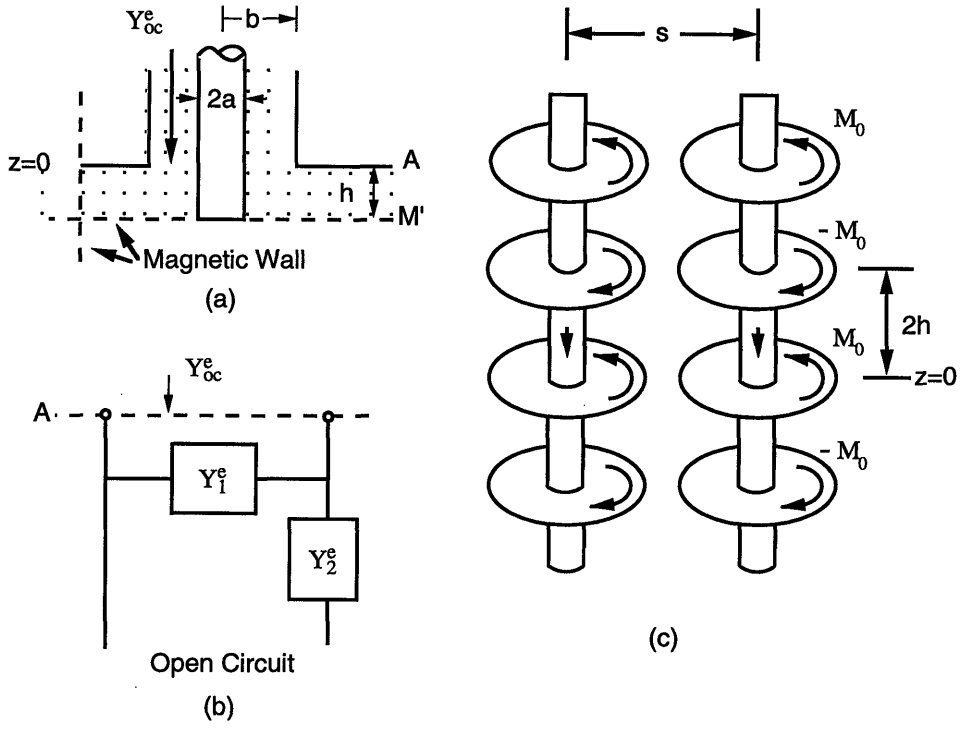

Figure 3.6: Configuration for magnetic walls placed on planes M and M' and its equivalent circuit and magnetic frill array model.

and $H_0^{(2)}$ are Bessel functions, modified Bessel functions and Hankel function of the second kind, respectively. Also

$$q_m = \sqrt{\left(\frac{m\pi}{kh}\right)^2 - 1} \tag{3.4}$$

and $\eta_0 = \sqrt{\frac{\mu_0}{\epsilon_0}}$ is the intrinsic impedance of free space.

From the equivalent network in Figure 3.5(b), the relationship between the admittance Y_{sc}^e and the network elements Y_1^e and Y_2^e is simply

$$Y_{sc}^e = Y_1^e + Y_2^e. \tag{3.5}$$

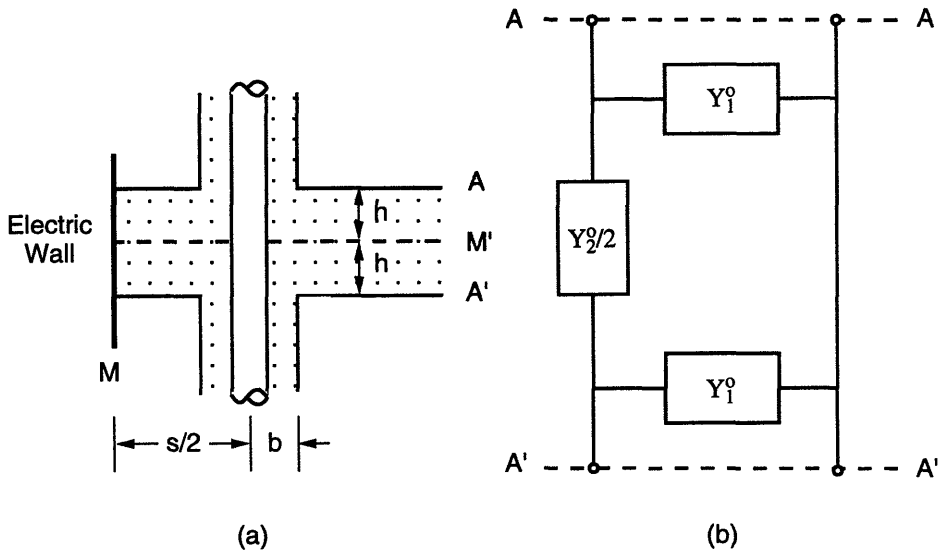

Figure 3.7: Configuration for odd-mode single layer via (a) and its $\pi-$type equivalent network (b).

By placing a magnetic wall on the middle plane M' of Figure 3.4(a), we obtain the configuration of Figure 3.6(a) and derive the corresponding equivalent network and the magnetic frill array model as depicted in Figure 3.6(b) and Figure 3.6(c), respectively. As follows from Chapter 2 and Section 3.3, the input admittance Y_{oc}^e at the aperture on plane A looking from the coaxial line has the form

$$\begin{aligned} Y_{oc}^e = \frac{2\pi j\sqrt{\epsilon_r}}{\eta_0 kh\ln^2(b/a)}\Bigg\{ & kh\ln(b/a)\tan(kh) \\ & +2\sum_{n=0}^{\infty}\frac{1}{q_n^2}\left[K_0(q_nkb)I_0(q_nka)-K_0(q_nka)I_0(q_nkb)\right] \\ & \cdot\left[\frac{K_0(q_nkb)+I_0(q_nkb)K_0(q_nks)}{K_0(q_nka)+I_0(q_nka)K_0(q_nks)}\right]\Bigg\} \end{aligned} \tag{3.6}$$

where

$$q_n = \sqrt{\left(\frac{(2n+1)\pi}{2kh}\right)^2 - 1}. \tag{3.7}$$

It is apparent from the equivalent network of Figure 3.6(b) that

$$Y_1^e = Y_{oc}^e. \tag{3.8}$$

Substituting (3.8) into (3.5), we obtain

$$Y_2^e = Y_{sc}^e - Y_{oc}^e. \tag{3.9}$$

Consider a single layer via with an electric wall on plane M as shown in Figure 3.7(a). This structure corresponds to the single layer vias under odd-mode excitation, and it can also be represented by a $\pi-$type network but with elements Y_1^o and Y_2^o, Figure 3.7(b). The analysis of this configuration is similar to the even-mode excitation where equivalent magnetic frill array models can be obtained by placing electric and magnetic walls on the middle plane M'.

When an electric wall is placed on the plane M', the configuration becomes a special case of the structure discussed in [19] with the conducting wall on one side of the rectangular waveguide removed. The input admittance Y_{sc}^o on plane A looking in from the coaxial line is

$$Y_{sc}^o = -\frac{2\pi j\sqrt{\epsilon_r}}{\eta_0 kh \ln^2(b/a)}\Big\{kh\ln(b/a)\cot(kh)$$

$$+\frac{\pi}{2}[Y_0(ka)J_0(kb) - Y_0(kb)J_0(ka)]\left[\frac{H_0^{(2)}(kb) - J_0(kb)H_0^{(2)}(ks)}{H_0^{(2)}(ka) - J_0(ka)H_0^{(2)}(ks)}\right]$$

$$-2\sum_{m=1}^{\infty}\frac{1}{q_m^2}[K_0(q_mkb)I_0(q_mka) - K_0(q_mka)I_0(q_mkb)]$$

$$\cdot\left[\frac{K_0(q_mkb) - I_0(q_mkb)K_0(q_mks)}{K_0(q_mka) - I_0(q_mka)K_0(q_mks)}\right]\Bigg\} \qquad (3.10)$$

where all the functions and variables are the same as in (3.3).

When a magnetic wall is located on plane M' (instead of an electric wall), the equivalent magnetic frill array model for this structure is the same as that in Figure 3.6(c). However, the magnetic and electric currents have reversed directions in one of the two magnetic frill arrays. The input admittance Y_{oc}^o is then

$$Y_{oc}^o = \frac{2\pi j\sqrt{\epsilon_r}}{\eta_0 kh\ln^2(b/a)}\Bigg\{kh\ln(b/a)\tan(kh)$$

$$+2\sum_{n=0}^{\infty}\frac{1}{q_n^2}[K_0(q_nkb)I_0(q_nka) - K_0(q_nka)I_0(q_nkb)]$$

$$\cdot\left[\frac{K_0(q_nkb) - I_0(q_nkb)K_0(q_nks)}{K_0(q_nka) - I_0(q_nka)K_0(q_nks)}\right]\Bigg\} \qquad (3.11)$$

where q_n is given by (3.7).

The elements Y_1^o and Y_2^o in the equivalent circuit of Figure 3.7(b) can also be expressed by Y_{sc}^o and Y_{oc}^o as

$$Y_1^o = Y_{oc}^o \qquad \text{and} \qquad Y_2^o = Y_{sc}^o - Y_{oc}^o \qquad (3.12)$$

From (3.8), (3.9), (3.12) and network theory, the wave transmission matrices

$[A^{e,o}]$ for the $\pi-$type networks in Figure 3.4(b) and Figure 3.7(b) are

$$\begin{bmatrix} A_{11}^{e,o} & A_{12}^{e,o} \\ A_{21}^{e,o} & A_{22}^{e,o} \end{bmatrix} = \frac{1}{\overline{Y}_{sc}^{e,o} - \overline{Y}_{oc}^{e,o}} \cdot \begin{bmatrix} 1 + \overline{Y}_{sc}^{e,o} + \overline{Y}_{oc}^{e,o} + \overline{Y}_{sc}^{e,o}\overline{Y}_{oc}^{e,o} & -1 + \overline{Y}_{sc}^{e,o}\overline{Y}_{oc}^{e,o} \\ 1 - \overline{Y}_{sc}^{e,o}\overline{Y}_{oc}^{e,o} & -1 + \overline{Y}_{sc}^{e,o} + \overline{Y}_{oc}^{e,o} - \overline{Y}_{sc}^{e,o}\overline{Y}_{oc}^{e,o} \end{bmatrix} \tag{3.13}$$

where

$$\overline{Y}_{sc}^{e,o} = \frac{Y_{sc}^{e,o}}{Y_0} \quad \text{and} \quad \overline{Y}_{oc}^{e,o} = \frac{Y_{oc}^{e,o}}{Y_0}. \tag{3.14}$$

Y_0 is the characteristic admittance of the coaxial line, and the superscripts 'e' and 'o' stand for the cases of even- and odd-mode excited single layer vias, respectively.

For vias with n identical layers with even- or odd-mode excitation, the total wave transmission matrix is

$$\begin{bmatrix} A_{11T}^{e,o} & A_{12T}^{e,o} \\ A_{21T}^{e,o} & A_{22T}^{e,o} \end{bmatrix} = \begin{bmatrix} e^{j\theta/2} & 0 \\ 0 & e^{-j\theta/2} \end{bmatrix} \begin{bmatrix} A_{11}^{e,o}e^{j\theta} & A_{12}^{e,o} \\ A_{21}^{e,o} & A_{22}^{e,o}e^{-j\theta} \end{bmatrix}^n \begin{bmatrix} e^{j\theta/2} & 0 \\ 0 & e^{-j\theta/2} \end{bmatrix}. \tag{3.15}$$

θ is the electrical length of each of the coaxial line segments

$$\theta = \frac{2\pi}{\lambda_g} d \tag{3.16}$$

where λ_g is the guide wavelength and d is the physical length of the coaxial line segment.

The characteristics of the two adjacent vias in a multilayered digital circuits are entirely governed by these even- and odd-mode wave transmission matrices. They

have the following relationship with the scattering matrix of a four-port system,

$$S_{11} = \frac{1}{2}\left(\frac{A^e_{21T}}{A^e_{11T}} + \frac{A^o_{21T}}{A^o_{11T}}\right) \tag{3.17}$$

$$S_{21} = \frac{1}{2}\left(\frac{1}{A^e_{11T}} + \frac{1}{A^o_{11T}}\right) \tag{3.18}$$

$$S_{31} = \frac{1}{2}\left(\frac{A^e_{21T}}{A^e_{11T}} - \frac{A^o_{21T}}{A^o_{11T}}\right) \tag{3.19}$$

$$S_{41} = \frac{1}{2}\left(\frac{1}{A^e_{11T}} - \frac{1}{A^o_{11T}}\right) \tag{3.20}$$

The input voltage is applied to port 1, the opposite end of the same via is port 2; ports 3 and 4 are on the passive via with port 3 being adjacent to port 1. The four elements, S_{11}, S_{21}, S_{31}, and S_{41}, correspond to the input reflection, transmission, near-end coupling and far-end coupling coefficients, respectively. Since the structure under analysis is symmetric and reciprocal, the elements of its scattering matrix bear the following relationships,

$$\begin{aligned} S_{11} &= S_{22} = S_{33} = S_{44} \\ S_{21} &= S_{12} = S_{43} = S_{34} \\ S_{31} &= S_{13} = S_{42} = S_{24} \\ S_{41} &= S_{14} = S_{32} = S_{23} \end{aligned}$$

The time waveforms for the reflected and the transmitted signals as well as the near- and far-end coupled noise can be obtained by means of the Fourier transform.

3.3 Derivation of Input Admittances

Otto [10] obtains an input admittance Y for a parallel plate antenna fed by a coaxial line, under the assumption that only TEM mode propagates in the line

$$Y = \frac{2\pi}{\ln(b/a)} \frac{\int_0^{2\pi} \int_a^b H_\theta(r,\theta,0)\, dr d\theta}{\int_0^{2\pi} \int_a^b E_r(r,\theta,0)\, dr d\theta}. \tag{3.21}$$

A cylindrical coordinate system (r,θ,z) is used with the origin on the intersection plane of the coaxial line and ground plane and at the center of the coaxial line inner conductor and the z-axis aligned with the coaxial line axis. Indeed, the configuration analyzed by Otto is the same as Figure 3.5(a) without the magnetic wall. With the TEM assumption in the coaxial line, the electric field $E_r(r,\theta,0)$ in the aperture formed by the coaxial line passing through the ground plane is given by (3.1). The magnetic field $H_\theta(r,\theta,0)$ can be derived from an equivalent magnetic frill array $\sum M_0 \delta(z - m(2h))$ $(m = 0, \pm 1, \pm 2, ...)$, where M_0 is the frill of equivalent magnetic current in the aperture at $z = 0$ and is given by (3.2).

The input admittance Y of the parallel-plate antenna as seen from the coaxial line side can be shown from [10, 19] to be,

$$Y = \frac{1}{2h} \left\{ \mathcal{Y}(0) + 2 \sum_{m=1}^{\infty} \mathcal{Y}(\frac{m\pi}{h}) \right\} \tag{3.22}$$

where $\mathcal{Y}(\alpha)$ is

$$\mathcal{Y}(\alpha) = \frac{1}{V \ln(b/a)} \int_0^{2\pi} \int_a^b \mathcal{H}_\theta(r, \theta, \alpha) dr d\theta. \tag{3.23}$$

$\mathcal{H}_\theta(r, \theta, \alpha)$ is the Fourier transform of the magnetic field H_θ

$$\begin{aligned} \mathcal{H}_\theta(r, \theta, \alpha) &= \frac{\mathcal{I}(\alpha)}{2\pi} q I_0(qa) K_1(qr) + \frac{2jkV\sqrt{\epsilon_r}}{q\eta_0 \ln(b/a)} \\ &\cdot \begin{cases} \frac{1}{qr} - I_0(qa)K_1(qr) - K_0(qb)I_1(qr), & a \le r \le b \\ [I_0(qb) - I_0(qa)]K_1(qr), & r \ge b. \end{cases} \end{aligned} \tag{3.24}$$

In (3.24), $\mathcal{I}(\alpha)$ is the Fourier transform of the current flowing on the cylindrical conducting element, i.e., the portion of the coaxial line inner conductor extending to the two parallel conducting plates. η_0 is the intrinsic impedance of free space, I_0, I_1, K_0 and K_1 are modified Bessel functions, and k and q are defined as follows,

$$k = \frac{2\pi\sqrt{\epsilon_r}}{\lambda} \quad \text{and} \quad q = \sqrt{\alpha^2 - k^2} \tag{3.25}$$

where ϵ_r is the relative dielectric constant of the filling material, and λ is the operating wavelength in free space.

The current $I(z)$ flowing on the cylindrical conducting element can be found in terms of the infinite magnetic frill array model and the boundary conditions, i.e., vanishing tangential electric field E_z on the surface of the cylindrical conducting plane. In the case of Figure 3.5(a), there exists a magnetic wall near the cylindrical element. Using image theory, a magnetic frill array model consisting of two identical, infinite, magnetic frill arrays with a center-to-center spacing of s instead of a single

array is obtained as shown in Figure 3.5(c). The current $I(z)$ on one of these two cylindrical conducting elements will not only be determined by the magnetic frill array distributed along this conducting element itself, but is also affected by the other magnetic frill array. The tangential electric field over the surface of the cylindrical conducting element will be the sum of the electric fields generated by the two arrays. As in [19], the average electric field over the aperture is used to express the second array contribution. The current distribution, $\mathcal{I}(\alpha)$, can be obtained in the Fourier domain by imposing the following approximate boundary condition

$$\mathcal{E}_z(a,\alpha) + \mathcal{E}_z^{av}(s,\alpha) = 0 \tag{3.26}$$

where $\mathcal{E}_z(r,\alpha)$ is the Fourier transform of the E_z component, given by [19] as

$$\begin{aligned} \mathcal{E}_z(r,\alpha) &= -\frac{\eta_0 q^2}{2\pi jk\sqrt{\epsilon_r}}\mathcal{I}(\alpha)I_0(qa)K_0(qr) \\ &\quad -\frac{2V}{\ln(b/a)}\begin{cases} I_0(qr)K_0(qb) - I_0(qa)K_0(qr) & a \le r \le b \\ [I_0(qb) - I_0(qa)]K_0(qr) & r \ge b \end{cases} \end{aligned} \tag{3.27}$$

and $\mathcal{E}_z^{av}(s,\alpha)$ is the average value of $\mathcal{E}_z(r,\alpha)$ over a circular contour with radius a, centered at a distance s. From (3.26) and (3.27), the current $\mathcal{I}(\alpha)$ is then derived to be

$$\mathcal{I}(\alpha) = \frac{4\pi jkV\sqrt{\epsilon_r}}{\eta_0 q^2}\left[1 - \frac{K_0(qb) + I_0(qb)K_0(qs)}{K_0(qa) + I_0(qa)K_0(qs)}\right] \tag{3.28}$$

In obtaining (3.28), the following approximation is used assuming $s \ll a$

$$\frac{1}{2\pi a}\int_0^{2\pi} K_0(qr)ad\theta \simeq \frac{1}{2\pi}\int_0^{2\pi} K_0(q(s + a\cos\theta))d\theta$$

$$\simeq \frac{K_0(qs)}{2\pi}\int_0^{2\pi} e^{-qa\cos\theta}d\theta$$

$$= K_0(qs)I_0(qa)$$

Substituting (3.28) into (3.24) and utilizing the following approximation

$$\int_0^{2\pi}\int_{s+a\cos\theta}^{s+b\cos\theta} K_1(qx)\,dxd\theta = -\int_0^{2\pi}\left[K_0(q(s+b\cos\theta)) - K_0(q(s+a\cos\theta))\right]\,d\theta$$

$$\simeq -2\pi K_0(qs)[I_0(qb) - I_0(qa)],$$

$\mathcal{Y}(\alpha)$ can be calculated by means of (3.23) and subsequently obtain $\mathcal{Y}(\frac{m\pi}{h})$ for $(m = 0, 1, 2, ...)$.

Finally, the input admittance Y_{sc}^e of the configuration in Figure 3.5(a) is obtained from (3.22) that has the form given in (3.3). The input admittance Y_{oc}^e (even-mode open circuit) as well as the input admittances Y_{sc}^o (odd-mode short circuit) and Y_{oc}^o (odd-mode open circuit) can also be obtained in a similar manner as Y_{sc}^e.

3.4 Numerical Results

In this section, two configurations of coupled via structures will be analyzed numerically based on the analytical formulas developed in Section 3.2. The first configuration is chosen to have large dimensions to facilitate the construction of the experimental model and subsequent validation of the closed-form formulas. The second configuration has dimensions of realistic integrated circuit modules, such as the IBM thermal conduction module. We are mostly interested in the crosstalk between the vias; other

propagation characteristics are of less interest. Since the coupling between the vias is usually weak, we shall expect that the signal reflection and transmission characteristics of the active via will be similar to those predicted in Chapter 2.

The case considered is a pair of identical 4-layer vias with a spacing $s = 4.0$ mm, substrate material $\epsilon_r = 2.2$ and dimensions: $a = 0.457$ mm, $b = 1.524$ mm, $h = 0.762$ mm and $d = 0$. The calculated scattering parameters, S_{11}, S_{21}, S_{31} and S_{41} versus frequency are shown in Figure 3.8. The coupling coefficients for the near- and far-end are both less than -12 dB over the calculated frequency range. The far-end coupling is higher than the near-end coupling for frequencies above 1 GHz. The near-end noise is mainly a result of the coupling of lower frequency components up to 6 GHz, while the far-end noise is due to high frequency components beyond 1 GHz. When spacing s is increased from 4.0 mm to 10.0 mm while other parameters are unchanged, both near- and far-end coupling coefficients decrease. The differences are about 4 dB as illustrated in Figure 3.9. The variation in the calculated coupling coefficients with number of layers is shown in Figure 3.10, where the number of layers is increased from 4 to 8, while other parameters are unchanged. At low frequencies the increase in coupling coefficients is due to a higher reflection coefficient and a longer coupling region for the 8 layer structure. At higher frequencies the far-end coupling appears to decrease because more layers will cause more energy to be transferred to the radial waveguide modes guided by the parallel conducting ground planes and propagating away from the via.

Figure 3.11 shows the calculated results of the scattering parameters of the second configuration with 10 layers and $a = 0.0625$ mm, $b = 0.1875$ mm, $h = 0.3$

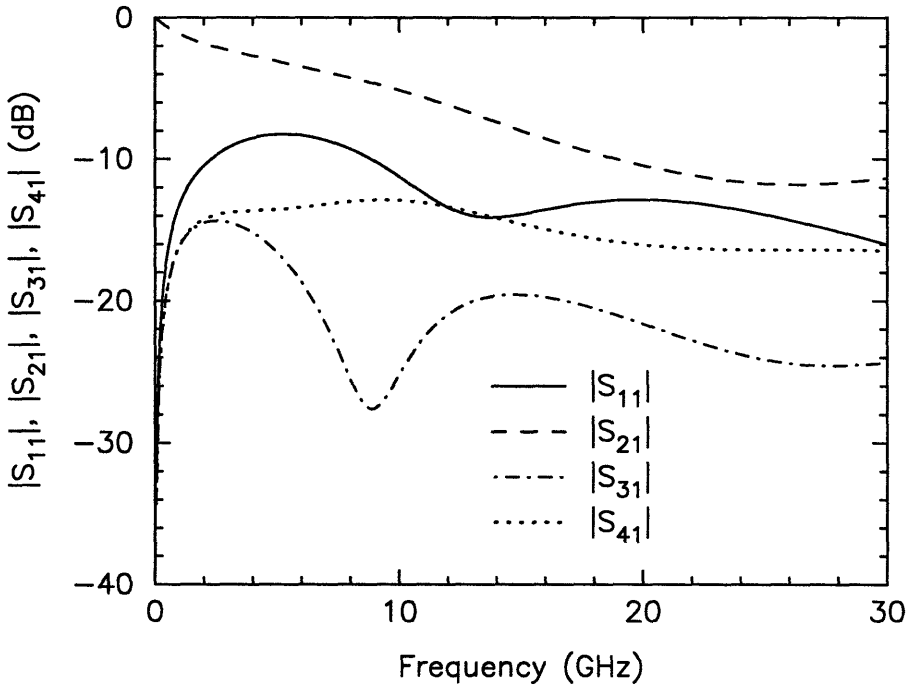

Figure 3.8: Magnitude of S parameters for a pair of 4-layer via with $a = 0.457$ mm, $b = 1.524$ mm, $h = 0.762$ mm, $s = 4.0$ mm, $d = 0$ and $\epsilon_r = 2.2$.

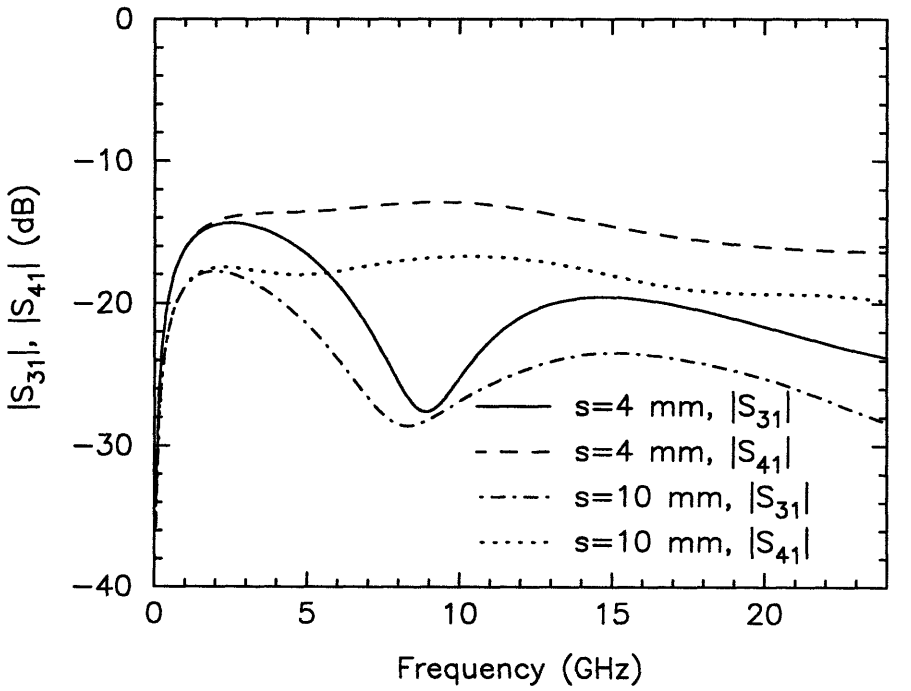

Figure 3.9: Coupling coefficient for a pair of 4-layer via with different spacing.

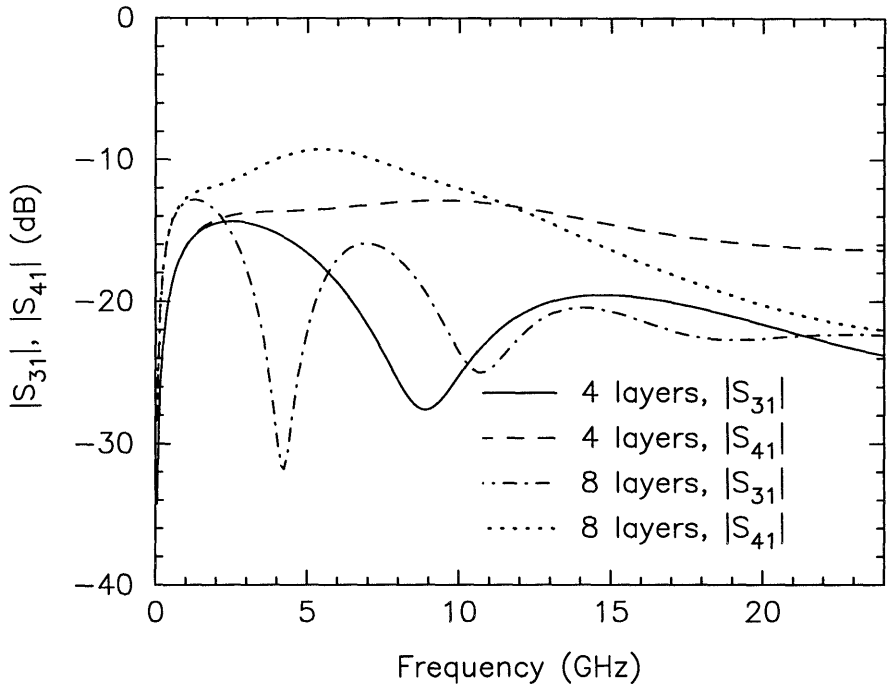

Figure 3.10: Coupling coefficient for a pair of via with different number of layers.

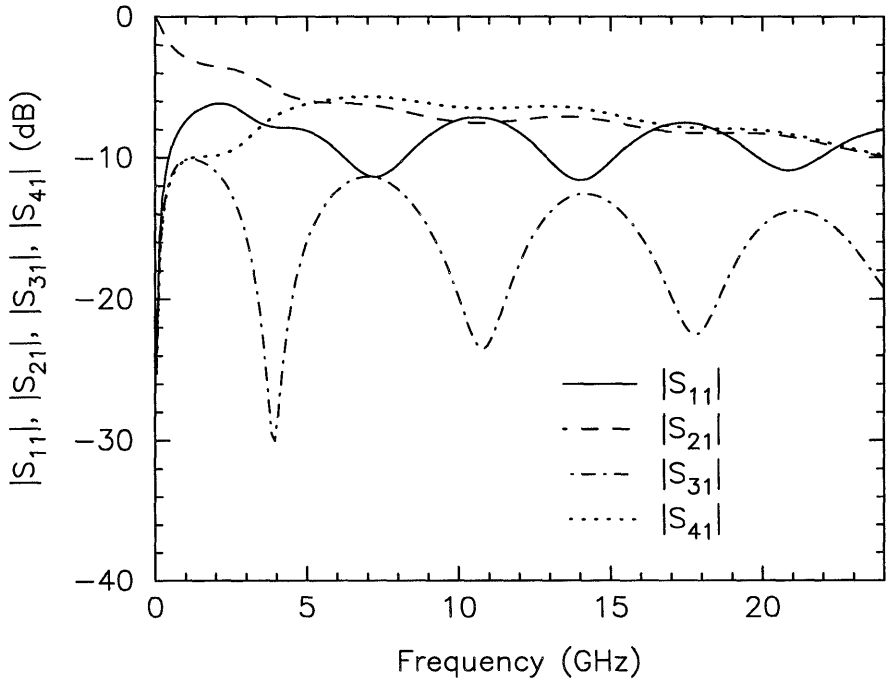

Figure 3.11: Magnitude of S parameters for a pair of 10-layer via with $a = 0.0625$ mm, $b = 0.1875$ mm, $h = 0.3$ mm, $s = 0.4$ mm, $d = 0$ and $\epsilon_r = 10$.

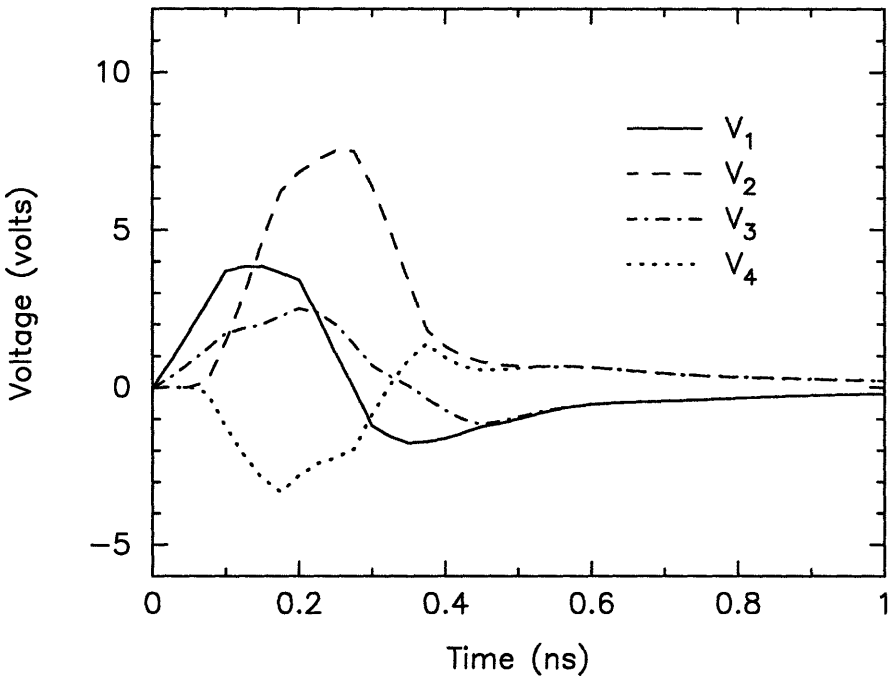

Figure 3.12: Time waveforms of reflection, transmission and coupling noises for a pair of 10-layer via with $a = 0.0625$ mm, $b = 0.1875$ mm, $h = 0.3$ mm, $s = 0.4$ mm, $d = 0$ and $\epsilon_r = 10$.

mm, $s = 0.4$ mm, $d = 0$ and $\epsilon_r = 10$. The higher dielectric constant ϵ_r and the larger number of layers further deteriorate the propagation characteristics and result in more undesired coupling. The coupled noise waveforms for the near-end, V_3, and the far-end, V_4, are shown in Figure 3.12. Here, a trapezoidal pulse with rise, fall and duration time of 100 ps and a relative amplitude of 10 is the input to port 1. The reflected waveform V_1 and the transmitted waveform V_2 on the active via are also presented in the same figure. From the figure, we may conclude that the given via structure cannot be used for the transmission of such narrow pulses because of considerable reflection and crosstalk. For multilayered circuits, e.g., 10 layers and $\epsilon_r = 10$, the fastest pulse which can propagate through the vias without serious distortion, reflection, and coupled noise should not have a rise-time of less than 500 ps. The performance of the via interconnect will further deteriorate if the effects of the transition from the via to the horizontal transmission lines are also taken into account.

3.5 Experimental Validation

A physical model is constructed from the same materials as the single vertical via model described in Chapter 2. The configuration of the experimental model is shown in Figure 3.13. An RT/Duroid 5880 laminate is cut into 4 pieces of 101.6 mm by 127.0 mm. Two through holes with a diameter of 0.914 mm and a center-to-center spacing of 10 mm are made in the middle of each laminate board and symmetrically located about the center line perpendicular to the wider side. Circular pads centered over the through holes on both sides of the board with a diameter of 3.048 mm are etched. The 4 pieces of the laminate boards are stacked with all of the through holes aligned,

and the resulting structure bound by nylon screws around the edges. Two 18 cm long 141 ISOCORE semi-rigid coaxial cables are used as vias. The outer conductor and dielectric over one third of the semi-rigid coaxial cables are removed. The bare inner conductor portion of each of these cables is inserted in and through one of the two holes in the stacked laminate structure from opposite sides, respectively. The outer portions are then placed back on the corresponding inner conductors extending from the stacked laminate structure. The outer conductors of the two cables are then soldered to the copper on both sides of the RT/Duroid. The lengths of the two cable segments on each side are different for convenience in measurement. SMA connectors are attached to the ends of the semi-rigid cables. The frequency range for the measurements extends up to 18 GHz, the limit of the performance of the cable and the connectors. The HP 8510B network analyzer system is used to measure the S parameters of the model.

The measurement data for transmission, reflection, near- and far-end coupling are shown with asterisks in Figure 3.14. In the same figure, the results obtained from the formulas presented in Section 3.2 are presented with solid lines. A good agreement between the calculation and the measurement is observed for the transmission $|S_{21}|$, reflection $|S_{11}|$, and far-end coupling $|S_{41}|$. The maximum deviation between the calculated and the measured near-end coupling, $|S_{31}|$, is about 2.3 dB. Since the signal level of the near-end coupling is low (-25 dB below the excitation at high frequencies), any slight imperfections in the experimental model can cause reflection or scattering loss of the same order. An additional factor affecting the accuracy of the measurement is caused by the use of an extra right-angle semi-rigid cable segment,

which was imposed by the connector size and the small spacing of the vias when measuring S_{31}. These effects will be more severe at high frequencies.

The measurements validate the mathematical model and the formulas derived in Section 3.2. These reliably predict the responses in the frequency and time domain for adjacent vias with different configurations and sizes without the need for performing difficult, sometimes impossible, measurements on an actual multilayer integrated circuit substrate or module.

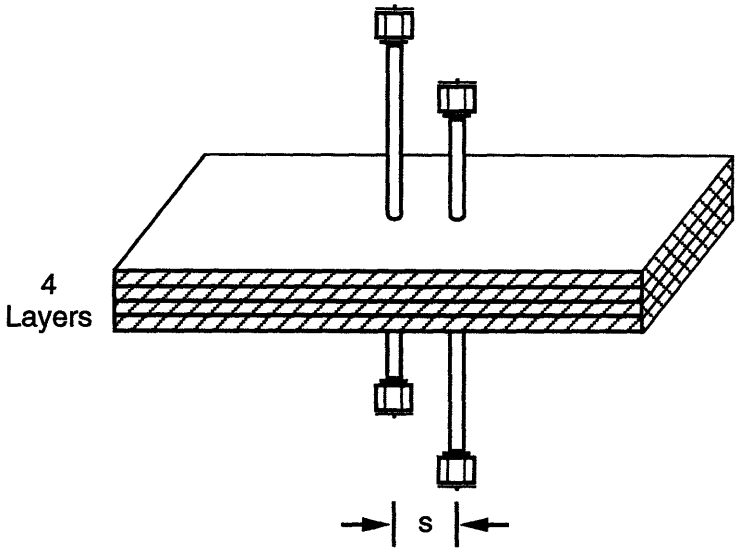

Figure 3.13: Configuration of experimental model.

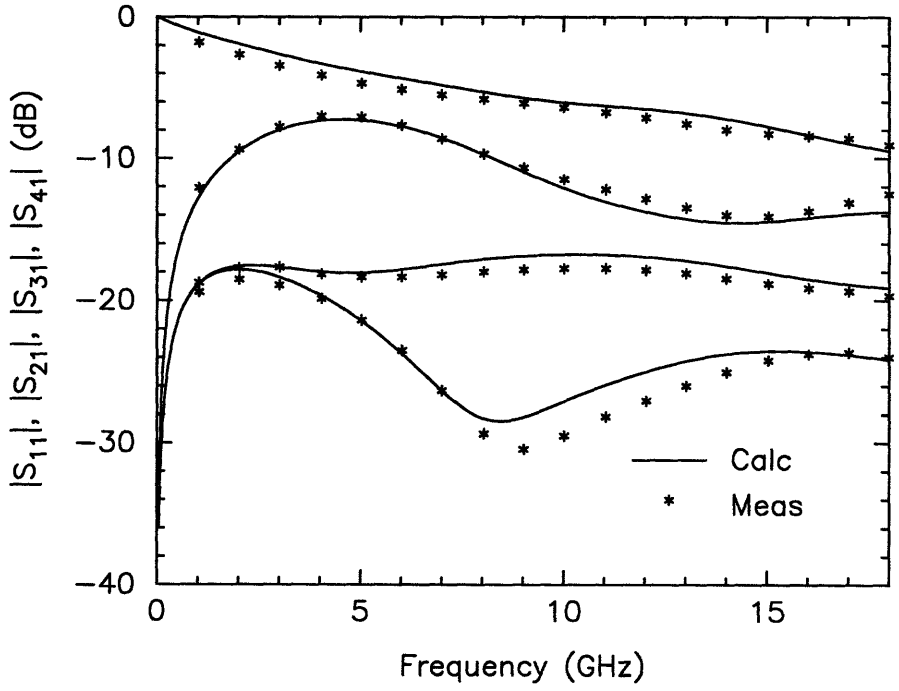

Figure 3.14: Comparison of measured and calculated S parameters.

3.6 Conclusions

An efficient method for analyzing coupling noises on adjacent vias has been developed by using equivalent magnetic frill array models and the even- and odd-mode analysis technique. For two adjacent vias, the closed-form formulas for the reflection and the transmission on the active via and for the near-end and far-end coupled noise on the passive via are analytically derived. The validity of these formulas has been confirmed by measurements. The frequency range over which the formulas are validated depends on the properties of the substrate material and dimensions of the structure. Usually, the applicable frequency range is wider when the dimensions of the via structure are smaller. For the vias used in our experiment, the applicable frequency covers DC to at least 18 GHz.

The analysis and numerical calculations lead to the following conclusions. The coupled noise increases with the number of layers and the dielectric constant of the substrate material, and decreases with increase in spacing between two adjacent vias. The far-end coupling first increases with number of layers at low frequencies and then decreases at high frequencies. The increase at low frequencies is due to the increase in length of the coupled region. At the higher frequencies the increase in coupled energy conversion to the radial waveguide modes causes a reduction in the far-end coupling.

Chapter 4

Analysis of Nonuniform Multiconductor Transmission Line Systems – Wave Transmission Matrix Method

4.1 Introduction

In very large scale integrated digital circuits and systems, multiconductor transmission lines are commonly used as signal interconnections between chips, chip carriers, circuit boards, or subsystems. As the operating speed of the circuits and the systems increases, the behavior of the multiconductor transmission lines employed as high speed signal carriers will have significant impact on the performance of the circuits or the systems. A multiconductor transmission line usually consists of cylindrical and/or strip conductors embedded in an inhomogeneous medium and one or several of the conductors serving as the ground. Inhomogeneous transmission lines can not support pure TEM waves but quasi-TEM waves at low frequencies. Even if the medium is homogeneous, at higher frequencies due to the conducting loss and higher order mode

propagation, the lines are not TEM in nature. Since a rigorous analysis of a multiconductor transmission line is very involved, the analyses in most of previous works and in the following sections are based on the quasi-TEM approximation. In fact, we have seen that this is a very good approximation when the transverse dimensions of the line are small as compared with the operating wavelength [20]–[30]. In addition to simplifying the analysis of the multiconductor lines, the quasi-TEM approximation is also desirable for handling the line terminations. These are usually described by circuit quantities (voltages and currents) rather than by the more general field quantities [31]. However, as the frequency of operation gets higher, the modes start to deviate from the quasi-TEM modes and one must analyze the problem with rigorous full-wave approach.

The general approach to the analysis of the multiconductor line is as follows. The multiconductor line is characterized by developing transmission line parameter matrices, such as the capacitance, inductance, resistance and conductance matrices per unit length of the line. A mathematical model, i.e., a set of equations governing the behavior of the line system is then established. The equations are solved with the appropriate method, e.g., modal analysis, analytically or numerically. This way the system responses is obtained in the time and frequency domains through corresponding boundary conditions. In this chapter, we shall emphasize the method of analyzing the responses of the multiconductor transmission line in the frequency domain and assume that the parameter matrices of the line are available.

When the dominant mode in the multiconductor transmission lines is quasi-TEM, the line system in time or frequency domain can be fully described by the well

known telegrapher equations (also referred to as transmission line equations). For uniform multiconductor transmission lines, the corresponding telegrapher equations are most commonly solved by using the so-called modal analysis in the time domain or in the frequency domain. However, for a lossy or frequency-dependent line, usually the modal analysis in the frequency domain will be used, because in this case N different quasi-TEM modes propagating on a transmission line with N signal conductors and one ground conductor can be defined in the frequency domain only. In the modal analyses, the kernel of the approach is to decouple the telegrapher equations by utilizing the method of characteristics. The problem can then be solved directly or by network analysis methods for a given boundary condition. Other approaches for the analysis of the multiconductor transmission line are the equivalent circuit model techniques, and matrix parameter methods (Green's function methods). The modal analysis can not directly deal with nonuniform multiconductor line problems, but incorporating with other techniques, such as the perturbation method, iteration method, or the numerical method, it is still possible to use the modal analysis in the time domain for some nonuniform systems. However, the more efficient methods for handling the nonuniform transmission lines are the network matrix parameter methods [43]–[48] in the frequency domain and the spectral method [50] in the time domain.

In this chapter a method which is based on the wave transmission matrix to deal with the nonuniform multiconductor line system is presented. This method has not only the ability to handle nonuniformity, but also the advantage of handling nonlinearity in the terminations efficiently. The wave transmission matrix is employed

to characterize the multiconductor transmission lines. Therefore, the telegrapher equations can easily be turned into algebraic equations. The nonuniform transmission line is treated as many small segments of uniform transmission lines connected in cascade. The boundary conditions are formulated with linear loads in spectral domain and with nonlinear loads in time domain.

The details of the method will be described in Section 4.2. The treatment of the boundary conditions including nonlinear terminations will be discussed in Section 4.3. Calculation approach and numerical results will be presented in Section 4.4 and Section 4.5.

4.2 Analysis and Formulation

The general system configuration under consideration is shown in Figure 4.1. The system consists of multiconductor interconnection lines terminated with linear/nonlinear loads. In this section, we use the wave transmission matrix to characterize the multiconductor transmission lines. The boundary condition or termination will be considered in next section.

For lossy multiconductor transmission lines, the telegrapher equations in the frequency domain can be expressed as

$$\frac{\partial}{\partial z}\begin{bmatrix}\mathbf{V}\\ \mathbf{I}\end{bmatrix} = -\begin{bmatrix}\mathbf{0} & \mathbf{Z}\\ \mathbf{Y} & \mathbf{0}\end{bmatrix}\begin{bmatrix}\mathbf{V}\\ \mathbf{I}\end{bmatrix}. \tag{4.1}$$

$\mathbf{V}$ and $\mathbf{I}$ are the N dimensional voltage and current vectors on the N transmission lines, and $\mathbf{Z}$ and $\mathbf{Y}$ denote the $N \times N$ impedance and admittance matrices per unit

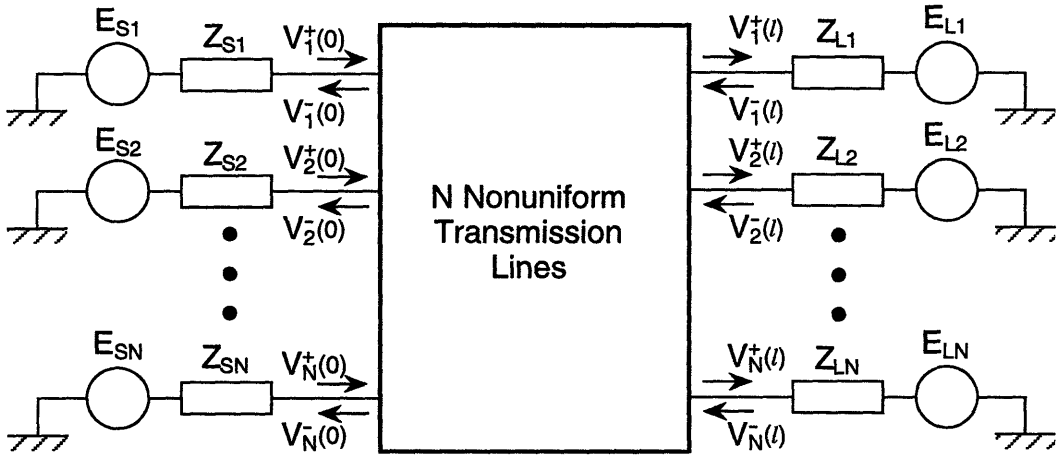

Figure 4.1: System configuration of multiconductor interconnection lines with linear/nonlinear loads.

length, respectively. The matrices $\mathbf{Z}$ and $\mathbf{Y}$ are symmetric. For uniform multiconductor lines, they are related to $N \times N$ resistance ($\mathbf{R}$), inductance ($\mathbf{L}$), conductance ($\mathbf{G}$), and capacitance ($\mathbf{C}$) real matrices per unit length as follows

$$\mathbf{Z} = \mathbf{R} + j\omega\mathbf{L} \tag{4.2}$$

$$\mathbf{Y} = \mathbf{G} + j\omega\mathbf{C} \tag{4.3}$$

Now, we define a forward-going and a backward-going voltage wave vectors, $\mathbf{V}^+$ and $\mathbf{V}^-$, as

$$\mathbf{V}^{\pm} = \mathbf{V} \pm \mathbf{Z}_0\mathbf{I}. \tag{4.4}$$

The voltage $\mathbf{V}$ and the current $\mathbf{I}$ are

$$\mathbf{V} = \frac{1}{2}\left(\mathbf{V}^{+} + \mathbf{V}^{-}\right) \tag{4.5}$$

$$\mathbf{I} = \frac{1}{2}\mathbf{Z}_0^{-1}\left(\mathbf{V}^{+} - \mathbf{V}^{-}\right) \tag{4.6}$$

where $\mathbf{Z}_0$ is defined in any of the following equivalent forms

$$\mathbf{Z}_0 = (\mathbf{ZY})^{1/2}\,\mathbf{Y}^{-1} = (\mathbf{ZY})^{-1/2}\,\mathbf{Z}. \tag{4.7}$$

After substituting (4.5) and (4.6) into (4.1) and some mathematical manipulation we obtain the wave transmission equations

$$\frac{\partial}{\partial z}\begin{bmatrix}\mathbf{V}^{+}\\ \mathbf{V}^{-}\end{bmatrix} = \frac{1}{2}\begin{bmatrix} -\left(\mathbf{ZZ}_0^{-1} + \mathbf{Z}_0\mathbf{Y}\right) & \left(\mathbf{ZZ}_0^{-1} - \mathbf{Z}_0\mathbf{Y}\right) \\ -\left(\mathbf{ZZ}_0^{-1} - \mathbf{Z}_0\mathbf{Y}\right) & \left(\mathbf{ZZ}_0^{-1} + \mathbf{Z}_0\mathbf{Y}\right)\end{bmatrix}\begin{bmatrix}\mathbf{V}^{+}\\ \mathbf{V}^{-}\end{bmatrix}. \tag{4.8}$$

It is easy to prove that the diagonal elements of the 2×2 block-partitioned matrix on the right-hand side of (4.8) are $-(\mathbf{ZY})^{1/2}$ and $(\mathbf{ZY})^{1/2}$, and the off-diagonal elementary matrices equal zero. Equation (4.8) can be rewritten as

$$\frac{\partial}{\partial z}\begin{bmatrix}\mathbf{V}^{+}\\ \mathbf{V}^{-}\end{bmatrix} = \begin{bmatrix} -(\mathbf{ZY})^{1/2} & \mathbf{0} \\ \mathbf{0} & (\mathbf{ZY})^{1/2}\end{bmatrix}\begin{bmatrix}\mathbf{V}^{+}\\ \mathbf{V}^{-}\end{bmatrix} \tag{4.9}$$

where $\mathbf{0}$ denotes a matrix with all the elements being 0.

From (4.9), we can see that the forward-going wave vector $\mathbf{V}^{+}$ and the backward-going wave vector $\mathbf{V}^{-}$ are decoupled. This is only true for uniform multiconductor transmission lines. There exists coupling between these two wave vectors for nonuni-

form transmission lines, because a travelling wave in either direction is continuously reflected by the nonuniformity of the lines along the propagation direction.

The equations in (4.9) are first order derivative matrix equations. It is obvious that their solutions have the forms

$$\mathbf{V}^{+}(z) = \mathbf{V}_0^{+} \exp(-\mathbf{K}z) \tag{4.10}$$

$$\mathbf{V}^{-}(z) = \mathbf{V}_0^{-} \exp(\mathbf{K}z). \tag{4.11}$$

$\mathbf{V}_0^{\pm}$ are constant vectors to be determined by boundary conditions of the lines, and $\mathbf{K}$ is the propagation constant matrix of the line

$$\mathbf{K} = (\mathbf{ZY})^{1/2}. \tag{4.12}$$

The voltage wave vectors at any two positions, z_1 and z_2, on the transmission line are related through a wave transmission matrix. The vectors at z, $\mathbf{V}^{\pm}(z)$, therefore, can be obtained from the wave vectors at $z = 0$, $\mathbf{V}^{\pm}(0)$, through the following expression

$$\begin{bmatrix} \mathbf{V}^{+}(z) \\ \mathbf{V}^{-}(z) \end{bmatrix} = \begin{bmatrix} \mathbf{A}_{11}(z) & \mathbf{A}_{12}(z) \\ \mathbf{A}_{21}(z) & \mathbf{A}_{22}(z) \end{bmatrix} \begin{bmatrix} \mathbf{V}^{+}(0) \\ \mathbf{V}^{-}(0) \end{bmatrix}. \tag{4.13}$$

Here, $[\mathbf{A}_{ij}]$ is the wave transmission matrix of the transmission line segment between z and 0. The elementary matrices $\mathbf{A}_{ij}\,(i, j = 1, 2)$ in the wave transmission matrix

can be obtained by utilizing (4.10) and (4.11). They are

$$\begin{aligned}
\mathbf{A}_{11}(z) &= \exp(-\mathbf{K}z) = \mathbf{1} - \mathbf{K}\frac{z}{1!} + (\mathbf{K})^2\frac{z^2}{2!} \\
&\quad -(\mathbf{K})^3\frac{z^3}{3!} + \cdots + (-1)^k(\mathbf{K})^k\frac{z^k}{k!} + \cdots \\
\mathbf{A}_{12}(z) &= \mathbf{A}_{21}(z) = \mathbf{0} \qquad (4.14) \\
\mathbf{A}_{22}(z) &= \exp(\mathbf{K}z) = \mathbf{1} + \mathbf{K}\frac{z}{1!} + (\mathbf{K})^2\frac{z^2}{2!} \\
&\quad +(\mathbf{K})^3\frac{z^3}{3!} + \cdots + (\mathbf{K})^k\frac{z^k}{k!} + \cdots
\end{aligned}$$

where $\mathbf{1}$ is the unit matrix. The properties of the wave transmission matrix are very similar to the chain parameter matrix, the identities given in [43] are therefore also suitable for the wave transmission matrix.

A nonuniform multiconductor transmission line can be approximated by many small uniform line segments with different characteristic impedance matrix $\mathbf{Z}_{0k}$ ($k = 1, 2, \ldots, m$) connected in cascade. The wave transmission matrix $[\mathbf{A}_{ij}]$ for the whole multiconductor line can be expressed as a product of sub-wave-transmission-matrices $[\mathbf{A}_{k,ij}]$, each characterizing a small line segment, and impedance transition submatrices $[\mathbf{T}_{k,ij}]$

$$\begin{bmatrix} \mathbf{A}_{11} & \mathbf{A}_{12} \\ \mathbf{A}_{21} & \mathbf{A}_{22} \end{bmatrix} = \begin{bmatrix} \mathbf{A}_{m,11} & \mathbf{A}_{m,12} \\ \mathbf{A}_{m,21} & \mathbf{A}_{m,22} \end{bmatrix} \prod_{k=m-1;-1}^{1} \left(\begin{bmatrix} \mathbf{T}_{k,11} & \mathbf{T}_{k,12} \\ \mathbf{T}_{k,21} & \mathbf{T}_{k,22} \end{bmatrix} \begin{bmatrix} \mathbf{A}_{k,11} & \mathbf{A}_{k,12} \\ \mathbf{A}_{k,21} & \mathbf{A}_{k,22} \end{bmatrix} \right). \qquad (4.15)$$

$\mathbf{A}_{k,ij}$ $(i,j=1,2)$ have the same forms as (4.14), and they are

$$\begin{aligned}
\mathbf{A}_{k,11} &= \exp(-\mathbf{K}_k\Delta\ell_k) = \sum_{p=0}^{\infty}\frac{(-1)^p}{p!}(\mathbf{K}_k\Delta\ell_k)^p \\
\mathbf{A}_{k,12} &= \mathbf{A}_{k,21} = \mathbf{0} \\
\mathbf{A}_{k,22} &= \exp(\mathbf{K}_k\Delta\ell_k) = \sum_{p=0}^{\infty}\frac{1}{p!}(\mathbf{K}_k\Delta\ell_k)^p.
\end{aligned} \tag{4.16}$$

$\Delta\ell_k$ is the length of the kth uniform segment at $z=z_k$, and $\mathbf{K}_k$ is the propagation constant matrix of the kth segment. It can be expressed by the per-unit-length impedance and admittance matrices of the kth segment, $\mathbf{Z}_k$ and $\mathbf{Y}_k$, as

$$\mathbf{K}_k = \sqrt{\mathbf{Z}_k\mathbf{Y}_k}. \tag{4.17}$$

In (4.15), the elementary matrices $\mathbf{T}_{k,ij}$ in the impedance transition submatrices have the forms

$$\mathbf{T}_{k,11} = \mathbf{T}_{k,22} = \frac{1}{2}(\mathbf{Z}_{0,k}+\mathbf{Z}_{0,k+1})\mathbf{Z}_{0,k}^{-1} \tag{4.18}$$

and

$$\mathbf{T}_{k,12} = \mathbf{T}_{k,21} = \frac{1}{2}(\mathbf{Z}_{0,k}-\mathbf{Z}_{0,k+1})\mathbf{Z}_{0,k}^{-1} \tag{4.19}$$

where $\mathbf{Z}_{0,k}$ $(k=1,2,\ldots,m)$ is the characteristic impedance matrix of the kth uniform segment.

A Comparison of (4.15) with (4.13) shows that in the nonuniform case the off-diagonal elementary matrices $\mathbf{A}_{12}$ and $\mathbf{A}_{21}$ are nonzero. This means that there is

coupling between the forward-going and backward-going voltage waves, $\mathbf{V}^+$ and $\mathbf{V}^-$ due to reflection caused by the nonuniformities along the line. The coupling between forward- and backward-going waves will be weak if the nonuniformities are small.

In reality, uniform or nonuniform multiconductor transmission lines are usually terminated with linear and/or nonlinear loads. The solution for the multiconductor transmission line systems must be related to boundary conditions of the systems. The approaches for treating different boundary conditions is described in the next section.

4.3 Boundary Conditions

In the previous section the multiconductor transmission lines were characterized by the wave transmission matrix $\mathbf{A}$. In order to analyze the total response of the system, the terminations or boundary conditions need to be considered. In this section we formulate the boundary conditions with linear loads in spectral domain and with nonlinear loads in time domain.

We assume Thevenin equivalent voltage sources and impedances for the linear terminations of the multiconductor transmission line system of length ℓ as shown in Figure 4.1. The boundary conditions are

$$\mathbf{V}(0) = \mathbf{E}_S - \mathbf{Z}_S\mathbf{I}(0) \tag{4.20}$$

$$\mathbf{V}(\ell) = \mathbf{E}_L + \mathbf{Z}_L\mathbf{I}(\ell) \tag{4.21}$$

where $\mathbf{E}_S$ and $\mathbf{E}_L$ denote excitation voltage vectors at $z = 0$ and $z = \ell$, respec-

tively. $\mathbf{Z}_S$ and $\mathbf{Z}_L$ are $N \times N$ diagonal source and load impedance matrices at the corresponding ends.

For linear terminations, we can determine the boundary values of the forward- and backward-going voltage wave vectors from (4.20) and (4.21) using (4.5), (4.6) and (4.13). The final expressions of the boundary values $\mathbf{V}^+(0)$ and $\mathbf{V}^-(\ell)$ are

$$\begin{aligned}\mathbf{V}^+(0) &= [\mathbf{1} - \mathbf{\Gamma}_S\mathbf{A}_{22}^{-1}\mathbf{A}_{21} - \mathbf{\Gamma}_S\mathbf{A}_{22}^{-1}(\mathbf{1} + \mathbf{\Gamma}_L\mathbf{A}_{12}\mathbf{A}_{22}^{-1})^{-1}\mathbf{\Gamma}_L\mathbf{Z}_{0m}\mathbf{Z}_{01}^{-1}\mathbf{A}_{22}^{-1}]^{-1} \\ &\quad [\mathbf{T}_S\mathbf{E}_S - \mathbf{\Gamma}_S\mathbf{A}_{22}^{-1}(\mathbf{1} + \mathbf{\Gamma}_L\mathbf{A}_{12}\mathbf{A}_{22}^{-1})^{-1}\mathbf{T}_L\mathbf{E}_L)] \qquad (4.22)\end{aligned}$$

and

$$\begin{aligned}\mathbf{V}^-(\ell) &= [\mathbf{1} + \mathbf{\Gamma}_L\mathbf{A}_{22}^{-1}\mathbf{A}_{12} - \mathbf{\Gamma}_L\mathbf{Z}_{0m}\mathbf{Z}_{01}^{-1}\mathbf{A}_{22}^{-1}(\mathbf{1} - \mathbf{\Gamma}_S\mathbf{A}_{22}^{-1}\mathbf{A}_{21})^{-1}\mathbf{\Gamma}_S\mathbf{A}_{22}^{-1}]^{-1} \\ &\quad [\mathbf{T}_L\mathbf{E}_L - \mathbf{\Gamma}_L\mathbf{Z}_{0m}\mathbf{Z}_{01}^{-1}\mathbf{A}_{22}^{-1}(\mathbf{1} - \mathbf{\Gamma}_S\mathbf{A}_{22}^{-1}\mathbf{A}_{21})^{-1}\mathbf{T}_S\mathbf{E}_S)] \qquad (4.23)\end{aligned}$$

where $\mathbf{\Gamma}_{S,L}$ and $\mathbf{T}_{S,L}$ are

$$\mathbf{\Gamma}_{S,L} = \left(\mathbf{1} + \mathbf{Z}_{S,L}\mathbf{Z}_{01,0m}^{-1}\right)^{-1}\left(\mathbf{1} - \mathbf{Z}_{S,L}\mathbf{Z}_{01,0m}^{-1}\right) \qquad (4.24)$$

$$\mathbf{T}_{S,L} = 2\left(\mathbf{1} + \mathbf{Z}_{S,L}\mathbf{Z}_{01,0m}^{-1}\right)^{-1}. \qquad (4.25)$$

$\mathbf{Z}_{01}$ and $\mathbf{Z}_{0m}$ are the characteristic impedance matrices of the first and the last line segments. For the derivation of (4.22) and (4.23), the identity

$$\mathbf{A}_{11}\mathbf{A}_{22} - \mathbf{A}_{12}\mathbf{A}_{22}^{-1}\mathbf{A}_{21}\mathbf{A}_{22} = \mathbf{Z}_{0m}\mathbf{Z}_{01}^{-1} \qquad (4.26)$$

has been used.

The voltage wave vectors at any point z on the line can be obtained from (4.13) and the boundary values (4.22) and (4.23). They are

$$\begin{bmatrix} \mathbf{V}^+(z) \\ \mathbf{V}^-(z) \end{bmatrix} = \begin{bmatrix} \mathbf{A}_{11}(z) & \mathbf{A}_{12}(z) \\ \mathbf{A}_{21}(z) & \mathbf{A}_{22}(z) \end{bmatrix} \begin{bmatrix} \mathbf{1} & \mathbf{0} \\ -\mathbf{A}_{22}^{-1}(\ell)\mathbf{A}_{21}^{-1}(\ell) & \mathbf{A}_{22}^{-1}(\ell) \end{bmatrix} \begin{bmatrix} \mathbf{V}^+(0) \\ \mathbf{V}^-(\ell) \end{bmatrix} \tag{4.27}$$

where the matrix $[\mathbf{A}_{ij}(z)]$ is

$$\begin{aligned} \begin{bmatrix} \mathbf{A}_{11}(z) & \mathbf{A}_{12}(z) \\ \mathbf{A}_{21}(z) & \mathbf{A}_{22}(z) \end{bmatrix} &= \begin{bmatrix} \mathbf{A}_{m_1,11} & \mathbf{A}_{m_1,12} \\ \mathbf{A}_{m_1,21} & \mathbf{A}_{m_1,22} \end{bmatrix}\Bigg|_{m_1=z/\Delta\ell} \\ &\cdot \prod_{k=m_1-1;-1}^{1} \left(\begin{bmatrix} \mathbf{T}_{k,11} & \mathbf{T}_{k,12} \\ \mathbf{T}_{k,21} & \mathbf{T}_{k,22} \end{bmatrix} \begin{bmatrix} \mathbf{A}_{k,11} & \mathbf{A}_{k,12} \\ \mathbf{A}_{k,21} & \mathbf{A}_{k,22} \end{bmatrix} \right) \end{aligned} \tag{4.28}$$

These results are in frequency domain and evaluations have to be performed for each frequency separately. The time response of the voltages can then be obtained by means of the Fourier transform.

For nonlinear terminations of the multiconductor transmission lines, the analysis of boundary conditions utilizes the incident wave $\mathbf{V}^{inc}$, and the reflected wave $\mathbf{V}^{ref}$, which are related by the scattering wave matrix $\mathbf{S}$ as

$$\mathbf{V}^{ref} = \mathbf{S}\mathbf{V}^{inc}. \tag{4.29}$$

In terms of elementary scattering matrices this is

$$\begin{bmatrix} \mathbf{V}^{ref}(0) \\ \mathbf{V}^{ref}(\ell) \end{bmatrix} = \begin{bmatrix} \mathbf{S}_{11} & \mathbf{S}_{12} \\ \mathbf{S}_{21} & \mathbf{S}_{22} \end{bmatrix} \begin{bmatrix} \mathbf{V}^{inc}(0) \\ \mathbf{V}^{inc}(\ell) \end{bmatrix} \tag{4.30}$$

where $V^{inc}(0)$ and $V^{inc}(\ell)$ are the incident voltage wave vectors at $z = 0$ and $z = \ell$, and $V^{ref}(0)$ and $V^{ref}(\ell)$ are the reflected voltage wave vectors at $z = 0$ and $z = \ell$. The $\mathbf{S}_{ij}$ are related to the elementary wave transmission matrices $\mathbf{A}_{ij}$ as

$$\begin{aligned}
\mathbf{S}_{11} &= -\mathbf{A}_{22}^{-1}\mathbf{A}_{21} \\
\mathbf{S}_{12} &= \mathbf{A}_{22}^{-1} \\
\mathbf{S}_{21} &= \mathbf{A}_{11} - \mathbf{A}_{12}\mathbf{A}_{22}^{-1}\mathbf{A}_{21} \\
\mathbf{S}_{22} &= \mathbf{A}_{12}\mathbf{A}_{22}^{-1}
\end{aligned}$$

The relation between the reflected and incident voltage vector in frequecy domain (4.29) can be written in time domain as

$$\mathbf{v}^{ref} = \mathbf{h} * \mathbf{v}^{inc} \tag{4.31}$$

where $\mathbf{h}$ is the inverse Fourier transform of the scattering matrix $\mathbf{S}$ and asterisk denotes convolution with respect to time. Lower case letters are used to denote time domain variables.

Consider the N nonuniform transmission lines, where each line is terminated by a voltage source and a load. Using the relationship of the incident and reflected wave with the current and voltage, the expressions

$$\mathbf{v}^{inc} = \mathbf{v}' + \mathbf{e} - \mathbf{z} * \mathbf{i} \tag{4.32}$$

$$\mathbf{v}^{ref} = \mathbf{v}' + \mathbf{e} + \mathbf{z} * \mathbf{i} \tag{4.33}$$

can be obtained. $\mathbf{v}'$ is the voltage vector across the loads, $\mathbf{e}$ is the voltage source vector, $\mathbf{i}$ is the current vector and each of its elements is a function of the corresponding element of $\mathbf{v}'$. The matrix $\mathbf{z}$ is the inverse Fourier transform of the diagonal impedance matrix characterizing the terminal impedance lines. The first N diagonal elements of $\mathbf{z}$ correspond to the impedances of the terminal lines connected to the first segments of the transmission lines; the latter N elements correspond to the impedances of the terminal lines connected to the last segments.

To solve the equations (4.31)–(4.33) numerically, we discretize the time variable and convert the convolution integrals into summation. After some manipulation, we obtain

$$\mathbf{v'}_k = -\mathbf{e}_k + [\mathbf{1} - \mathbf{h}_0]^{-1} \left\{ \sum_{m=0}^{k-1} \mathbf{h}_{k-m} \mathbf{v}_m^{inc} - [\mathbf{1} + \mathbf{h}_0] \sum_{m=0}^{k} \mathbf{z}_{k-m} \mathbf{i}_m \right\}. \tag{4.34}$$

In the above equation, the subscripts denote the discretized time step, for instant $\mathbf{v'}_k = \mathbf{v}'(k\Delta t)$, where Δt is the time step. Equation (4.34) is a set of nonlinear algebraic equations, which can be solved by means of the Newton–Raphson technique. The incident voltage used in equation (4.34) can be obtained from

$$\mathbf{v}_k^{inc} = \mathbf{v'}_k + \mathbf{e}_k - \sum_{m=0}^{k} \mathbf{z}_{k-m} \mathbf{i}_m. \tag{4.35}$$

The above formulation also works for linear loads where the current is the ratio of v' to the load impedance.

4.4 Computational Considerations

The major part in the numerical implementation of this method consists of various matrix operations and manipulations, including calculation of matrix functions such as square-root and exponential functions.

In the calculation of wave transmission matrix, the square-root of a matrix has to be evaluated as in (4.12). A formal approach to carry out this operation is to transform the matrix into a diagonalized matrix, i.e., to use the method of characteristics. Define a matrix $\mathbf{X}$ to be the square-root of $\mathbf{ZY}$ as

$$\mathbf{ZY} = \mathbf{XX} \tag{4.36}$$

Assume that the eigenvalues and eigenvectors of $\mathbf{ZY}$ are β_i^2 and $\mathbf{D}_i$, respectively. They have the following relationship

$$\mathbf{D}^{-1}\mathbf{ZYD} = \mathrm{diag}[\beta_i^2] \tag{4.37}$$

where $\mathbf{D}$ is a matrix consisting of the eigenvectors $\mathbf{D}_i$, i.e., $\mathbf{D} = [\mathbf{D}_1, \mathbf{D}_2, \ldots, \mathbf{D}_N]$. Substituting (4.36) into (4.37), we obtain

$$\mathrm{diag}[\beta_i^2] = \mathbf{D}^{-1}\mathbf{ZYD} = \mathbf{D}^{-1}\mathbf{XDD}^{-1}\mathbf{XD}. \tag{4.38}$$

From above, $(\mathbf{ZY})^{1/2}$ is obtained as

$$\mathbf{X} = (\mathbf{ZY})^{1/2} = \mathbf{D}\,\mathrm{diag}[\beta_i]\,\mathbf{D}^{-1}. \tag{4.39}$$

In general, a matrix function can be defined and calculated by

$$f(\mathbf{W}) = \mathbf{D}\,\mathrm{diag}[f(\lambda_1), f(\lambda_2), \ldots, f(\lambda_N)]\,\mathbf{D}^{-1} \tag{4.40}$$

where $f(\cdot)$ denotes a function, such as square root and/or exponential function, and λ_i is the eigenvalue and $\mathbf{D}$ is the matrix consisting of eigenvectors of matrix $\mathbf{W}$.

The elementary matrices $\mathbf{A}_{ij}$ $(i,j = 1,2)$ defined by (4.16) can be calculated directly by a series expansion. The matrix series are absolutely convergent and their convergence rates depend upon the magnitude of eigenvalues of $\sqrt{\mathbf{Z}_k\mathbf{Y}_k}$, $\beta_{k,i}\,(i = 1,2,\ldots,N)$, and the length $\Delta\ell_k$ of the line segments. The smaller the product $|\beta_{k,i}|\Delta\ell_k$, the higher the convergence rate. Therefore, in order to obtain high convergence rate we need to divide the uniform/nonuniform line into large number of short segments, which is computationally expensive. The exponential matrix functions can also be calculated using equation (4.40), as in the calculation of square-root function. However the latter requires the calculation of the eigenvectors of the matrix, a very time consuming numerical procedure.

An alternative approach to calculate the elementary matrices is to make use of Sylvester's formula [51]. If an $N \times N$ matrix $\mathbf{W}$ has N distinct eigenvalues, a function of matrix $\mathbf{W}$ can then be calculated by

$$f(\mathbf{W}) = \sum_{r=1}^{N} f(\lambda_r)\mathbf{Z}_r \tag{4.41}$$

where λ_r are eigenvalues of matrix $\mathbf{W}$, and $\mathbf{Z_r}$ are $N \times N$ matrices given by

$$\mathbf{Z}_r = \prod_{\substack{i=1 \\ i \neq r}}^{N} \frac{\mathbf{W} - \lambda_i \mathbf{1}}{\lambda_r - \lambda_i}. \tag{4.42}$$

The matrices $\mathbf{Z}_r$ satisfy the following relations

$$\sum_{r=1}^{N} \mathbf{Z}_r = \mathbf{1}, \quad \text{and} \quad \mathbf{Z}_r \mathbf{Z}_s = \mathbf{0} \quad (r \neq s). \tag{4.43}$$

The approach of using equation (4.41) avoids the calculation of the eigenvectors and, since it uses the exact formula (4.40) instead of series expansion, it also avoids the problem of convergence. It is therefore numerically much more simpler and faster. Moreover, by using (4.41) in the calculation of the elementary matrix $\mathbf{A}_{ij}$, the manipulation of square-root and exponential of the matrix $\sqrt{\mathbf{Z}_k \mathbf{Y}_k}$ can be combined and accomplished in one procedure. For the cases of coupled microstrip lines, the eigenvalues which correspond to coupled modes of the structures are always non-degenerate due to the coupling effect. In our numerical implementation, both approaches are used, if the eigenvalues of the matrix product $\mathbf{ZY}$ are distinct. The same results are obtained, while the Sylvester's formula significantly reduces the computation time.

To validate the present method and its numerical implementation, we consider a pair of symmetric nonuniformly coupled lines. For this case, the elementary matrices in (4.16) and (4.17) are 2×2 and can be calculated analytically. Assume a pair of

nonuniform transmission lines with impedance matrix $\mathbf{Z}$ and admittance matrix $\mathbf{Y}$

$$\mathbf{Z} = \begin{bmatrix} R(z) & 0 \\ 0 & R(z) \end{bmatrix} + j\omega \begin{bmatrix} L(z) & L_m(z) \\ L_m(z) & L(z) \end{bmatrix} \tag{4.44}$$

and

$$\mathbf{Y} = \begin{bmatrix} G(z) & 0 \\ 0 & G(z) \end{bmatrix} + j\omega \begin{bmatrix} C(z) & C_m(z) \\ C_m(z) & C(z) \end{bmatrix}. \tag{4.45}$$

Then the square root of $\mathbf{ZY}$ can be obtained by

$$\mathbf{K} = \sqrt{\mathbf{ZY}} = \frac{1}{2} \begin{bmatrix} \gamma_+ + \gamma_- & \gamma_+ - \gamma_- \\ \gamma_+ - \gamma_- & \gamma_+ + \gamma_- \end{bmatrix} \tag{4.46}$$

where γ_+ and γ_- are the eigenvalues of $\mathbf{K}$ given by

$$\gamma_+ = \sqrt{[R(z) + j\omega(L(z) + L_m(z))][G(z) + j\omega(C(z) + C_m(z))]} \tag{4.47}$$

and

$$\gamma_- = \sqrt{[R(z) + j\omega(L(z) - L_m(z))][G(z) + j\omega(C(z) - C_m(z))]}. \tag{4.48}$$

The characteristic impedance matrix $\mathbf{Z_0} = \sqrt{\mathbf{ZY}}\ \mathbf{Y}^{-1}$ will be

$$\mathbf{Z}_0 = \frac{1}{2} \begin{bmatrix} \frac{G+j\omega C}{\Delta C}(\gamma_+ + \gamma_-) - \frac{j\omega C_m}{\Delta C}(\gamma_+ - \gamma_-) & \frac{G+j\omega C}{\Delta C}(\gamma_+ - \gamma_-) - \frac{j\omega C_m}{\Delta C}(\gamma_+ + \gamma_-) \\ \frac{G+j\omega C}{\Delta C}(\gamma_+ - \gamma_-) - \frac{j\omega C_m}{\Delta C}(\gamma_+ + \gamma_-) & \frac{G+j\omega C}{\Delta C}(\gamma_+ + \gamma_-) - \frac{j\omega C_m}{\Delta C}(\gamma_+ - \gamma_-) \end{bmatrix} \tag{4.49}$$

where

$$\Delta C = (G + j\omega C)^2 + \omega^2 C_m^2.$$

For this example, we use the same parameters as those of Figure 8 in [24]. The total length of the line is 1 cm. The elements of matrices $\mathbf{Z}$ and $\mathbf{Y}$ in (4.44) and (4.45) are

$$\begin{aligned} L(z) &= 5.73(1 - k_L(z)) \qquad \text{(nH/cm)} \\ L_m(z) &= k_L(z)L(z) \qquad \text{(nH/cm)} \\ C(z) &= 1.81(1 + k_C(z)) \qquad \text{(pF/cm)} \\ C_m(z) &= -k_C(z)C(z) \qquad \text{(pF/cm)} \\ k_C(z) &= 0.2 - 0.05[1 - \cos(2\pi z)] \\ k_L(z) &= 0.2 \\ R(z) &= G(z) = 0 \end{aligned} \tag{4.50}$$

A pulse source with amplitude 10 V, rise and fall time of 10 ps, and a duration of 20 ps is imposed on one end of the lines and all the ends are terminated with 50 Ω loads. The time waveforms of the voltage at each end are given in Figure 4.2. These results compare very well with those of [24], especially for the near end and far end coupling noises. The numerical calculations were checked with cases where exact solutions could be obtained.

4.5 Numerical Examples

In this section several examples of nonuniform multiconductor microstrip lines with linear or nonlinear terminations are considered. In the analysis of any transmission line system we first need to construct the impedance matrix $\mathbf{Z}$ and admittance matrix $\mathbf{Y}$, as defined in (4.2) and (4.3) by the resistance ($\mathbf{R}$), inductance ($\mathbf{L}$), conductance ($\mathbf{G}$), and capacitance ($\mathbf{C}$) matrices. Many methods have been developed to calculate the impedance and admittance of microstrip lines. The formulation developed in the previous sections does not depend on the method that those parameter matrices are calculated. Moreover, by introducing different effects in the parameter matrices, the same effects can be incorporated into the system signal responses. For example, if the inductance and capacitance are calculated as frequency dependent, then the dispersion can be included. If the skin effects are considered in the calculation of resistance and conductance, then the overall losses as a function of frequency can be determined. In the following examples, we calculated the inductance and capacitance in a way similar to that of [54]. The resistance and conductance are calculated by the strip cross section and the metal conductivity.

As a first example, the nonuniform coupled interconnection, given in example 5 of [50] is analyzed. Figure 4.3 depicts the geometry and terminations of the lossless tapered coupled lines under consideration. A ramp function with a rise time of 100 ps and an amplitude of 1 V is applied on the active line. Initially, we employed a frequency bandwidth from DC to 100 GHz, and obtained the time waveforms on the active and passive lines shown in Figure 4.4 and Figure 4.5, respectively. A comparison with the results in [50] and [52] shows that our waveforms are sharper

than those. As the frequency bandwidth is decreased, e.g., to 15 GHz, the resulting waveforms become smoother (Figure 4.6 and Figure 4.7). In the calculation, we use 80 uniform segments with equal lengths to approximate the nonuniform region of this coupled interconnection. The CPU time is 3 minutes on a DECstation 3100 for the case of 100 GHz bandwidth with 500 frequency samples.

As discussed in Section 4.3, multiple line system with nonlinear terminations can be analyzed efficiently in terms of scattering matrix and the corresponding impulse responses in time domain. As the second example, we consider the case of two lossy uniform transmission line with nonlinear terminations. The line length is 0.5 m. In order to check our results, we used the same **L**,**C**, **R** and **G** parameter matrices and nonlinear load as those given in [44]. The paramater matrices at 1 MHz are

$$\mathbf{L} = \begin{bmatrix} 309 & 21.7 \\ 21.7 & 309 \end{bmatrix} \text{ nH/m}$$

$$\mathbf{C} = \begin{bmatrix} 144 & -6.4 \\ -6.4 & 144 \end{bmatrix} \text{ pF/m}$$

$$\mathbf{R} = \begin{bmatrix} 524 & 33.9 \\ 33.9 & 524 \end{bmatrix} \text{ m}\Omega\text{/m}$$

$$\mathbf{G} = \begin{bmatrix} 905 & -11.8 \\ -11.8 & 905 \end{bmatrix} \text{ nS/m.}$$

The resistances were assumed to vary proportionally to the square root of frequency, and the conductances proportionally to the first power of frequency. At one line end, one conductor is driven by a 50–Ω voltage generator with a trapezoidal pulse of 5 ns duration and rise and fall time of 0.5 ns, while the other conductor is terminated by a 75–Ω load. At the other end the line is terminated by two nonlinear

resistive circuits, each of them being a series combination of a 10–Ω resistor and a nonlinear resistor. The current through the nonlinear resistors were assumed to be given by $I = 10(e^{V/V_T} - 1)$ nA, where $V_T = 25$ mV. Figure 4.8 shows the near-end and far-end voltage responses on the active line and Figure 4.9 those on the parasitic line. Our results match very well with that of [44]. This further confirms that our method is efficient and valid for solving multiconductor lines with nonlinear termination.

In the following example, a system with three nonuniform microstrip lines with both linear and nonlinear terminations is analyzed. The transmission line system and the cross section of the microstrip are depicted in Figure 4.10. The thickness of the metal strip is assumed to be $t = 5$ μm. The surface resistance of the metal strip is $R = 30$ m$\Omega/\square$. The nonuniform microstrip line is divided into 50 uniform segments. The incidence voltage is a step function with an amplitude of 1 V.

First, we calculate the linear load case where all ends are terminated with 50 Ω resistors. Figure 4.11 shows the near-ends response voltages and Figure 4.12 shows the far-end responses. These results compare very well with those given in [53], even though the **L**,**C**, **R** and **G** matrices are calculated differently and the strip thickness is not given in [53]. Next, we replace the active line's far-end termination (port 4) by a nonlinear load keeping the rest of the system parameters unchanged. The current through the nonlinear load is characterized by $I = (e^{V/V_T} - 1)$ mA, where $V_T = 25$ mV. In Figure 4.13 and Figure 4.14, the voltage waveforms on the far and near end terminals of the three lines are shown. Comparing Figure 4.13–Figure 4.14 with Figure 4.11–Figure 4.12, we can see the effect of the nonlinear load not only at port 4, but also at other ports.

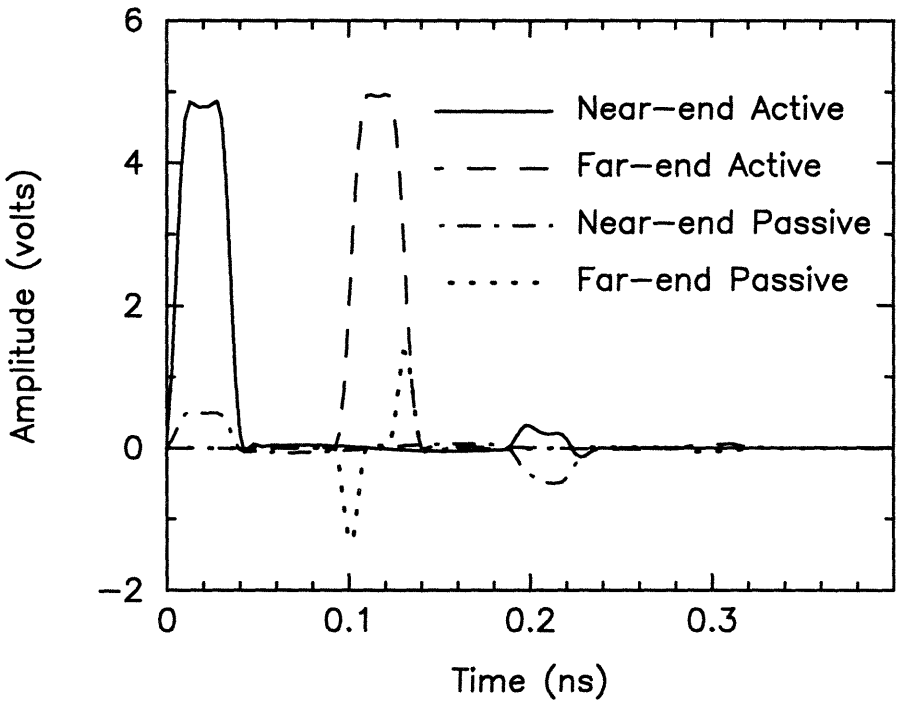

Figure 4.2: Time waveforms of transmitted signal, near end noise and far end noise on the coupled lines with parameters given by (4.50).

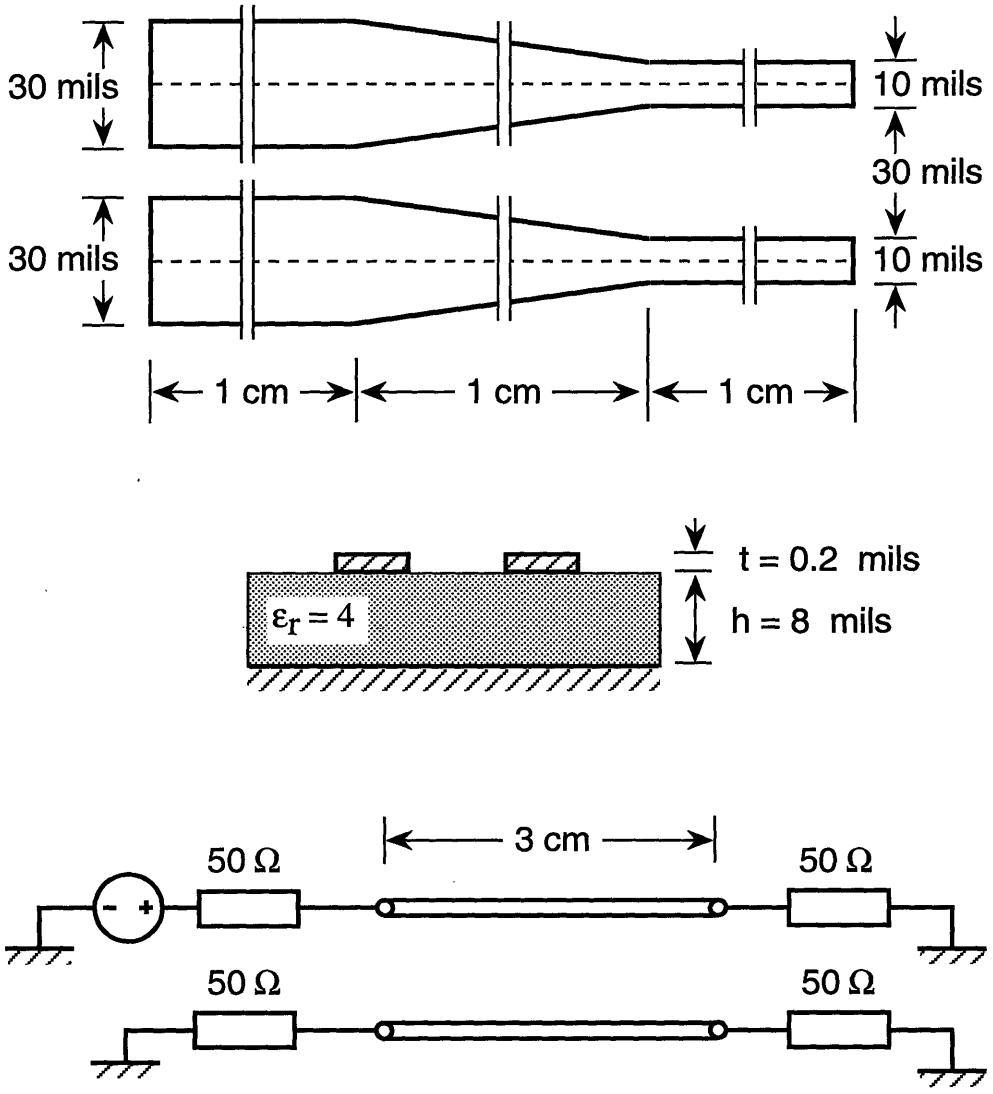

Figure 4.3: Configuration of the tapered lossless coupled transmission line with linear loads, top view, geometry of cross section and circuit configuration.

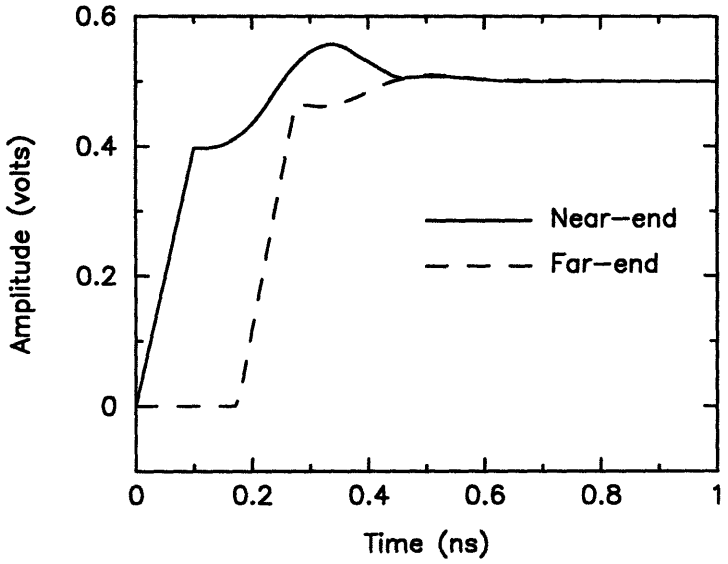

Figure 4.4: Time waveforms on the active line of two coupled nonuniform lines with a frequency bandwidth from DC to 100 GHz.

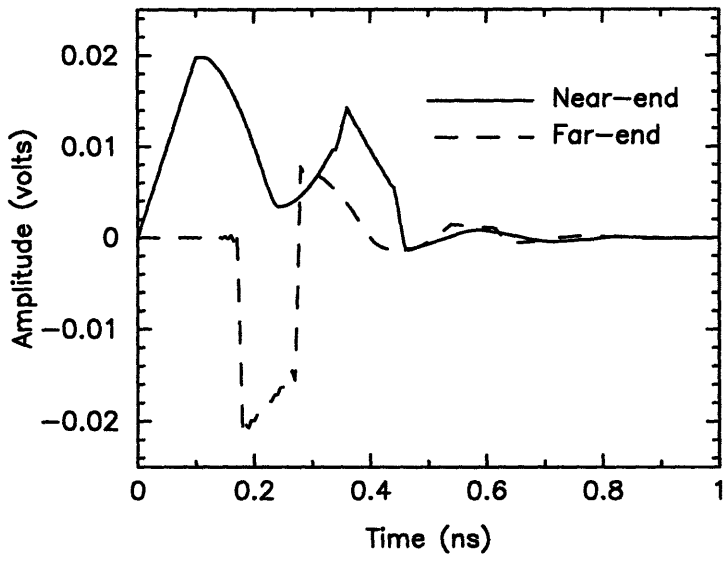

Figure 4.5: Time waveforms on the passive line of two coupled nonuniform lines with a frequency bandwidth from DC to 100 GHz.

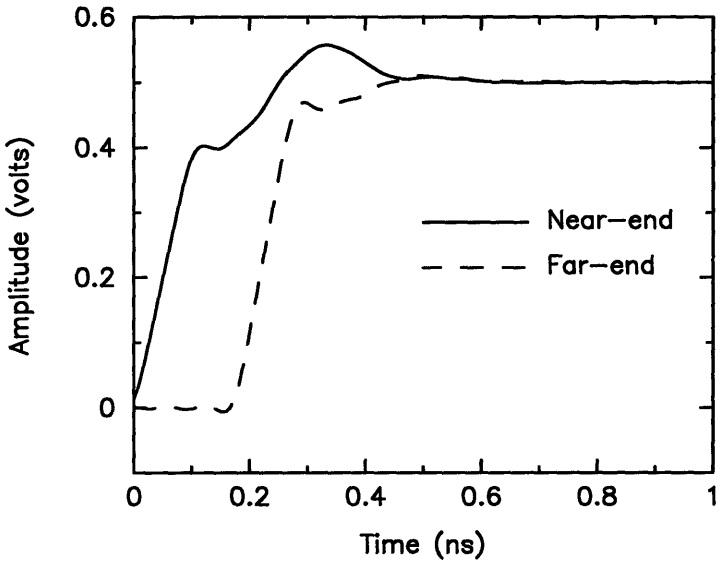

Figure 4.6: Time waveforms on the active line of two coupled nonuniform lines with a frequency bandwidth from DC to 15 GHz.

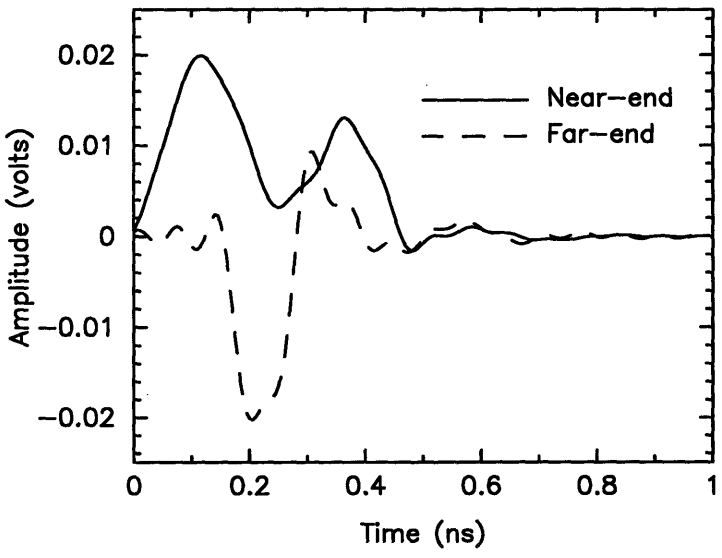

Figure 4.7: Time waveforms on the passive line of two coupled nonuniform lines with a frequency bandwidth from DC to 15 GHz.

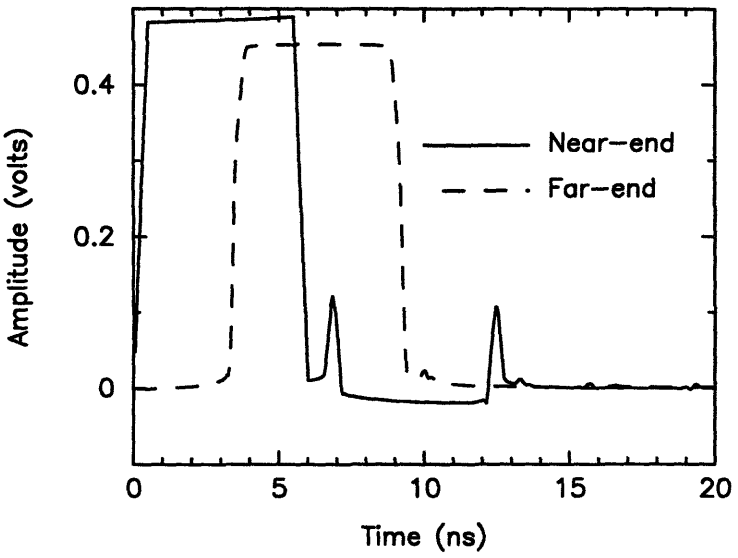

Figure 4.8: Time waveforms on the active line of two coupled lines with nonlinear terminations.

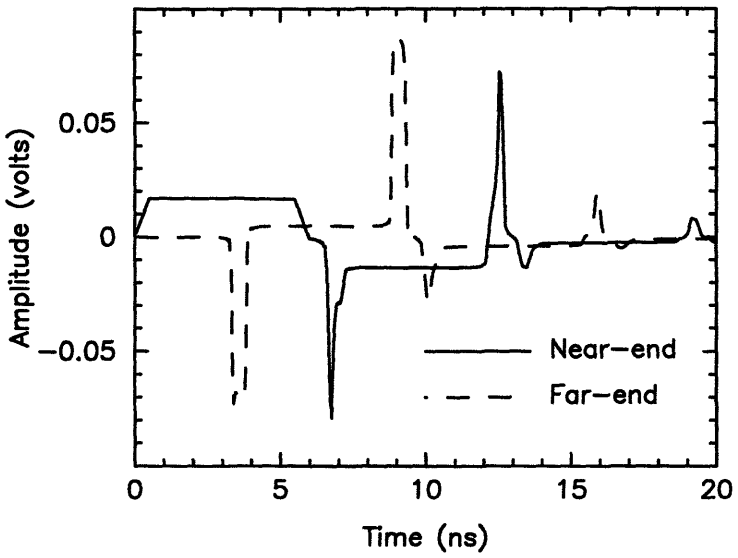

Figure 4.9: Time waveforms on the passive line of two coupled lines with nonlinear terminations.

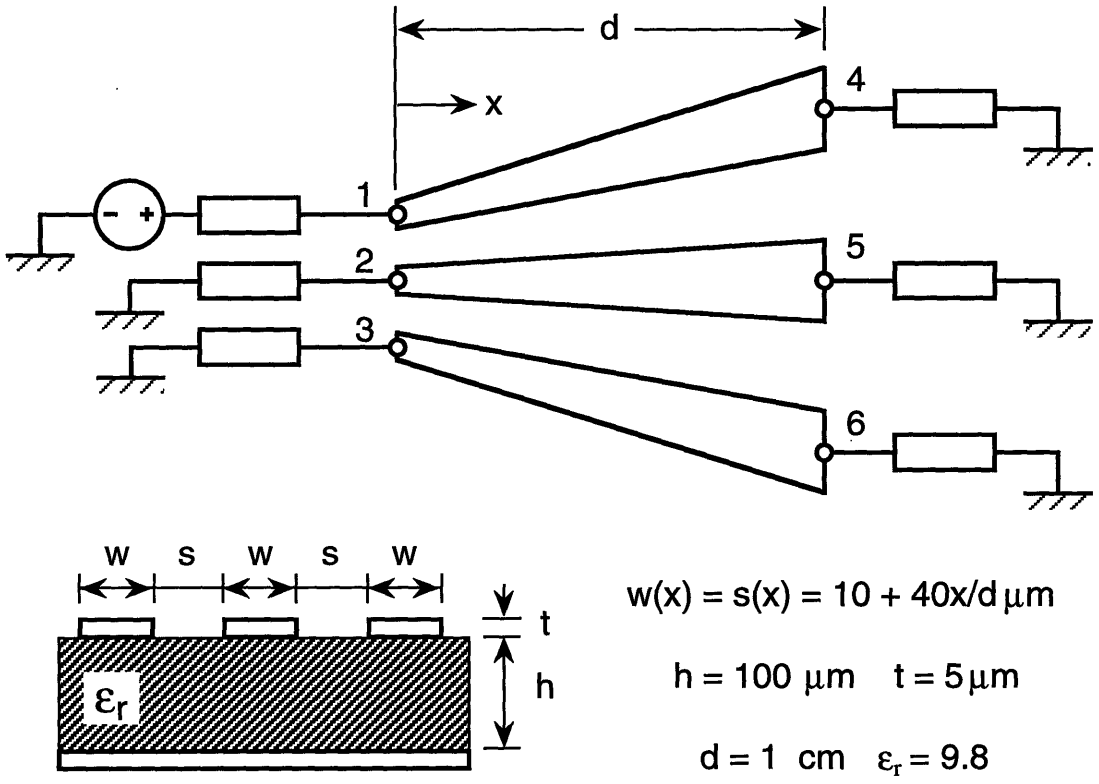

Figure 4.10: Configuration of three nonuniform microstrip system with linear or nonlinear loads.

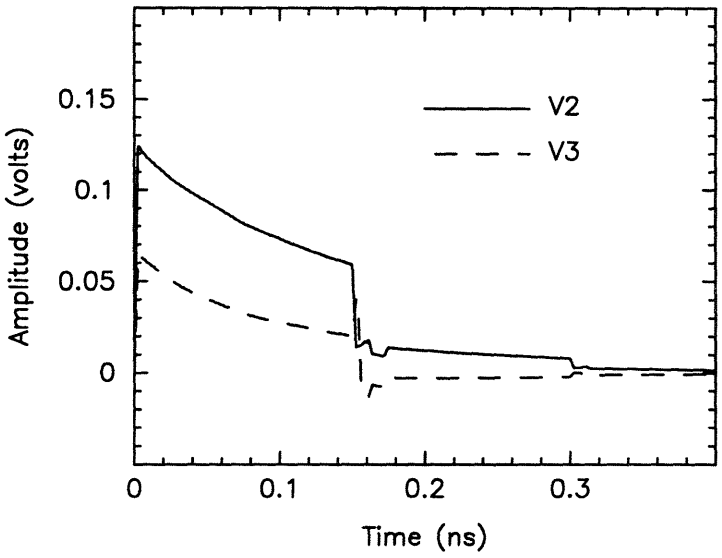

Figure 4.11: Near-end response voltages with linear loads for the three nonuniform transmission line system.

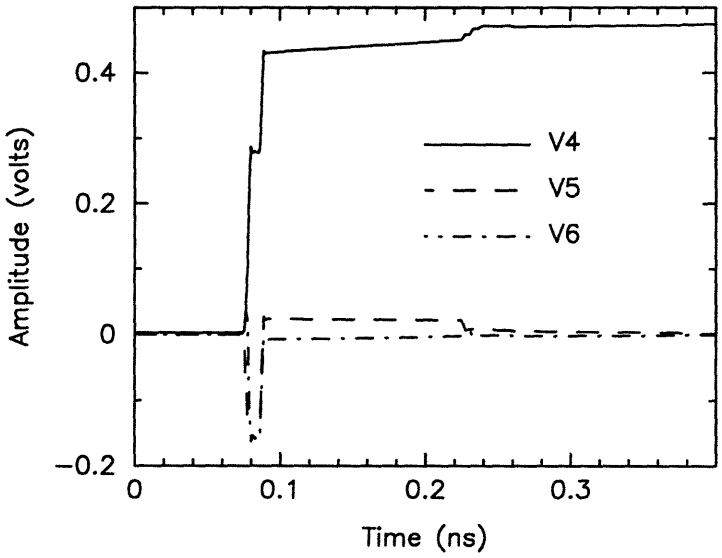

Figure 4.12: Far-end response voltages with linear loads the three nonuniform transmission line system.

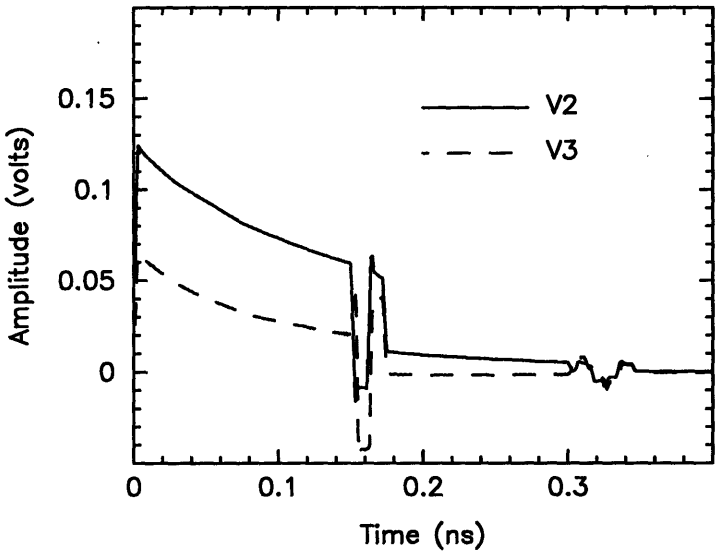

Figure 4.13: Near-end response voltages with nonlinear loads the three nonuniform transmission line system.

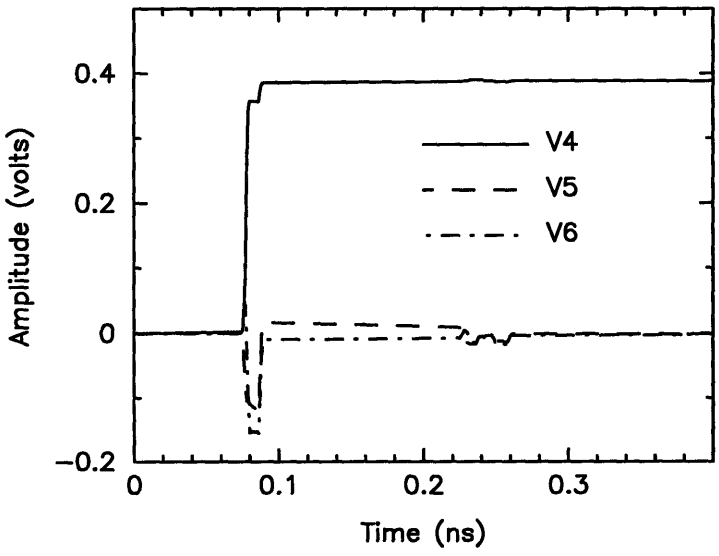

Figure 4.14: Far-end response voltages with nonlinear loads the three nonuniform transmission line system.

4.6 Conclusions

A method based on the wave transmission matrix is developed to deal with nonuniform multiconductor transmission lines. One of the advantages of this method is the flexibility of handling a variety of nonuniform multiline structures, because in most cases it is possible to approximate a nonuniform multiline by small segments of uniform multiline connected in cascade. The total wave transmission matrix is then the product of all the submatrices representing each small uniform segment. The other virtue is that uniform or weak nonuniform multilines will have diagonalized wave transmission matrices.

This method uses the forward and backward going waves rather than voltage and current. It is consistent with the method of solving nonlinear problems in terms of the scattering matrix and the corresponding impulse responses [46, 47]. These are easily incorporated in our model to handle nonuniform multiconductor transmission lines with nonlinear terminations. This combination is even efficient when the lines are lossless or have a low loss, a case where conventional methods based on voltage and current have difficulties. The examples given in the previous section firmly validate the accuracy of this method.

Chapter 5

Electromagnetic Fields In Metallic Enclosures Lined with Resistive Material

5.1 Introduction

The use of equipment enclosures to shield against emissions and external energy is a common practice. Efforts range from use of metal impregnated plastics to thick steel panels incorporating waveguide design in air vents. The choice of complexity depends on system performance and application. The question has often been raised as to whether high field intensities within such enclosures will affect equipment reliability. Clearly this is increasingly pertinent in cases of heavy shielding where resonator-like structures with high quality factors (Q) result. Moreover, in these cases, any energy leakage may be highly frequency selective with substantial associated field strength.

The primary motivation for studying such structures is that computers are now operating at faster speeds and consuming more power, resulting in significantly increased levels of power at higher frequencies. Also typical metallic enclosure configu-

rations have dimensions which are electrically resonant at frequencies in the hundreds of megahertz range.

This study focuses on the use of resistive material within the enclosure walls for absorbing some of the contained RF energy, thereby avoiding high Q enclosures and reducing the likelihood of significant field buildup within enclosure. The energy leakage from perforations (holes, slots) on the walls is also being studied. The radiation properties of these structures are examined by varying the size and position of the holes in the enclosure. Some guidelines on the usage of resistive material and perforations to reduce radiation from metallic enclosures are obtained.

In analyzing this problem the two dimensional finite-difference time-domain (FD–TD) technique as described in Section 5.2 is used. The enclosure is modeled as four perfectly conducting plates forming a rectangular box with apertures. The inside is lined with resistive material which is modeled as a layer of dielectric material with finite conductivity. A simplified model of the enclosure configuration is shown in Figure 5.1. Numerical results are presented in Section 5.3

Modeling the metallic walls as perfectly conducting will result in an infinite Q for enclosures with neither aperture nor resistive lining. In order to accurately model the electromagnetic fields in such enclosures, the finite conductivity of the walls has to be considered. There have been several attempts to model thin conducting sheets in FD–TD that are limited to low frequencies [62, 65]. In these models the fields are assumed to be constant within the conducting sheet, whereas at high frequencies they vary significantly. An efficient implementation of highly conducting thin sheets for a wide frequency band in FD–TD is presented in Section 5.4.

5.2 Method of Solution

The finite-difference time-domain (FD–TD) technique [55] is used in the analysis. It is based on the discretization of the electric and magnetic fields over rectangular grids together with the finite difference approximation of the spatial and temporal derivatives appearing in the differential form of Maxwell's equations. The reasons for which the FD–TD methodology was selected include the relative ease of treating complicated geometries with dielectrics, the requirement of only simple arithmetic operations in the solution process, and the flexibility for time- and frequency-domain analyses.

In the FD–TD technique, a computational domain is first defined and divided into rectangular cells. Electric and magnetic fields are spatially discretized in a staggered manner [12]. Electric fields are assigned to integer (n) time steps and magnetic fields are assigned to half-integer ($n + 1/2$) time steps for the temporal discretization of fields. Next, the spatial and temporal derivatives of the two Maxwell's curl equations are approximated using center differences. Maxwell's curl equations for a homogeneous, isotropic, time- and frequency-invariant medium are:

$$\nabla \times \overline{H} = \epsilon_r \epsilon_0 \frac{\partial \overline{E}}{\partial t} + \sigma \overline{E} \tag{5.1}$$

$$\nabla \times \overline{E} = -\mu_r \mu_0 \frac{\partial \overline{H}}{\partial t} \tag{5.2}$$

where ϵ_0 is the free-space permittivity, 8.854×10^{-12} F/m and μ_0 is the free-space permeability, $4\pi \times 10^{-7}$ H/m. ϵ_r and μ_r are the dielectric constant and relative

permeability of the medium and σ is the electric conductivity. Maxwell's divergence equations are ignored since the curl equations with appropriate boundary conditions uniquely determine the solution. In rectilinear coordinates, the curl equations can be rewritten as a set of six scalar equations. For two-dimensional problems, which are assumed to be uniform and infinite in one direction, these equations decouple into the H-field and E-field polarizations. For example, the three equations governing the H-field polarization assuming y is the uniform direction are as follows,

$$\mu_r \mu_0 \frac{\partial H_y}{\partial t} = \frac{\partial E_z}{\partial x} - \frac{\partial E_x}{\partial z} \tag{5.3}$$

$$\epsilon_r \epsilon_0 \frac{\partial E_x}{\partial t} = -\frac{\partial H_y}{\partial z} - \sigma E_x \tag{5.4}$$

$$\epsilon_r \epsilon_0 \frac{\partial E_z}{\partial t} = \frac{\partial H_y}{\partial x} - \sigma E_z \tag{5.5}$$

Difference equations are derived from these equations by applying center differencing. This ensures that the spatial and temporal discretizations are of second-order accuracy, where errors are proportional to the square of the cell size and time increment [12]. The electric field terms involving conductivity are approximated by using the average of the field values at a half time step before and after the desired time.

$$H_{y\ i,k}^{n+1/2} = H_{y\ i,k}^{n-1/2} + \frac{\Delta t}{\mu_r \mu_0} \left(\frac{E_{z\ i+1,k}^{n} - E_{z\ i,k}^{n}}{\Delta x} - \frac{E_{x\ i,k+1}^{n} - E_{x\ i,k}^{n}}{\Delta z} \right) \tag{5.6}$$

$$E_{x\ i,k}^{n+1} = C_e E_{x\ i,k}^{n} - C_h \left(\frac{H_{y\ i,k}^{n+1/2} - H_{y\ i,k-1}^{n+1/2}}{\Delta z} \right) \tag{5.7}$$

$$E_{z\ i,k}^{n+1} = C_e E_{z\ i,k}^{n} + C_h \left(\frac{H_{y\ i,k}^{n+1/2} - H_{y\ i-1,k}^{n+1/2}}{\Delta x} \right) \tag{5.8}$$

where

$$C_e = \frac{1 - \sigma \Delta t / 2\epsilon_r \epsilon_0}{1 + \sigma \Delta t / 2\epsilon_r \epsilon_0} \qquad C_h = \frac{\Delta t / \epsilon_r \epsilon_0}{1 + \sigma \Delta t / 2\epsilon_r \epsilon_0} \tag{5.9}$$

Finally, with appropriate initial and boundary conditions, the solutions to the difference equations are obtained through explicit leapfrog time marching. This corresponds to alternating the advance of electric and magnetic fields (i.e., first the electric fields are calculated, then the magnetic fields are calculated, and the sequence is repeated). To achieve accurate results, the cell sizes are taken to be a fraction, typically 1/20, of the smallest wavelength. The maximum time increment and the cell size are related by the stability criterion [56],

$$\Delta t \leq \frac{1}{c\sqrt{(1/\Delta x)^2 + (1/\Delta z)^2}} \tag{5.10}$$

where c is the speed of light in free space. Fields are set to be zero initially everywhere to satisfy the causality condition consistent with zero excitation for time less than zero. The boundary conditions are continuity of tangential electric and magnetic fields on material interfaces, vanishing tangential electric fields on perfect conductors, and absorbing boundary conditions on the outer boundary of the computational domain. Second-order absorbing boundary conditions [57] are used to limit the computational domain by simulating unbounded space.

The implementation of the excitation source requires that certain electric and

magnetic fields be updated at each time step. These steps are essentially repeated until steady state is reached for a sinusoidal excitation, or until all the transient fields have propagated out of the computational domain for a Gaussian pulse excitation. To obtain multi-frequency data, the time waveforms of the sources are chosen to be Gaussian pulses, i.e., $\simeq \exp[-((t-t_0)/T)^2]$, where t_0 is the delay, and T determines the pulse-width. Some limitations to the range of frequencies that can be analyzed are that the grid must be fine enough to adequately model the frequency of interest and that the Gaussian pulse must contain a significant amount of energy at that frequency.

In order to obtain certain frequency domain parameters, such as the radiated power or the radiation pattern, the complex field amplitudes on a closed surface must be obtained. The post-processing of full time domain information for the purpose of generating frequency domain data is expensive in storage and is inefficient. The complex field amplitudes are instead calculated at selected multiple frequencies. Complex amplitudes at each frequency are calculated simultaneously on a boundary enclosing the scatterer using the discrete Fourier transform. Once the complex field amplitudes have been stored, the far-field radiation pattern can be calculated using Huygens' principle [16]. Normalization of the complex field amplitudes at a particular frequency is performed by dividing the complex Fourier amplitudes of the fields by the Fourier amplitude of the excitation.

5.3 Numerical Results and Discussion

FD–TD numerical results have been obtained for several metallic enclosures lined with resistive materials and perforations on the walls. A few of these cases are demonstrated in this section. We have studied the effects of having different size perforations on the side and top plate of the enclosure. We have also observed the variations in radiated power and resonant frequencies with placing resistive materials at different locations within the enclosure.

The size of the computational domain used to perform these calculations is 200 by 200 nodes. The cell size is 0.004 m in both dimensions. The size of the computational domain is therefore 0.8 meters by 0.8 meters. The enclosure is a perfectly conducting box of width 0.408 m and height 0.092 m. The time step used is 7.8 ps.

The excitation source is a magnetic line current source with a Gaussian pulse amplitude that is placed within the enclosure. The pulse width is 190 ps and is defined to be equal to two standard deviations of the Gaussian pulse. To simulate the magnetic line current source, we excited a magnetic source $M = M_0/(\Delta x \Delta z)$ in the discretized Maxwell's electric field curl equation. The value of the Gaussian pulse is imposed on M_0. The magnetic field at time $n + 1/2$ at node i, k, where the source is located, is updated as

$$H_{y\ i,k}^{n+1/2} = H_{y\ i,k}^{n-1/2} + \frac{\Delta t}{\mu_r \mu_0 \Delta x}\left(E_{z\ i+1,k}^{n} - E_{z\ i,k}^{n}\right) - \frac{\Delta t}{\mu_r \mu_0 \Delta z}\left(E_{x\ i,k+1}^{n} - E_{x\ i,k}^{n}\right) - \frac{\Delta t}{\mu_r \mu_0 \Delta x \Delta z} M_{0\ i,k}^{n} \qquad (5.11)$$

To verify the excitation scheme, the FD–TD prediction was compared with the closed-form solution of two simple cases. First the radiation of the magnetic line current source in free space was obtained, which exhibits a linear increase with frequency. The second case was the radiation of the source in a parallel plate with separation 0.092m, which is constant over the frequency range of up to 3 GHz. In this range of frequency only the TEM mode will be propagating in the parallel plate waveguide, and has a radiated power of -21.4 dBW/m. Since the source is halfway between the two plates, the next propagating mode is TM_2 with cutoff frequency of 3.26 GHz. The results of the FD–TD prediction and the closed-form solution for magnetic line source in free space and inside a parallel plate are shown in Figure 5.2.

The variation in the radiated power as a function of frequency from the enclosure is illustrated in the following four cases. The first case shows the effect of aperture size on radiation. The second and third cases exhibit the variation in radiated power with position of the resistive material and aperture. The fourth case demonstrates the effect of source position inside the enclosure.

The first case shown in Figure 5.4 illustrates the effect of aperture size on the side plate. There is no resistive material used in this case. The solid curve represents the radiation from an enclosure with aperture size of 1.2 cm. The dashed curve corresponds to the radiation from the same enclosure with aperture size of 2.4 cm. The corresponding configuration is shown in Figure 5.3. the peak radiation at resonant frequencies decreases with increase in aperture size, resulting in a lower quality factor. Since the source is placed at the center of the enclosure, mainly the even modes at approximately 0.8, 1.6 and 2.4 GHz are being excited. The lowest resonant frequency

observed around 200 MHz is due to the quasi-static resonance at the aperture. As shown in the next cases the characteristics of this resonance is not altered by placing resistive material within the enclosure.

The second case, shown in Figure 5.6, is a metallic enclosure with an aperture on the side plate. The resistive material is placed at different locations within the enclosure to demonstrate the effect of its position on the radiated power. The dimensions of the configurations are given in Figure 5.5. The resistive material used has a relative dielectric constant of 2, conductivity of 1 mho/m and thickness of 1.6 cm. The curves in Figure 5.6 correspond to four different positions of the material. The solid curve illustrates the case where the material is on the side plate. The other three curves have resistive material on the top plate near the corner (T1), 10 cm from the corner (T2), and at the center (T3). Overall the lowest radiated power is obtained when the resistive material is placed on the sides, since the resonances shown in this figure are due to the longer dimension of the enclosure.

Figure 5.7 illustrates the case where the metallic enclosure has resistive material on the side plate and aperture at different positions. The resistive material used have the same properties as the previous cases. Figure 5.8 compares the power radiated of four different configurations. The solid curve illustrates the case where aperture is on the side. The other three curves have the aperture near the corner (T1), 10 cm from the corner (T2), and at the center (T3). Overall radiated power is smallest when the aperture is placed on the top plate of the enclosure. The optimum position of the aperture depends on the resonant mode and its corresponding field pattern. For example the resonance at 0.8 GHz has the least amount of radiation when the

aperture is at position T2, where the transverse field is minimum.

The fourth case demonstrates the effect of source position in the enclosure. The configuration and the source locations considered are shown in Figure 5.9. Both the aperture and the resistive material are on the side plate. The curves in Figure 5.10 show the radiated power versus frequency for three different locations of the source. The solid curve shows the radiated power when the excitation is located at the center. The odd mode resonances are not excited then and hence the radiation at those resonant frequencies is minimal. However, in the other two curves where the source is off-center, there is significant amount of radiation at odd mode resonant frequencies.

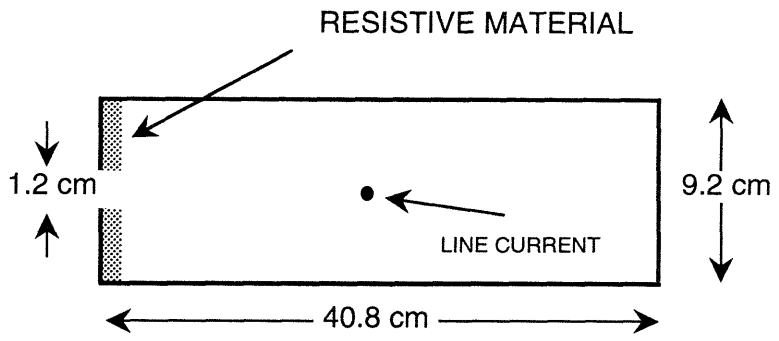

Figure 5.1: Simplified 2-D configuration.

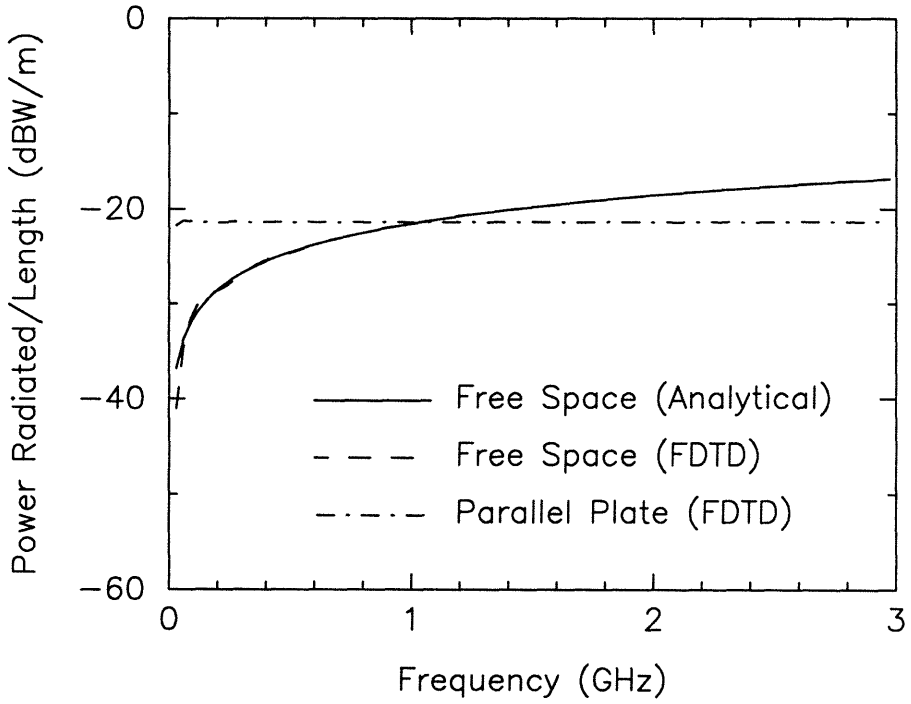

Figure 5.2: Radiated power from a line current source in free space and inside a parallel plate.

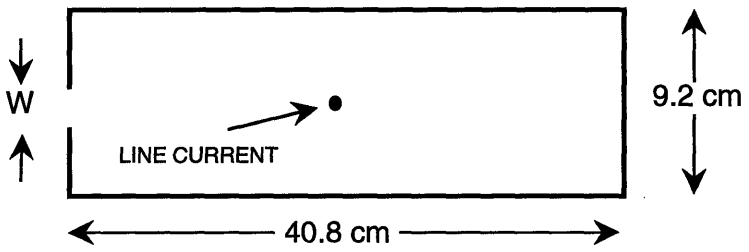

Figure 5.3: Configuration of the enclosure with different aperture size on the side.

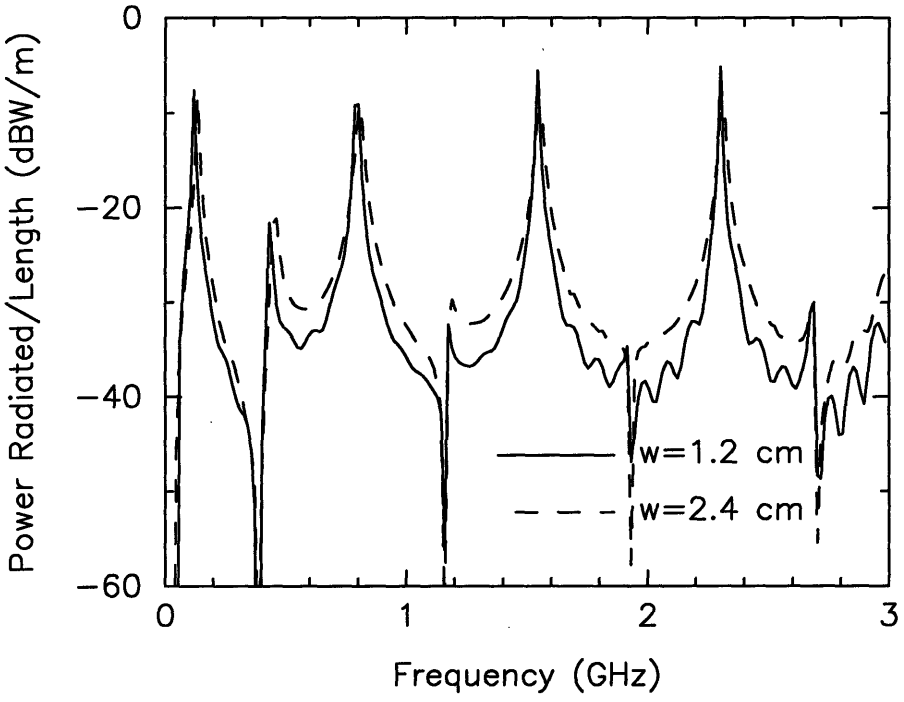

Figure 5.4: Radiated power from the enclosure with different aperture size on the side.

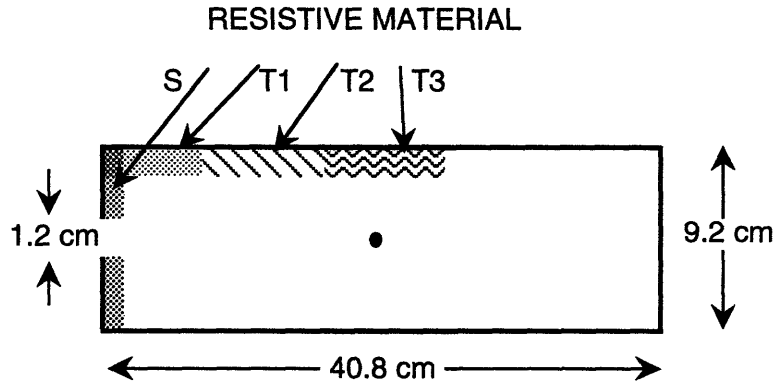

Figure 5.5: Configuration of the enclosure with aperture on the side and resistive material at different positions.

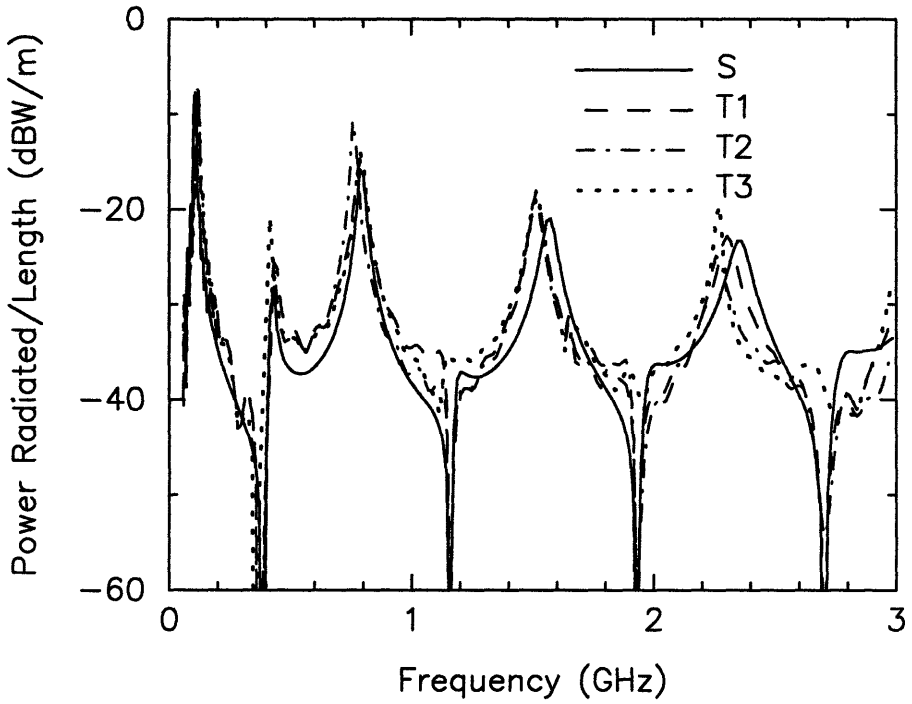

Figure 5.6: Radiated power from the enclosure with aperture on the side and resistive material at different positions.

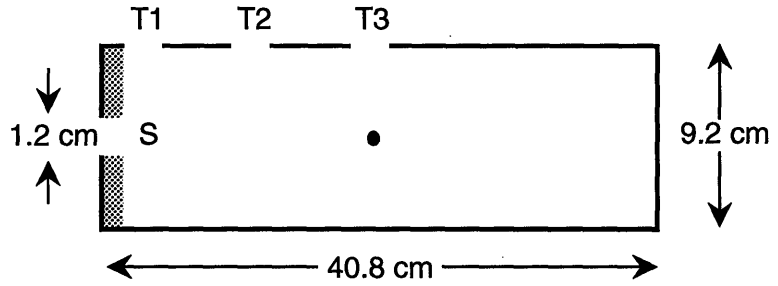

Figure 5.7: Configuration of the enclosure with resistive material on the side and aperture at different positions.

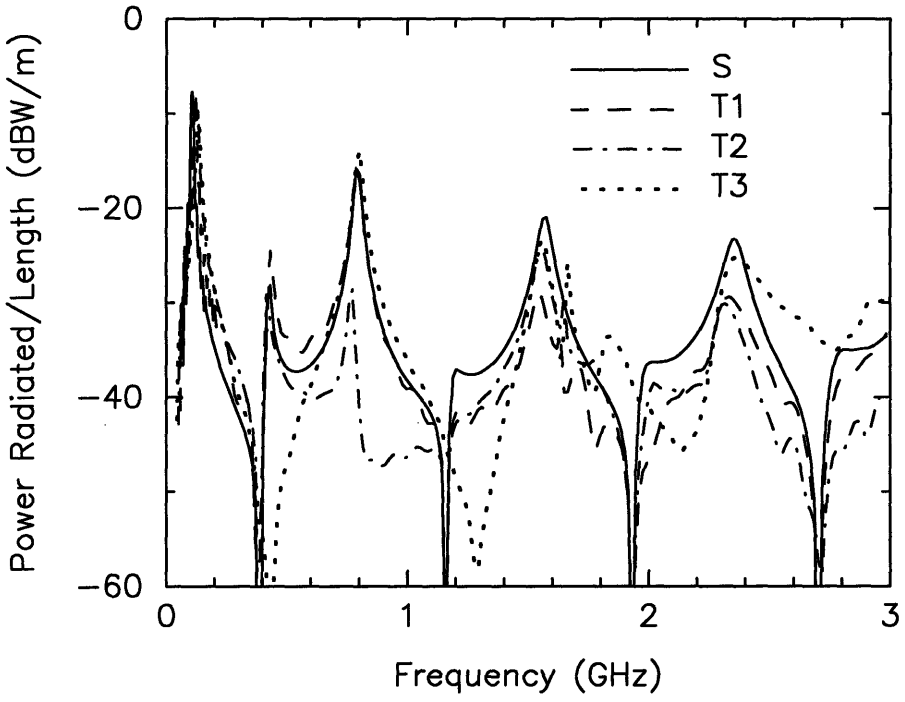

Figure 5.8: Radiated power from the enclosure with resistive material on the side and aperture at different positions.

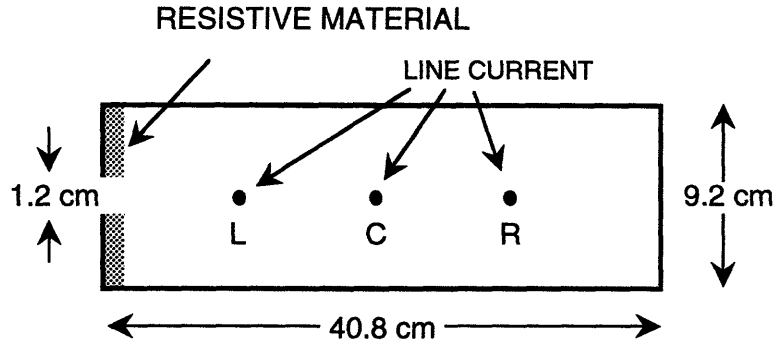

Figure 5.9: Configuration of the enclosure with the source positioned at the center, or off-center.

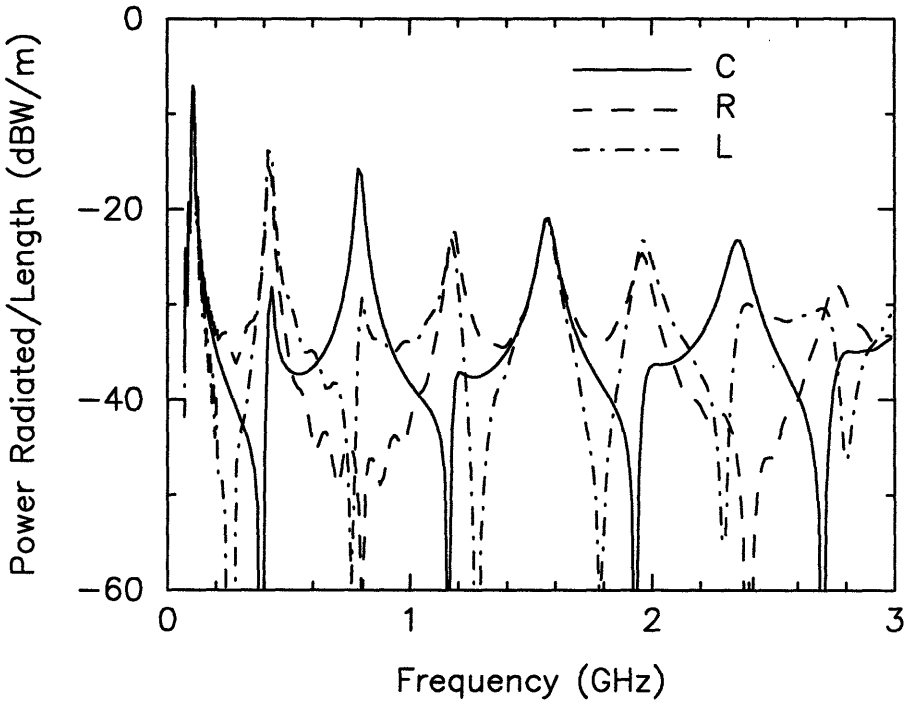

Figure 5.10: Radiated power from the enclosure with excitation source at different locations within the enclosure.

5.4 Modeling Conducting Sheets in the FD–TD Method

Accurate modeling of the electromagnetic fields in metallic enclosures in FD–TD requires the consideration of the finite conductivity of the metallic walls. Recently several different methods have been proposed for efficiently modeling electrically thin material sheets in FD–TD method [65]-[62]. All these methods, when applied to a conductor, assume a thickness which is small compared to skin depth at all frequencies of interest. The electromagnetic fields are then approximately uniform over the cross section of the sheet. However, for material with a high conductivity these fields vary significantly within a very small thickness of the material. Therefore, the frequency dependence of the fields has to be considered.

A dispersive surface impedance boundary condition is employed in [61] to replace a conducting half-space in FD–TD. Applying this approach to finite thickness material is only valid at high frequencies were the thickness is several skin depths. The surface impedance of a highly conducting half-space goes to zero as frequency approaches zero. However, for a conductor with finite thickness it approaches the resistive sheet impedance value.

In this section a formulation which is valid for a wide frequency band from very low frequencies up to where the thickness exceeds several skin depths is described. A frequency dependent surface input impedance concept for highly conducting thin sheets is used. The impedance is written in Laplace domain and then expanded as an infinite product. The time domain expression is obtained in terms of poles and

residues. Finally, the FD–TD implementation is derived via a recursive approach to efficiently calculate the fields at the conductor.

An impedance boundary condition relates the tangential components of the electric and magnetic fields via an impedance factor Z. In frequency domain at the interface this is

$$\overline{E}_{\tan}(\omega) = Z(\omega)[\hat{n} \times \overline{H}_{\tan}(\omega)] \tag{5.12}$$

where $\overline{E}_{\tan}$ and $\overline{H}_{\tan}$ are tangential electric and magnetic fields and $\hat{n}$ is the outward unit normal vector to the interface. Fields are assumed to have $e^{j\omega t}$ time dependence.

For a conducting material with permittivity ϵ and conductivity σ, the complex permittivity in frequency domain can be written as

$$\epsilon_c = \epsilon - j\frac{\sigma}{\omega} \tag{5.13}$$

where ω is the angular frequency. If the material is a good conductor ($\omega \ll \frac{\sigma}{\epsilon}$), then ϵ_c can be approximated as

$$\epsilon_c \approx -j\frac{\sigma}{\omega}. \tag{5.14}$$

For highly conducting sheets the electromagnetic wave within the conductor propagates normal to the interface. Therefore the surface impedance is analogous to a transmission line of thickness ℓ and intrinsic impedance η_c as the conductors wave impedance for all incidence angles. The input impedance of the transmission line of

length ℓ terminated with an impedance η_t is

$$Z_{in} = \eta_c \frac{\eta_t + \eta_c \tanh(jk_c\ell)}{\eta_c + \eta_t \tanh(jk_c\ell)}. \tag{5.15}$$

When free space is the medium on the other side of the interface ($\eta_t = \eta_0$), the second term in the numerator and the first term in the denominator become small compared to the other terms and can be ignored. The input impedance is then approximately

$$Z_{in} \approx \eta_c \coth(jk_c\ell). \tag{5.16}$$

The wave impedance and wavenumber for a material with complex permittivity ϵ_c are

$$\eta_c = \sqrt{\frac{\mu_0}{\epsilon_c}} \tag{5.17}$$

$$k_c = \omega\sqrt{\mu_0\epsilon_c} \tag{5.18}$$

Using (5.14), (5.17) and (5.18) the input impedance (5.16) expressed in terms of the Laplace transform variable $s = j\omega$ is

$$Z_{in}(s) = \alpha\sqrt{s}\, \coth(\alpha\sigma\ell\sqrt{s}) \tag{5.19}$$

where $\alpha = \sqrt{\mu_0/\sigma}$. Using power series expansion of hyperbolic sine and cosine in [11]

this becomes

$$Z_{in}(s) = \frac{1}{\sigma\ell} \frac{\prod_{m=1}^{\infty} \left[1 + \left(\frac{2\alpha}{(2m-1)\pi}\right)^2 s\right]}{\prod_{m=1}^{\infty} \left[1 + \left(\frac{\alpha}{m\pi}\right)^2 s\right]}. \tag{5.20}$$

It is worth noting that (5.20) satisfies the low frequency limit of the thin conducting sheet $1/\sigma\ell$.

A frequency domain expression such as (5.12) is not suitable for implementation in FD–TD. However, the use of inverse Laplace transform allows (5.12) to be written in the time domain

$$\overline{E}_{\tan}(t) = \int_0^t Z(\tau)[\hat{n} \times \overline{H}_{\tan}(t-\tau)]d\tau \tag{5.21}$$

An approximate time domain surface impedance $Z(t)$ can be obtained after truncating the numerator and denominator of (5.20) and calculating the poles and the corresponding residues. Keeping Q terms of the denominator and $Q-1$ terms in the numerator, the inverse Laplace transform of (5.20) can be written as

$$Z(t) = \sum_{m=1}^{Q} C_m e^{A_m t} \tag{5.22}$$

where A_m is the mth pole and C_m is the residue at the corresponding pole.

The discretization of (5.21) as a convolution sum at the Nth time step is

$$\overline{E}_{\tan}(N) = \sum_{k=0}^{N-1} \sum_{m=1}^{Q} F_m(k)[\hat{n} \times \overline{H}_{\tan}(N-k)]. \tag{5.23}$$

The function F_m is part of the mth term of the time domain surface impedance (5.22), and is obtained by discretizing the convolution integral (5.21). Assuming that $\hat{n} \times \overline{H}_{\tan}(t)$ is piecewise constant within the time interval Δt, $F_m(N)$ can be written as

$$F_m(N) = \int_N^{N+1} C_m e^{A_m \Delta t \gamma} \Delta t d\gamma = \frac{C_m}{A_m} \left(e^{A_m \Delta t} - 1 \right) e^{A_m N \Delta t}. \tag{5.24}$$

The computational cost for evaluating the convolution sum of (5.23) is quite large and it increases as N becomes large. It also requires the storage of all the previous tangential magnetic fields at the conductor interface. However, since $F_m(N)$ is in exponential form the summation can be performed recursively with low computational cost and storage. The sum in (5.23) is

$$\overline{E}_{\tan}(N) = \sum_{m=1}^{Q} \overline{G}_m(N) \tag{5.25}$$

where

$$\overline{G}_m(N) = F_m(0)[\hat{n} \times \overline{H}_{\tan}(N)] + e^{A_m \Delta t} \overline{G}_m(N-1). \tag{5.26}$$

The efficiency of this approach is evident when (5.25) and (5.26) are compared to the convolution sum. The storage requirements here are 2Q variables for the poles and residues, and Q variables per grid on the conductor interface. Also the computation and storage requirements remain constant as N becomes large.

To obtain a more accurate expression for the discretized convolution integral,

the tangential magnetic field $\hat{n} \times \overline{H}_{\tan}(t)$ is assumed to be piecewise linear within Δt. The linear assumption gives the following form instead of (5.24)

$$F_m(N) = \int_{\phi}^{N+1} (1 - |\gamma - N|)\, C_m e^{A_m \Delta t \gamma} \Delta t d\gamma \tag{5.27}$$

where the lower limit of the integral ϕ is

$$\phi = \begin{cases} 0 & N = 0 \\ N - 1 & N \geq 1 \end{cases} \tag{5.28}$$

Evaluating the above integral yields,

$$F_m(N) = \begin{cases} \dfrac{C_m}{A_m^2 \Delta t} \left(e^{A_m \Delta t} - 1 - A_m \Delta t \right) & N = 0 \\ \dfrac{C_m}{A_m^2 \Delta t} \left(e^{A_m \Delta t} - 1 \right)^2 e^{A_m \Delta t (N-1)} & N \geq 1 \end{cases} \tag{5.29}$$

In analogy to (5.25) the electric field at the interface is obtained recursively as

$$\overline{E}_{\tan}(N) = \sum_{m=1}^{Q} F_m(0)[\hat{n} \times \overline{H}_{\tan}(N)] + \overline{G}_m(N-1) \tag{5.30}$$

where

$$\overline{G}_m(N-1) = F_m(1)[\hat{n} \times \overline{H}_{\tan}(N-1)] + e^{A_m \Delta t} \overline{G}_m(N-2). \tag{5.31}$$

The linear assumption requires the storage of the tangential magnetic field at one previous time step in addition to the variables required in piecewise constant case.

A difficulty in incorporating the impedance boundary condition into FD–TD is that the formulation requires both tangential electric and magnetic fields to be at the

same location in space and time. Most widely used FD–TD methods are based on the interleaved grid in space and time. For this work, the tangential electric field at the boundary was updated by using the magnetic field at half a grid in front of the boundary. However, the shift in time is taken care of by using the average electric field. For example (5.25) can be written as

$$\overline{E}_{\tan}(N+1) = -\overline{E}_{\tan}(N) + 2\sum_{m=1}^{Q} \overline{G}_m(N+1/2). \tag{5.32}$$

To verify the time domain surface impedance boundary condition formulation in FD–TD, results for the one dimensional case are compared with the exact analytical solution. In all the cases a copper sheet with a thickness of 35 μm and a conductivity of 5.8×10^7 is used. A time step of $\Delta t = \Delta x/2c$ was chosen, and a Gaussian pulse with pulse width of $20\Delta t$ was launched. The reflected wave is recorded and transformed into frequency domain. The reflection coefficient, R, the ratio of the reflected to the incident wave, is calculated. In the following cases the transmissivity $(1 - |R|^2)$, is plotted versus frequency.

In Figure 5.11 the FD–TD curve was obtained by updating the electric field at the interface with (5.25), using $\Delta x = 4$ cm and Q=20 terms of the expansion. There is an excellent agreement up to 600 MHz, compared to the exact solution shown in solid line. To obtain higher frequency results, Δx was decreased to 4 mm and the results are shown in Figure 5.12 with dashed line. To obtain a better approximation of the fields at higher frequencies, 40 terms of the expansion are used with other parameters unchanged. The results were plotted in Figure 5.13.

In order to assess the behavior of the 40 term approximation at higher frequencies, the Δx was reduced to 0.4 mm. In Figure 5.14 the piecewise linear assumption of the tangential magnetic fields is used in the computation. The piecewise linear assumption yields a more stable and accurate result at higher frequencies than the piecewise constant case. The agreement of FD–TD and the exact solutions decreases with increase in frequency. The transmissivity is within 2 dB of the exact solution at frequencies of up to 30 GHz, where the thickness is about 90 skin depths. To obtain more accurate results at higher frequencies more terms in the expansion need to be considered. The disagreement at low frequencies is due to the truncation of the time response and can be improved by running the simulation for a longer period of time. It is worth noting that in obtaining these results the time step is scaled with the grid size while the same number of time steps is used.

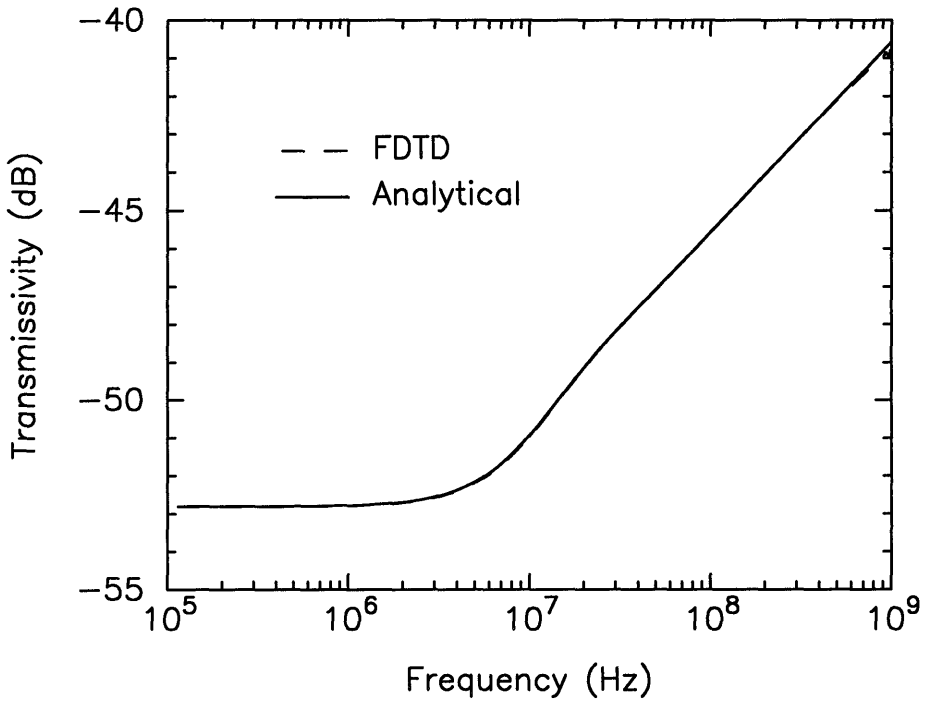

Figure 5.11: Transmissivity of a plane wave incident upon a 35 μm copper sheet with $\Delta x = 4$ cm, $Q = 20$ and piecewise constant magnetic field.

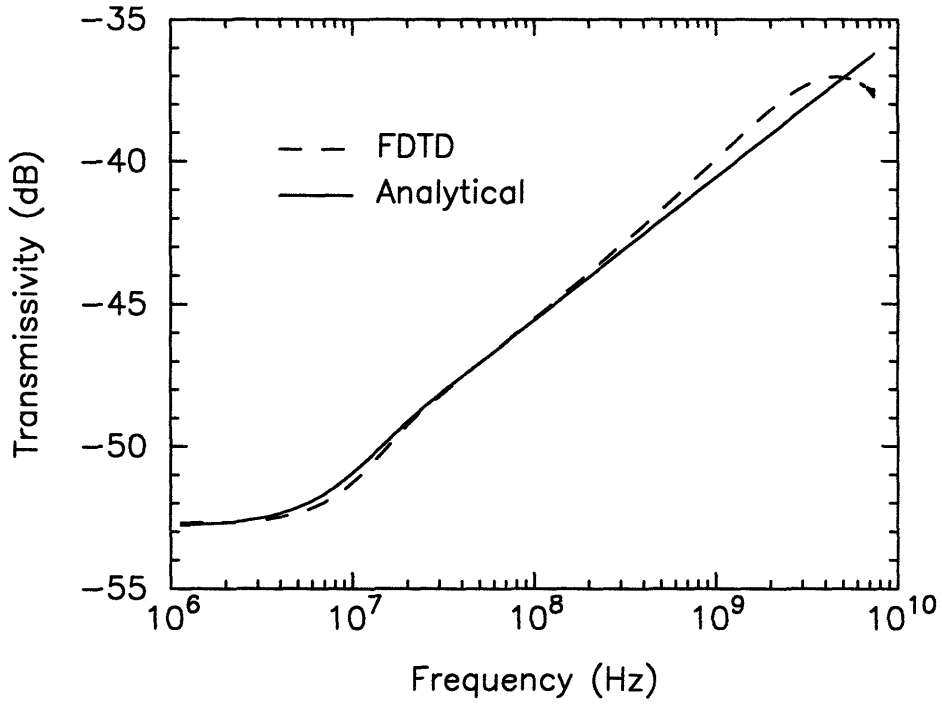

Figure 5.12: Transmissivity of a plane wave incident upon a 35 μm copper sheet with Δx = 4 mm, $Q = 20$ and piecewise constant magnetic field.

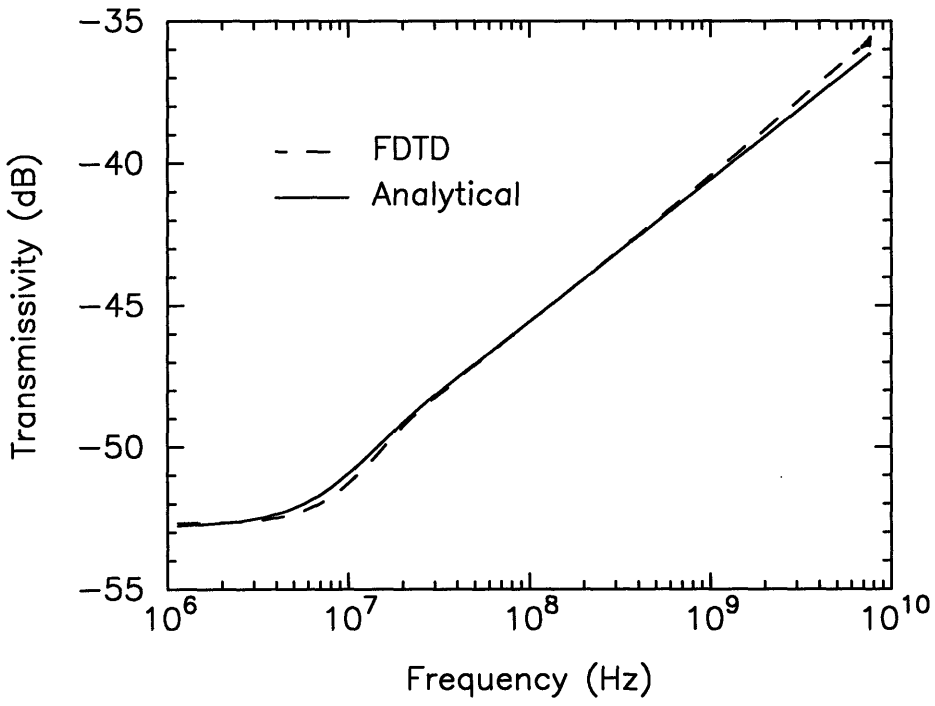

Figure 5.13: Transmissivity of a plane wave incident upon a 35 μm copper sheet with $\Delta x = 4$ mm, $Q = 40$ and piecewise constant magnetic field.

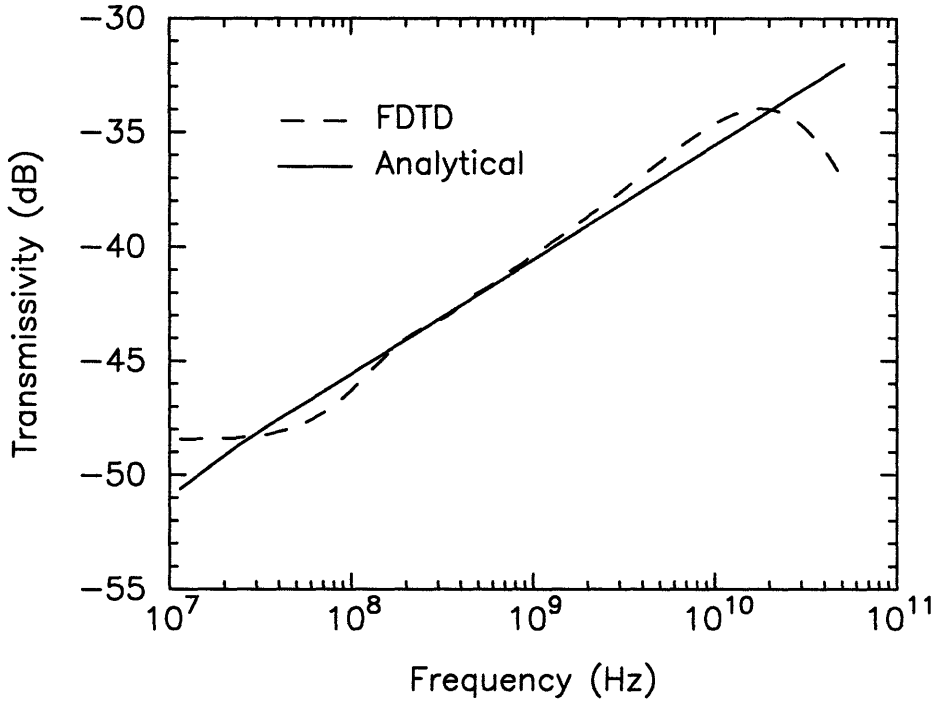

Figure 5.14: Transmissivity of a plane wave incident upon a 35 μm copper sheet with $\Delta x = 0.4$ mm, $Q = 40$ and piecewise linear magnetic field.

5.5 Conclusions

The radiation properties of metallic enclosures have been studied with a two dimensional FD–TD method. The walls of the enclosure were lined with absorbing material to reduce the fields inside and the contained RF energy, thereby avoiding high Q resonances. The energy leakage from perforations (holes, slots) on the walls is also studied. The radiation properties of these structures were examined by varying the size and position of the holes in the enclosure.

Rectangular enclosures were studied to simulate computer packages. Resonances observed at frequencies of interest were due to modes created in the longer dimension of the enclosure. The lowest power radiated at resonant frequencies, for the configurations studied, is obtained for the case where the conductive material is placed on the side walls and perforations on the top plate. The optimum position of the perforation depends on the resonant mode and its corresponding field pattern. Also, increase in aperture width results in lowering the Q of the structure. The position of the source is the determining factor on the modes excited in the enclosure. For example odd modes are not excited with the excitation located at the center of the enclosure.

A time domain surface impedance boundary condition for highly conducting sheets in FD–TD was formulated. An efficient implementation based on the recursive properties of convolution with exponentials was presented. The reflected fields were simulated and exhibit good agreement with the exact solutions. This model of the conducting sheet is valid for a wide frequency band from very low frequencies up to where the thickness is several skin depths.

Chapter 6

Interference Analysis in Airborne Instrument Landing System Receivers

6.1 Introduction

Instrument Landing System (ILS) for airport runway was developed during World War II and was standardized by the end of the war. It is a low-approach guidance system to aid the pilot in landing the aircraft when the weather is bad and visibility is poor. ILS is currently being used worldwide as the standard precision approach guidance system. It consists of three basic components: a localizer to line the airplane up with the runway azimuthally, a glide slope for vertical glide path control, and marker beacons for homing and position determination. To improve the range accuracy, DME (Distance Measurement Equipment) is often used as a replacement for the marker beacons in newer ILS. The localizer transmitter is installed approximately 1000 feet from the end of the runway. The glide slope transmitter is located on a line perpendicular to the runway centerline at the point where airplanes touch

down.

The ILS localizer operates in the band 108.00 to 112.00 MHz using only those frequencies where the digit in the tenths-of-a-megahertz position is odd. Prior to the late 1970s, there were 20 channels allocated for localizers at 100 kHz spacing (108.1 MHz, 108.3 MHz, etc.). However, with the rapid increase of air traffic, 20 ILS localizer channels were unable to meet the demand. To solve this problem, the separation between localizer channels was reduced from 100 kHz to 50 kHz. Although the number of channels allocated for localizers was thus increased to 40 (108.1 MHz, 108.15 MHz, 108.3 MHz, 108.35 MHz, etc.), not all new channel frequencies are assigned because some older localizer receivers designed in accordance with the Radio Technical Commission for Aeronautics Report RTCA DO-131 [78] (100 kHz channel spacing) are still in use today and may not operate properly in an environment in which the separation between localizer channels is 50 kHz. Studies and actual assignment efforts have indicated that there is a potential frequency congestion problem.

The objective of this research is to develop a computer simulation tool for ILS to: perform quantitative analyses of in-band (aviation band) and out-of-band electromagnetic interferences, and make quantitative assessments of electromagnetic interferences within the ILS service volume, and predict channel capacities of ILS in congested metropolitan areas. Based upon these requirements, we established a methodology for implementing the simulation software from theoretical studies of electromagnetic interference phenomena, as shown in Figure 6.1.

In brief, we first locate potential interference sources and use an electromagnetic propagation model to compute the desired and interfering signal strengths. Then

an interference analysis based upon safety standards, which are consistent with the receiver model, is performed. Finally, the interference analysis results for various locations are combined to make a channel capacity assessment.

Accordingly, the following steps were identified and accomplished during this interference study,

- identification of potential interfering radiation sources, including in-band and out-of-band sources,
- development of propagation models to be used to calculate the interference levels,
- development of receiver models to determine the quantitative effect of interference signals,
- verification and validation of models through testing and checking against existing data, and
- implementation of the models in a graphical user interface which allows for interactive retrieval of quantitative information on the assessment,
- design of an optimum channel assignment procedure for multiple runways in a given area.

In section 2 of this chapter, the technical approach taken for this study is described. It contains descriptions on the models used in the simulation tool. Section 3 is centered around the simulation procedures in the software, Electromagnetic Simulation Applied to Landing Systems (EMSALS).

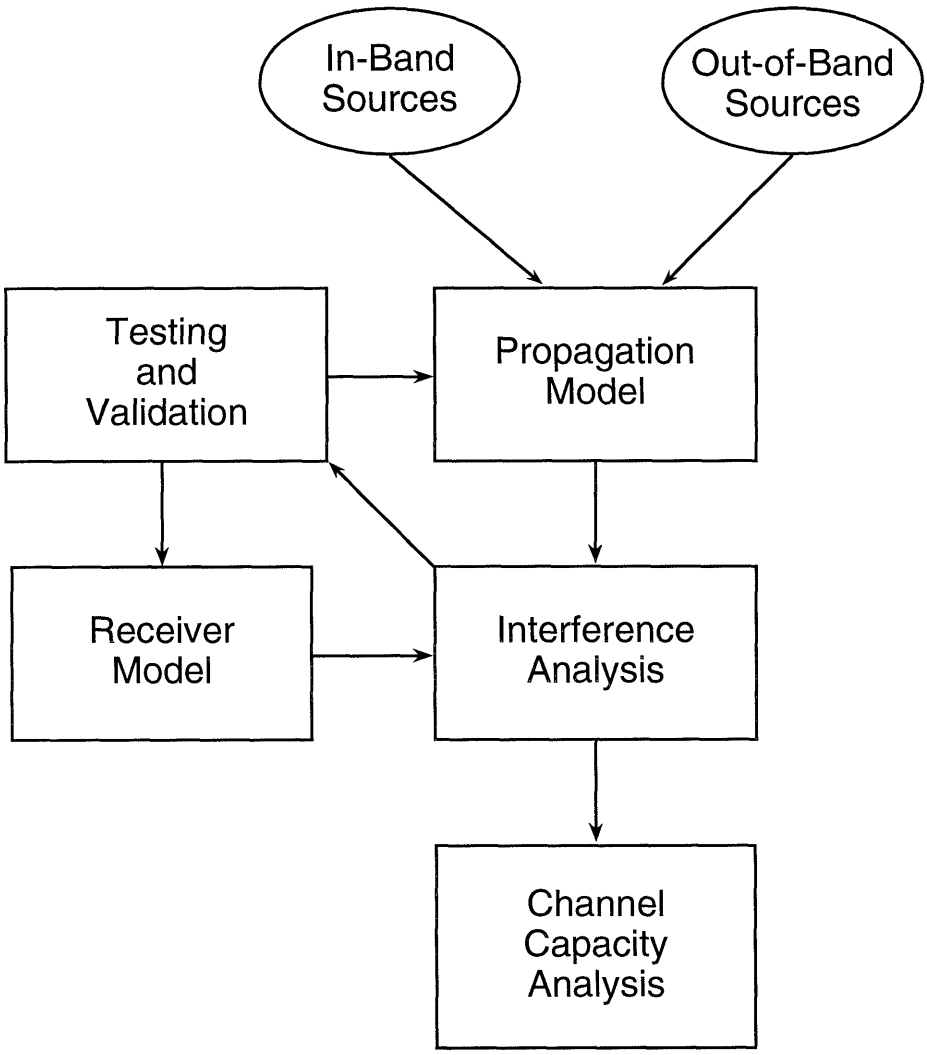

Figure 6.1: Overview of methodology.

6.2 Technical Approach

6.2.1 Identification of Interference Sources

The first issue encountered in frequency management is identification of the potential sources of electromagnetic interference. In order to carry this out systematically, interference sources are classified according to the mechanisms by which they come into the radio spectrum. The interference generated by radio-navigational transmitters is classified as in-band, and interference from all other sources will be called out-of-band.

According to the existing FAA requirement, a fully functional ILS consists of localizer, glide slope, and DME. Each of them operates in a frequency band far from the others. Localizer operates in the 108–112 MHz band; glide slope operates in the 329–335 MHz band; and DME operates between 962 and 1215 MHz (Figure 6.2). They are not assigned independently at any given runway. Rather, the transmitting frequencies are uniquely assigned by the channel plan in which the channel number is the sole parameter. Therefore, interference analyses have to be separately conducted in the respective frequency bands, and linked together by channel plan [68]. If any of the three components are unable to meet the interference immunity requirements, the channel cannot be assigned.

Of the three components of an ILS, the localizer band has the most serious interference problems. Besides other localizers, existing VHF Omni-Range (VOR) transmitters could also be interferers (see Figure 6.2). Conversely, potential interference from a new localizer to existing localizers or VORs has to be considered as well. Commercial FM broadcasting stations equipped with powerful transmitters can also

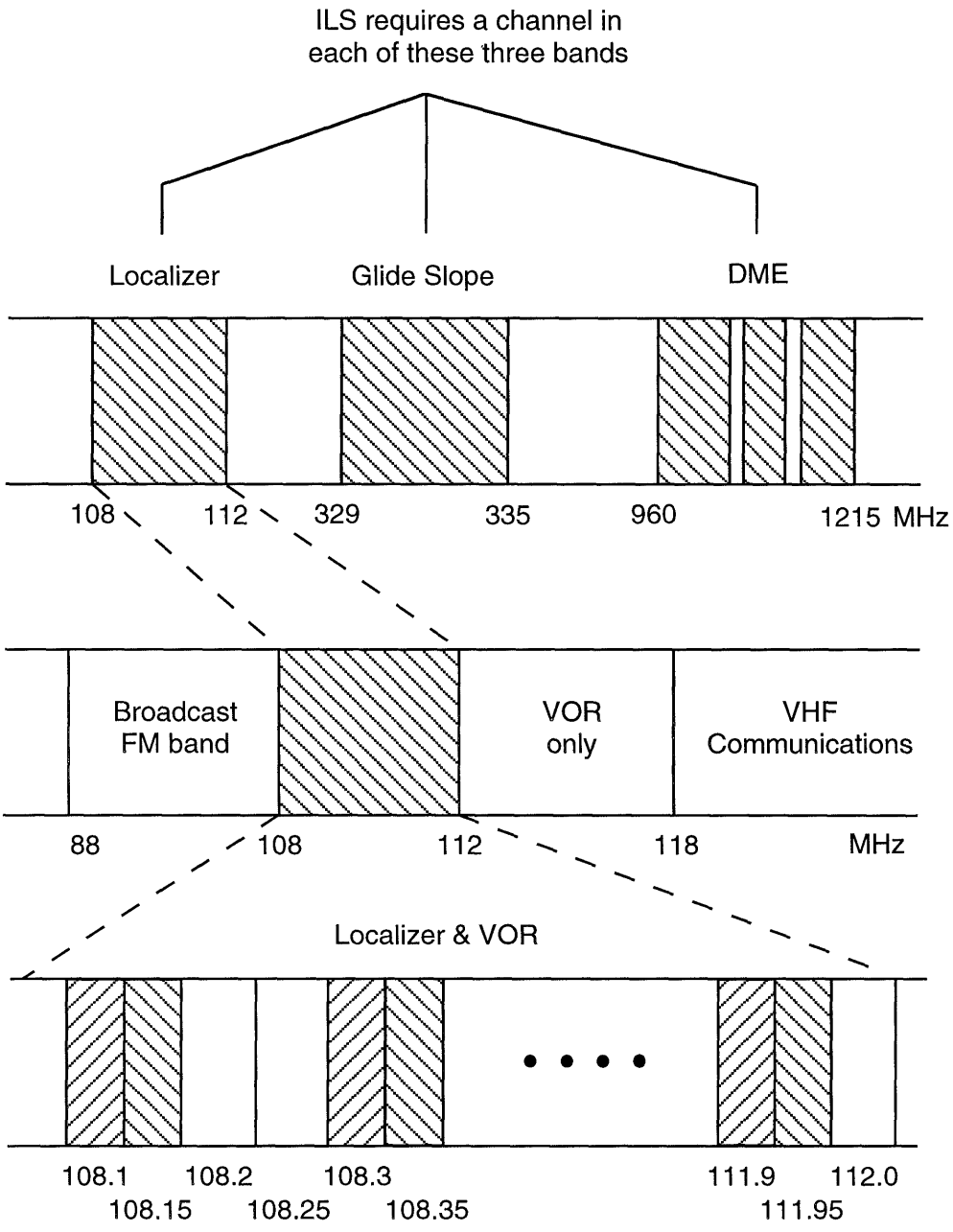

Figure 6.2: ILS channel components frequencies.

easily generate out-of-band interferences. Our analysis scheme is thus centered around localizers. We consider the interferences to and from other localizers and VORs to be direct interferences, whereas interferences occurring at the accompanying glide slope and DME frequencies are indirect interferences.

Interferer Databases

Based upon the above chosen interferer classes, computer simulation of interference analysis can be performed systematically. The first task involves preparation of interferer databases. National Telecommunications and Information Administration (NTIA) maintains a complete computer database of all government radiowave transmitters called the Government Master File (GMF). The FAA section contains approximately 35 megabytes of data. For ILS frequency management purposes, we extract only three portions, corresponding to the localizer, glide slope, and DME frequency bands respectively. Because electromagnetic interference from ground-based transmitters is limited to geographically adjacent areas, we can extract a partial database to carry out regional analysis. Important pieces of information used by the simulation program are as follows: operating frequency, location (latitude, longitude), antenna height and elevation, authorized transmission power, antenna type, antenna orientation, and service volume radius.

For the purpose of out-of-band interference, we use the Federal Communications Commission (FCC) FM station database. This database contains an updated list of all licensed FM stations. This information is used in the simulation program to determine the strength of FM interference signals. The FM station database includes:

operating frequency, location (latitude, longitude), antenna elevation and authorized transmission power.

6.2.2 Propagation Model

A means of calculating the signal strength at a given point in space is needed for the interference studies. This is accomplished with the propagation model which is used to compare the relative strengths of desired and undesired signals (interference) at a point in space by evaluating the power loss incurred on them.

Four important mechanisms are involved in the propagation of the electromagnetic wave over spherical earth. They are:

- Beam spreading (free space loss): This loss is caused by the decrease in power density with increasing separation between the transmitter and receiver. It is an inherent property of propagation and present even in the absence of any interfering objects.

- Reflection and scattering: In the presence of the earth, ground reflections and scattering from terrain features enter into the characterization of the propagation phenomenon. The dielectric constant and conductivity of the ground, and scattering objects are included in this factor.

- Diffraction: Diffraction is also an important terrain effect, especially for propagation beyond line-of-sight, the so-called "shadow region" in electromagnetics. Two situations typically cause diffraction: (1) the presence of large obstacles that block the direct transmission, such as a mountain top, and (2) the spherical

profile of the earth's surface.

- Atmospheric effects: Due to the inhomogeneous nature of the atmosphere, the waves will attenuate and refract. There might also be attenuation caused by rain, snow falls, dust particles, etc. Clearly, the atmospheric factor varies constantly and thus, can only be rigorously treated in a statistical sense.

Propagation models differ in complexity and accuracy in their description of these phenomena; of course there is a trade-off between accuracy and complexity. The first model used in EMSALS considers only free space loss. This very simplified model does not take into account the other mechanisms mentioned above (reflection, terrain and atmospheric factors). However simplified it may be, it does give a first approximation of the interference problem. When the range is small, and the antenna pattern directive enough to avoid ground reflections, it gives a relatively accurate description of the propagation loss. This model is kept as an "option" in the EMSALS program for its speed.

For rigorous ILS frequency management assessment, we use the IF-77 model which incorporates other propagation mechanisms. First developed through the joint effort of ITS and the FAA [70]–[71], this model combines propagation theory with observed data regarding radiowave propagation collected over the years. In order to cover all the complex factors involved (terrain surface reflections and divergence effects, tropospheric multipath, atmospheric absorption, rain attenuation, and spherical earth diffraction) the IF-77 model takes a statistical approach in computing propagation loss. Averages are taken over the changes in reflection properties of the surface, variations in the atmosphere, and short term phenomena such as rain. For a fixed

transmitter/receiver geometry, the propagation loss is distributed over a range of values, and can only be calculated in probabilistic terms. For example, one can derive that 95% of the time the loss will be below a certain value, or so-called 95 percentile in statistics.

From the view point of establishing safety margins, statistical modeling is actually more realistic than deterministic modeling because, propagation is so complicated that any perturbation in the environment will likely create errors in the so-called "exact" propagation loss prediction.

Due to its complexity, IF-77 takes considerably longer to run than the free space model. In the EMSALS program, a "look-up" method is developed to overcome this difficulty. For nominal antenna heights and patterns, propagation loss tables are generated for variations in range and transmitter height. These tables are stored and loss values are read from them; intermediate values of loss are obtained by interpolation. This scheme works quickly and without much loss of accuracy. Due to stringent constraints on computer memory, a nonlinear interpolation algorithm is used.

One minor concern regarding the IF-77 model is that it does not consider regional differences. The most obvious regional difference could be accounted for with the inclusion of a detailed terrain profile (high-resolution digital map) in the computation. For example, MIT Lincoln Laboratory developed the Spherical Earth with Knife-Edges (SEKE) model [87] which incorporates terrain profiles to perform propagation loss calculations. When the terrain profile is available, along with atmospheric factors, it is theoretically possible to calculate the "precise" propagation loss for a given path. In practice, it can only be carried out selectively, since it is very time-

consuming to incorporate the algorithm into every aspect of the EMSALS program. Moreover, the huge computer storage requirement and the availability of a complete United States digital map database is another area of concern.

IF-77 Model

The IF-77 propagation model can be used to calculate propagation losses at frequencies between 0.1 and 20 GHz. This range covers all the potential interference sources and the ILS operating frequencies. The input parameters and the associated ranges are as follows:

- Frequency: The operating frequency of the system, ranging from 0.1 to 20 GHz,
- Antenna height: The height of the transmitter antenna located at the ground system facility. It must be greater than 0.5 m above the facility site surface. The height of the facility site surface above mean sea level (MSL) should also be supplied to determine the antenna height above MSL.
- Cell height above MSL: The height at which the propagation loss is to be calculated. This height must be greater than the facility horizon height. The facility horizon height may be specified as input or, assumed to be the same as the height of the facility site surface, by default. "Cell" is the term adopted in EMSALS for a volume in space at which desired and undesired signal calculations are made.
- Distance: The distance between the transmitter antenna and the cell in question. This distance should be understood to be the great circle distance between

the two points.

- Antenna pattern: The vertical pattern of the transmitter antenna expressed in the form of a mathematical function. If not specified, the program assumes an isotropic pattern of radiation. An elevation pattern is used within the program since the magnitude of the ray that is reflected from the ground is modified by this pattern. Azimuthal pattern, on the other hand, is considered separately from the propagation model and comes into consideration externally, with the radiation power of the antenna.

- Polarization: This parameter can be specified as vertical, horizontal or circular and pertains to the transmitter antenna.

- Surface type options: These include mean terrain elevation, and the dielectric constant and conductivity of the reflecting surface. These parameters are used in the calculation of the reflection coefficients which partly determine the magnitude of the ray that is reflected from the ground. In EMSALS, parameters for average ground are assumed. In particular, the relative dielectric constant and the conductivity are taken as 15 and 0.005 (mho/m) respectively.

- Facility horizon location: The distance of the "horizon" from the transmitter and its height. This is a relatively simple way to take into account the effect of terrain. When such a specification is made, the obstacle is treated as a knife-edge and pertinent calculations are carried out. If not specified, the height of the horizon is taken to be the same as the height of the facility site elevation. Under this condition the only mechanism for diffraction will be that of the bulk of the earth.

Given these inputs, the program returns the propagation loss value at the "cell", that is the ratio of power radiated to the power that would be available at the receiving antenna located in the cell.

Conceptually, the IF-77 model is similar to the Longley-Rice model [73]. When propagation loss is calculated as a function of the distance between the transmitter and the receiver, three regions are considered. These are the line-of-sight (LOS) region, diffraction region, and scatter region.

The LOS region extends to the point where the cell becomes invisible. This may be due to the curvature of the earth, or the presence of an obstacle that blocks the radiation field. In either case, the field strength at the cell is assumed to be the sum of two rays, a direct ray from the transmitter and a reflected ray that bounces off the ground and reaches the cell. This is the geometrical optics approximation. To calculate the phase difference between the direct and the reflected rays, the location of the specular reflection point is determined from the solution of a third order equation [74]. Then, geometrical calculations are carried out to determine the relevant parameters.

In addition to the phase difference, the relative amplitude of the reflected ray is needed for the calculations. To evaluate this amplitude, an effective reflection coefficient is calculated. In this coefficient, Fresnel reflection coefficients, diffuse reflection attenuation, divergence and ray length factors [74], and the antenna pattern of the transmitter are taken into account. Fresnel reflection coefficients are determined using the dielectric constant and the conductivity of the reflecting surface. Diffuse reflection attenuation is determined using perturbation theory with the assumption

of small scale roughness. The divergence factor takes into account the curvature of the earth and consequent divergence of the rays. Finally, the amplitude of the reflected ray is modified by the magnitude of the antenna pattern in that direction.

In the diffraction region, there are two basic mechanisms of loss. The first is the so called knife-edge diffraction that becomes significant when there is an obstacle blocking the propagation path of the signal. The presence of a knife-edge is determined according to the specified facility horizon height. If there is a knife-edge present, the diffraction attenuation (or enhancement) is determined from the Fresnel theory for knife-edge diffraction. Ground reflections are taken into account in accordance with the Longley-Rice model.

The second important diffraction mechanism affecting EM wave propagation is that caused by the bulk of the earth, called spherical earth diffraction, or rounded earth diffraction. The calculations for this region are based on a curve fit approximation to the residual height gain function curves developed by Longley. In the diffraction region, diffraction attenuation is assumed to be linearly dependent on the distance. Knife-edge and round-earth diffraction considerations are combined to calculate the two points that determine the linear loss line.

Beyond the horizon, propagation is determined by two main propagation phenomena. The first one is round-earth diffraction, which has been discussed in the previous paragraph. The second mechanism is scattering due to the atmosphere. Scattering enhances the signal strength at over the horizon ranges. Scattering enhancement calculations are based on [75] but also include certain CCIR information [76].

In the frequency range of interest, electromagnetic wave propagation is also affected by: the lower, non-ionized atmosphere, absorption and attenuation caused by atmospheric phenomena, scattering due to rain (when the frequency is greater than 3 GHz), ionospheric scintillation, etc. Time and space variations of these factors lend themselves to a statistical description as employed in IF-77. Below is a description of how these factors are incorporated into the model.

Refraction is one of the most important effects the atmosphere has on EM wave refraction. It is caused by the non-zero refractivity gradient of the atmosphere. In such a medium, the rays bend as they propagate. One way to consider the effect of the bending is to use an effective earth radius that compensates for it. Over this "effective earth" the rays are assumed to propagate in straight lines, simplifying the calculations. However, when the antenna or cell heights in question are high, greater than 3 km, horizon distances become excessive and this method loses its accuracy. In such cases, effective antenna and cell heights are calculated using ray tracing through the atmosphere. In the ray tracing algorithm, refractivity is assumed to change exponentially with height. Absorption due to oxygen and water vapor is estimated by calculating the effective ray lengths contained within atmospheric layers of the appropriate thicknesses.

The "variability" of the signal is calculated based on the variations in the stochastic processes that affect signal propagation. These are considered under two main groups; atmospheric effects and surface effects. Each of these factors has an associated uncertainty that can be estimated by the variance of the stochastic process. These variances are combined to give a certain range of variation in the propagated

signal. The method of combining the variabilities follows the method used by Tary et. al. [77]. The range of values obtained can be interpreted as the change in signal strength from one particular time to another. For example, when we say 95% loss value, we mean that the loss value is not exceeded 95% of the time. In this scheme, it is reasonable to use different propagation values for desired and undesired stations to give a safety margin for the desired operation. More precisely, 95% value is used for the desired station and the 5% value is used for the undesired station so that the calculated D/U ratio at the cell will be valid at least 95% of the time.

6.2.3 Receiver Model

The purpose of establishing a receiver model is to evaluate the interference tolerance and to predict and analyze the receiver response to interference. Both in-band and out-of-band interference can cause receiver output guidance errors. The error in the course deviation resulting from the interference can be a serious problem especially during the critical approach and landing phase of an aircraft. The in-band interference is due to the emitters in the band between 108 MHz and 112 MHz which consist of localizers and VORs. The out-of-band interference of the localizer receivers is caused primarily by the high-power FM broadcasting stations which operate in the 88–108 MHz frequency band.

In order to understand how a localizer receiver operates and to see how interference affects the output of the receiver, experiments were conducted on two commercial receivers [67]. The components of a typical localizer receiver unit as shown in Figure 6.3 are: RF front end including filter and mixer, IF filter, envelope detector,

automatic gain control (AGC), 90 Hz filter, and 150 Hz filter. The function of the RF filter in the localizer receiver is to pass signals with carrier frequencies between 108 and 112 MHz. The purpose of the mixer is to shift frequencies of the input signals. Since the mixer is a non-linear device, it is where the FM intermodulation product is generated. The IF filter is used to select the desired signal and to reject adjacent interference sources. The function of the envelope detector is to extract the amplitude modulation envelope of the signal, and AGC is used to normalize the output.

In-band Interference

To understand the influences of various interferences on the output of localizer receivers, interference measurements were performed. In-band interference measurements include co-channel and adjacent-channel measurements. The test setup is shown in Figure 6.3. The input signal to the receiver is the combination of the localizer signal and interfering signals with carrier frequencies in the band between 108 MHz and 112 MHz. Minimum allowable signal to interference ratios (SIR), or minimum threshold for the desired localizer carrier power to the undesired interferer carrier power were measured.

FAA [68] and ICAO [72] have specified the minimum allowable signal to interference ratios, or minimum threshold for (D/U)-ratio, within certain airspace called Frequency Protected Service Volume (FPSV) of the localizer in order to provide an interference-free environment for the localizer. Taking into consideration the random fluctuations in signal strength, frequency and phase of the interferer, the predicted nominal SIR value must be above the minimum (shown in Table 6.1) more than 95

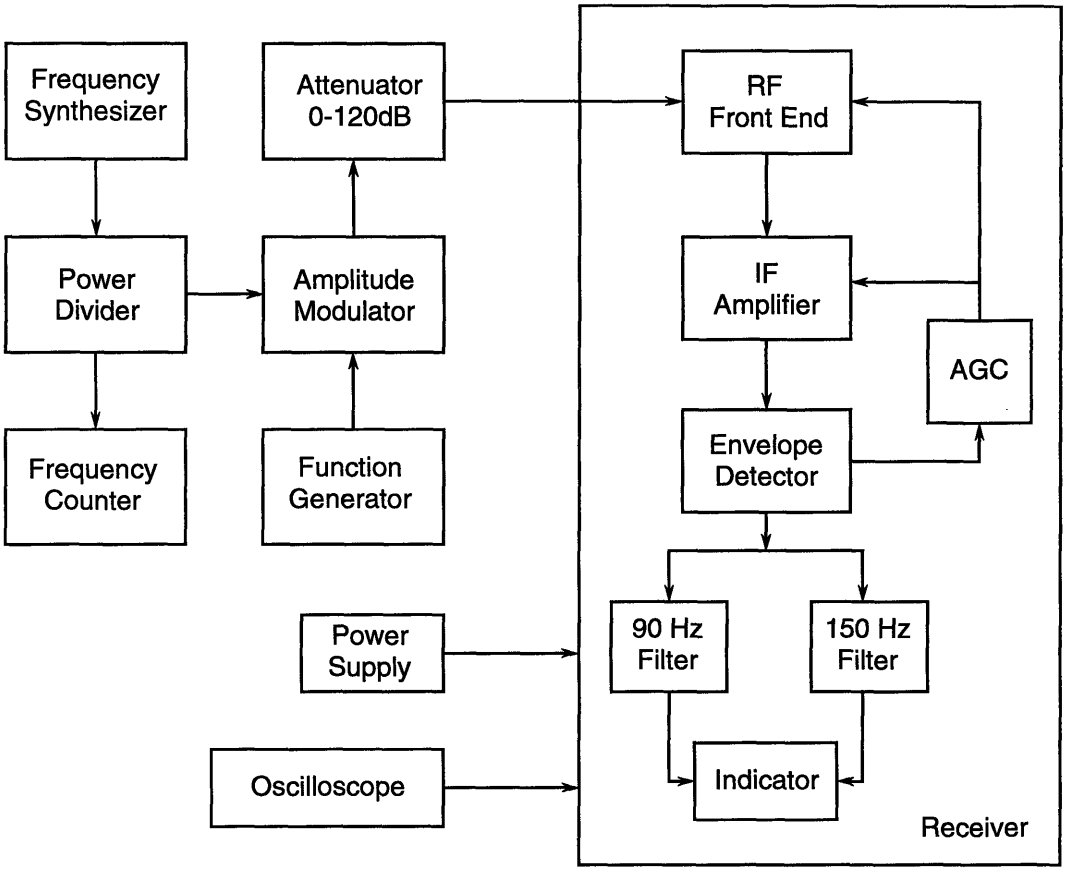

Figure 6.3: Reciever architecture and test setup.

Interferer (Localizer or VOR)	Minimum SIR (dB) ICAO	FAA
Co-Channel	+20	+23
1st Adjacent (Interim)	−7	−4
1st Adjacent (Final)	−34	−31
2nd Adjacent (±100 kHz)	−46	−43
3rd Adjacent (±150 kHz)	−50	−47

Table 6.1: Minimum SIRs required by FAA and ICAO.

percent of the time, SIR are the ratios of the desired localizer carrier power to the undesired interferer carrier power. The minimum SIR are established based on extensive measurements, taking into account the minimum requirements and including safety margins. The 3 dB extra safety margin in the FAA values is to account for the variance of ground station power output.

Depending on the frequency separating the desired localizer and interferer, different values for the specified minimum SIR are obtained. The desired signal must exceed the undesired co-channel signal, which is generated by the nearby localizers with the same frequency as the desired signal, by 23 dB or more. If the undesired signal has a frequency 50 kHz away from the desired signal (first adjacent channel), it can exceed the desired signal by up to 31 dB if the localizer receiver is designed in accordance with RTCA DO-131A/DO-195 or by up to only 4 dB if the localizer receiver is designed according to the RTCA DO-131. In addition to the localizers, VORs are potential adjacent channel interferers. The same adjacent channel protection criteria apply to the interference between Localizers and VORs. Table 6.1 also lists the minimum SIR for second adjacent channel and third adjacent channel cases.

Out-of-Band Interference

The out-of-band interference of the localizer receiver is caused primarily by the high-powered FM broadcasting stations which operate in the 88–108 MHz frequency band. The test setup for the out-of-band interference is similar to the test setup of the in-band interference (see Figure 6.3) except that the interference sources are FM signals instead of localizer or VOR signals. The out-of-band interference measurements include the FM intermodulation (B1) response and the FM desensitization (B2) measurements.

In order to quantify the susceptibility of ILS localizer receivers to various types of FM interference, several organizations have conducted experimental studies. These programs involved subjecting a selected set of commercially available localizer receivers to simulated and actual FM signal environments. Various types of interference error mechanisms have been investigated. In most cases, the experimental results were quantified in terms of the amount of FM signal power required to cause an unacceptable localizer error. The results of these studies are summarized in CCIR Report 929-1 [69]. This report forms the basis for the nonlinear receiver model used in EMSALS. The Airspace Model [82] which includes a set of refined FM immunity levels derived from recent bench tests by the FAA and Ohio University, is also incorporated in the simulation.

Type B1 interference has to do with receiver-generated intermodulation. High-powered FM broadcasting signals have the potential to drive ILS receivers into nonlinearity. As a result, several broadcasting signals with different carrier frequencies

interact within the receiver and generate frequency components at or near the ILS frequency, causing serious interference problems. Intermodulation products are generated with at least two FM signals and the signals must have a frequency relationship which can produce a single frequency in the frequency band between 108 MHz and 112 MHz after mixing. One of the broadcasting station must be powerful enough to drive the receiver into regions of nonlinearity but interference may then be produced even though the other signal(s) may be significantly less powerful.

For the intermodulation interference, the main consideration was the third-order intermodulation products for two signal and three signal cases. The intermod product frequency is either $(2f_1 - f_2)$ or $(f_1 + f_2 - f_3)$. For example, localizer reception on channel 109.1 MHz could be interfered with by the presence of FM broadcast station interference at 107.9 and 106.7 MHz (i.e., $2 \times 107.9 - 106.7 = 109.1$).

Type B1 interference is not considered to be a problem when the levels of the interfering signals at the receiver meet the following requirements:

$$2N_1 + N_2 - 2a(f_1) - a(f_2) < -120\,\text{dBm}$$

and

$$N_1 + N_2 + N_3 - a(f_1) - a(f_2) - a(f_3) < -126\,\text{dBm}$$

for two-signal and three-signal third order intermod, respectively, where f_1, f_2 and f_3 are the FM station frequencies in MHz and N_1, N_2 and N_3 are their respective signal

FM Broadcast Frequency, f_{FM} (MHz)	Maximum Level (dBm)
88–100	+10
88–106	$+10-(25/6)(f_{FM}-100)$
106–108	$-15-3(f_{FM}-106)$

Table 6.2: Type B2 interference threshold levels.

levels in dBm at the receiver input, and

$$a(f_i) = 20\log(\max[0.4; 108.1 - f_i]/0.4]) \qquad \text{for} \qquad i = 1, 2, 3.$$

The above criteria apply when the intermod frequency is the same as that of the localizer channel. When the intermod frequency is ±50, ±100 or ±150kHz away from the localizer frequency, an adjustment factor of 2, 8 or 16 dB is required. Each of the interfering signal levels (N_i) is reduced by this factor, if the adjacency criterion is met.

Type B2 interference occurs when the airborne receiver RF front-end is overloaded by one or more broadcasting signals. The RF section of a localizer receiver is especially vulnerable because the filter is designed to be wideband and its cut-off is not sharp below 108 MHz. This type of interference can happen when a strong FM station dominates the AGC signal and reduces the front-end receiver gain, or when the RF section of the receiver is overloaded by the FM station power. The susceptibility criteria for this type of interference is mainly a function of the frequency and power of the FM station. The criteria used in the receiver model is shown in Table 6.2.

6.3 Simulation Procedure

The simulation software (EMSALS) utilizes inputs such as the location and direction of the proposed runways and generates a graphical display of assessment results, showing which frequencies are available for new assignments. This assessment is performed by considering in-band and out-of-band interference sources. Within a large geographical area, a list of frequencies associated with each of the proposed sites can be obtained. Lastly, the number of runways that can be assigned with ILS channels is obtained by going through a number of different frequency assignment combinations.

Figure 6.4 illustrates the procedures involved in this program. Initially the required databases need to be selected, including local GMF and FM databases, as well as new candidate runway list. Then the whole sequence of DME analysis, localizer/glide slope analysis (keyhole analysis), and FM interference analysis is performed to obtain a list of possible frequencies for each of the new candidate runways. In the end, we have to go through the frequency combination process to conclude the channel capacity analysis. The order of performing DME, keyhole, and FM analyses are selected according to their complexity and computational requirements.

6.3.1 DME Analysis

The DME analysis, shown in Figure 6.5, utilizes the existing ILS and DME databases and the location of the new candidate runway as input. All possible channels are checked in order to determine if its use would interfere with existing DME facilities.

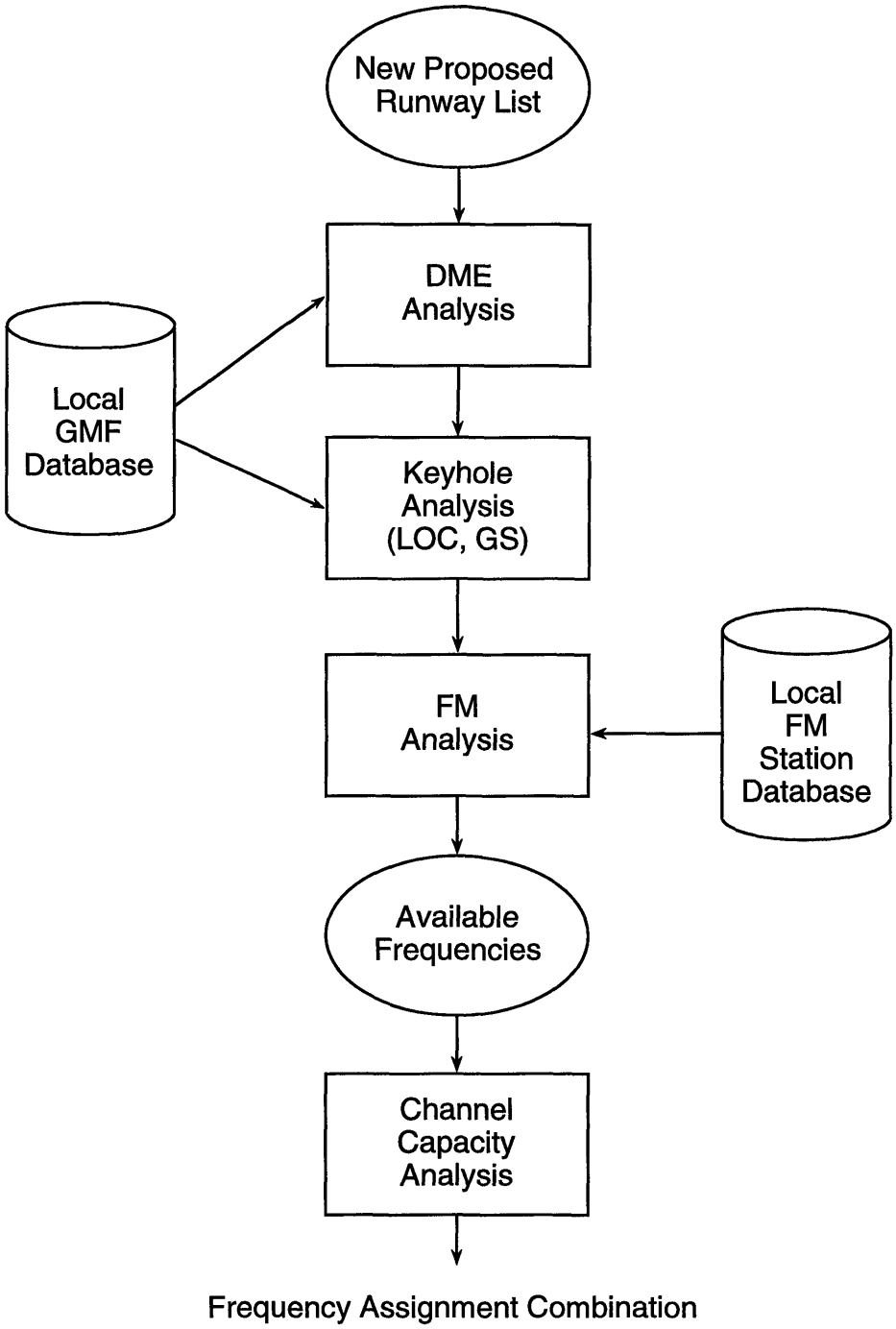

Figure 6.4: Simulation procedure used in the EMSALS software.

Co-channel interference is checked by searching the database for other users of that channel. The distance between any that are found and the new facility is then computed and compared to the FAA's separation criteria. If the separation criteria are met, the channel is then checked for first adjacent channel interference.

First adjacent interference is tested by calculating the strength of the desired and interferer signal at the edge of the frequency protected service volume (FPSV). The ratio is then compared against the DME receiver threshold for the type of interferer [68]. All channels are checked in this manner and those found to be free of interference are output for keyhole analysis. As indicated in FAA Order 6050.32, interference with channels separated beyond the first adjacent channel is not a problem.

6.3.2 Localizer and Glide Slope Keyhole Analysis

The localizer keyhole analysis procedure is shown in Figure 6.8. Those frequencies that have passed the DME analysis are now evaluated for interference from and interference to existing localizer, VOR and glide slope facilities. This analysis utilizes the localizer, VOR and glide slope database, in addition to the VOR expanded service volumes (ESV).

The location and orientation of the keyhole is established for the candidate runway. A standard keyhole, FPSV, is assumed for the candidate facility. The strength of the interferer and desired signals are computed at 8 points in the localizer's FPSV Figure 6.6. These include the 4 corners of the FPSV at the lowest and highest altitudes.

The classes high altitude, low altitude, and terminal VOR and VOR ESVs are

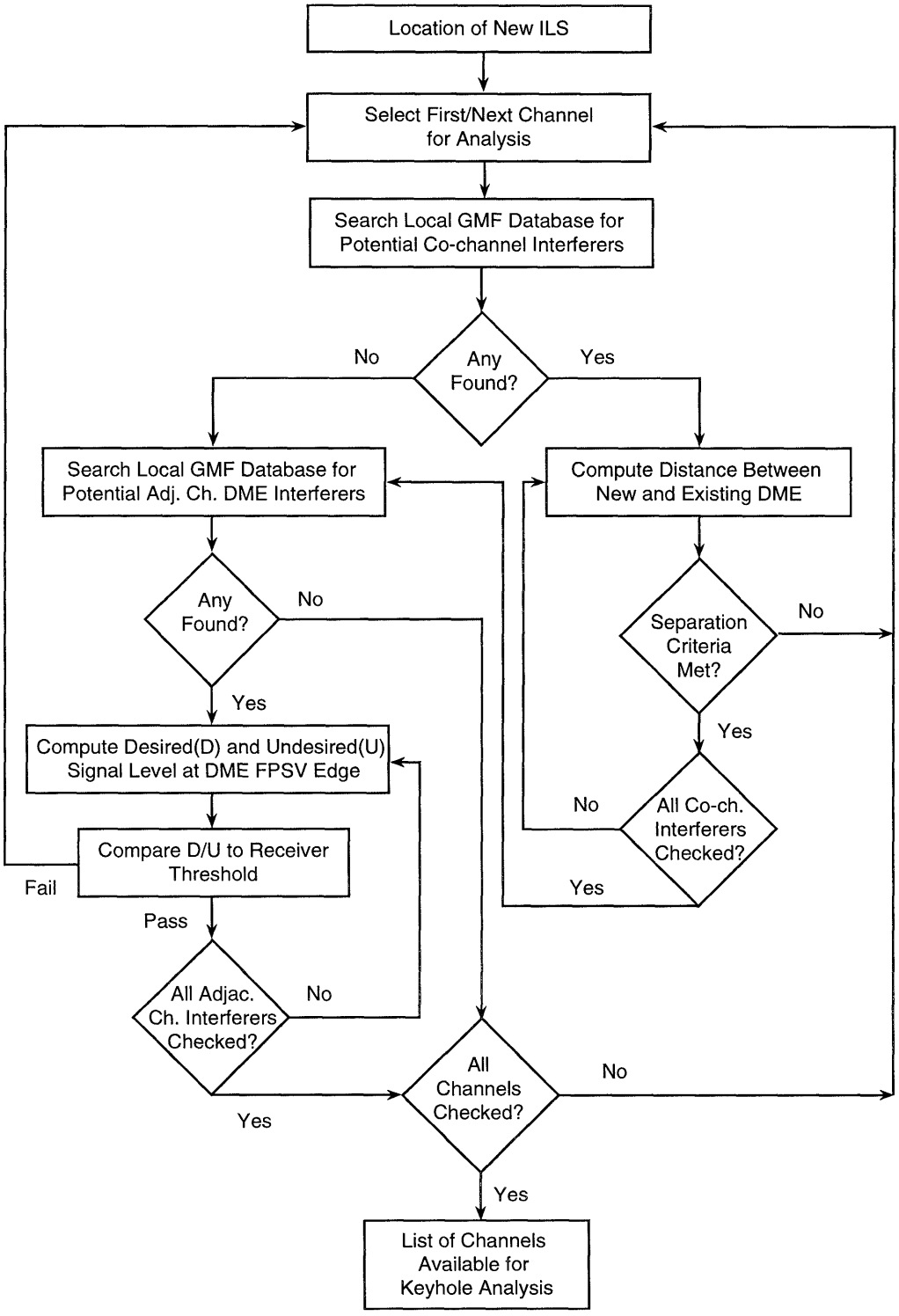

Figure 6.5: Flowchart of the DME analysis.

included in the analysis. The VOR antennas are assumed to have an omni-directional radiation pattern in azimuthal direction with an antenna gain of 2 dBi. The critical points in the VOR FPSV are shown in Figure 6.7. They are the closest point of the VOR FPSV to the proposed localizer emitter, two tangents to the VOR FPSV circle, and the intersection of the line in the boresight direction of the localizer antenna with the VOR FPSV circle. The critical point for the VOR ESVs is that which is furthest from the VOR (desired) facility and simultaneously closest to the localizer (undesired) facility. The signal strengths are computed at the lowest and highest altitudes of the critical points.

Any existing localizer/VOR facility within 125 nmi of the candidate facility is considered a potential interferer. The interferer radiated power at the critical point is determined by extracting the interfering localizer/VOR's location, orientation, transmit power and antenna type from the local GMF database. The distance and bearing to the critical point are computed. The antenna gain for that bearing is adjusted by the radiation pattern gain given for that antenna. The antenna patterns are given in FAA Order 6050.32.

The computed distance and the altitude of the critical point and the emitter are used by the chosen propagation model to calculate the loss in the transmitted signal. Having the distance, loss factor, power transmitted and the antenna gain a normalized signal strength can be calculated. The signal strengths for the desired and undesired facilities at the critical points are calculated and stored in a temporary spectrum file.

The first channel from the DME analysis is selected. The desired (D) to un-

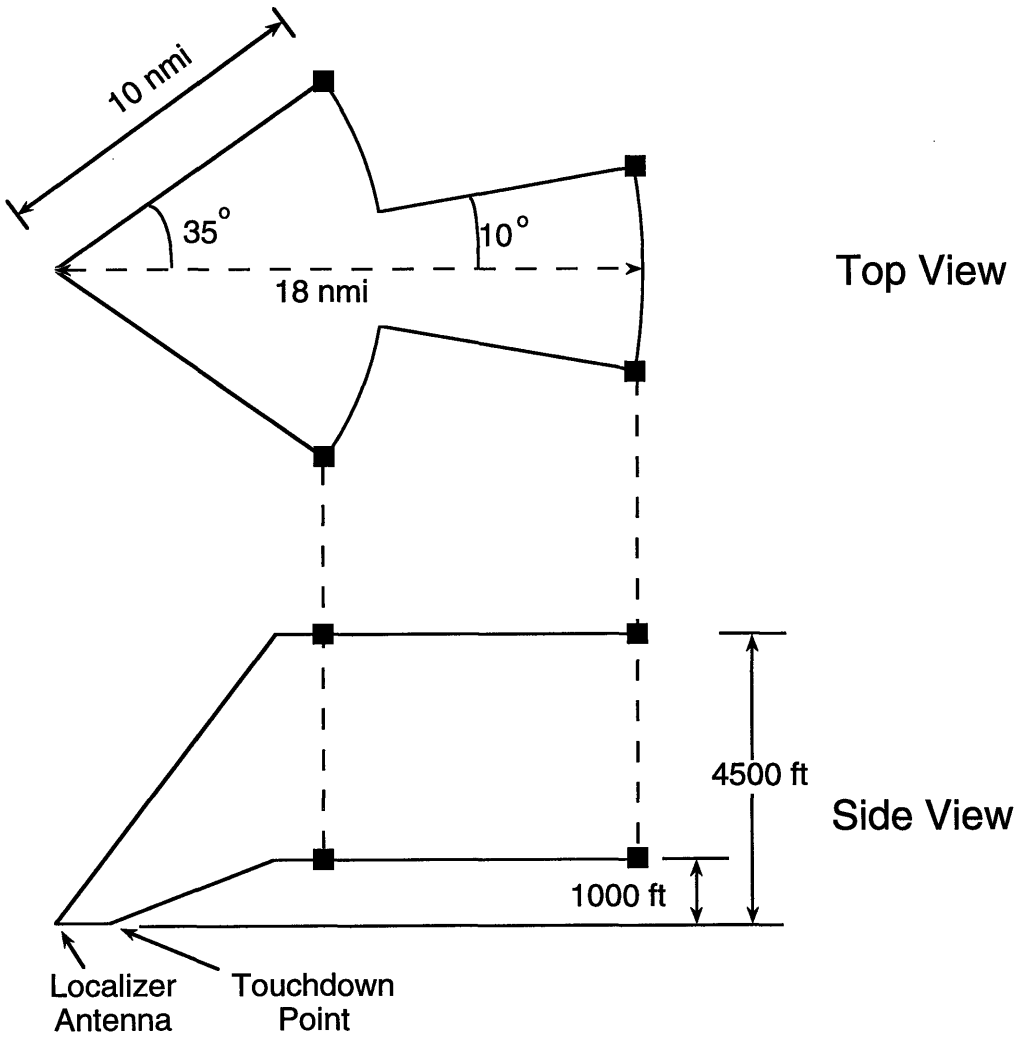

Figure 6.6: Candidate localizer critical points.

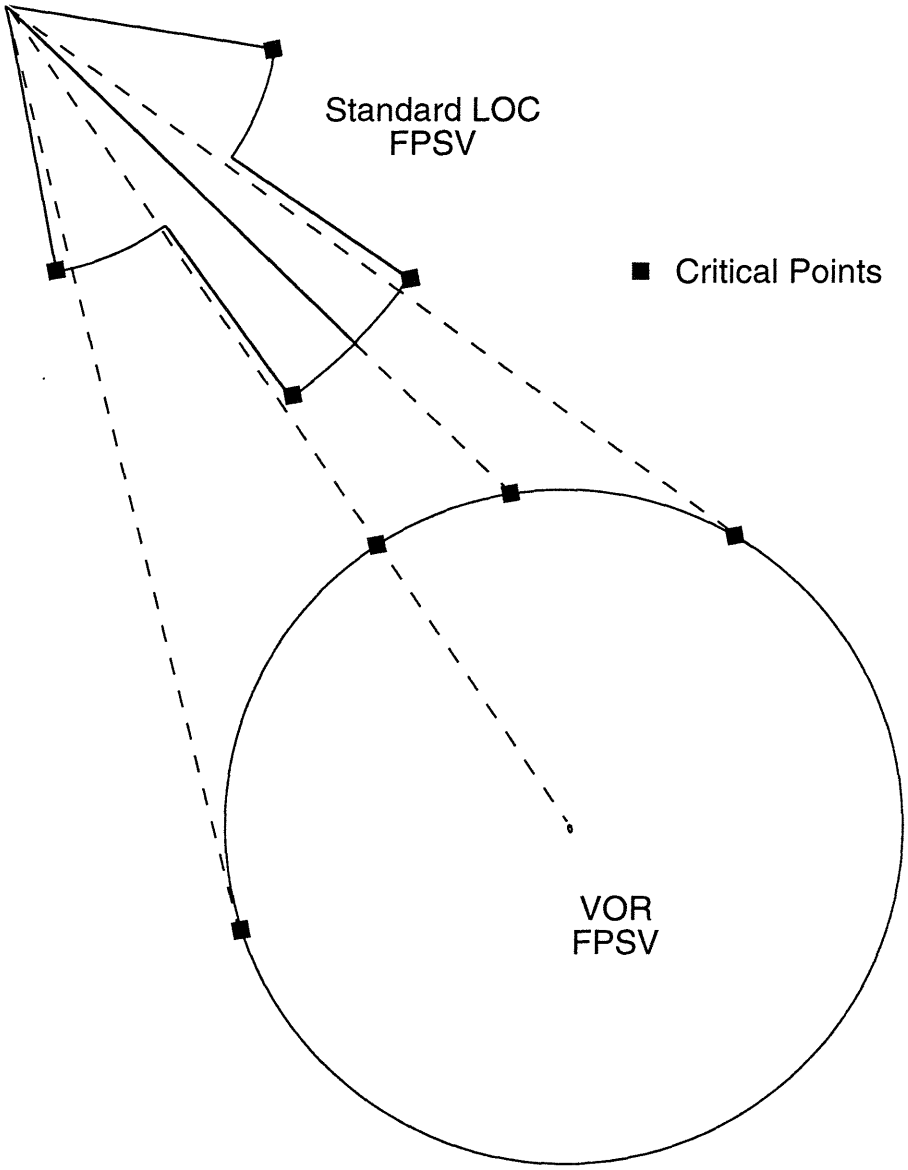

Figure 6.7: Localizer and VOR critical points.

desired (U) ratios are computed for co-channel and first, second and third adjacent channel interference for the selected channel. These are compared to the receiver D/U thresholds. The D/U calculation and comparison are repeated for all the critical points of the candidate and interferer FPSVs. The selected frequency is then analyzed for in-band glide slope interference.

Co-channel glide slope interference is not checked since the glide slope FPSV is well within the keyhole, and transmit powers, antenna gains and receiver thresholds are similar to those of localizer facilities. Adjacent channel glide slopes must be checked since the nature of the frequency pairing is such that widely spaced localizer channels can have adjacent glide slope channels. Those potential glide slope interferers that are within 10 nmi of the candidate facility are assumed to cause interference.

The keyhole analysis for the selected channel is completed after the glide slope analysis, and the next channel from the DME list can now be analyzed. The D/U computation and comparison process is repeated for all the channels that passed the DME analysis. The channels passed the keyhole analysis are now available for FM interference analysis.

6.3.3 FM Interference Analysis

Those frequencies that have passed the keyhole analysis are next evaluated for interference from FM broadcast band transmitters. The analysis as shown in Figure 6.9, utilizes the location, orientation and elevation of the candidate runway in addition to the FM database provided by FCC. Each FM station is characterized by location (latitude, longitude and altitude), station identity code, frequency and power.

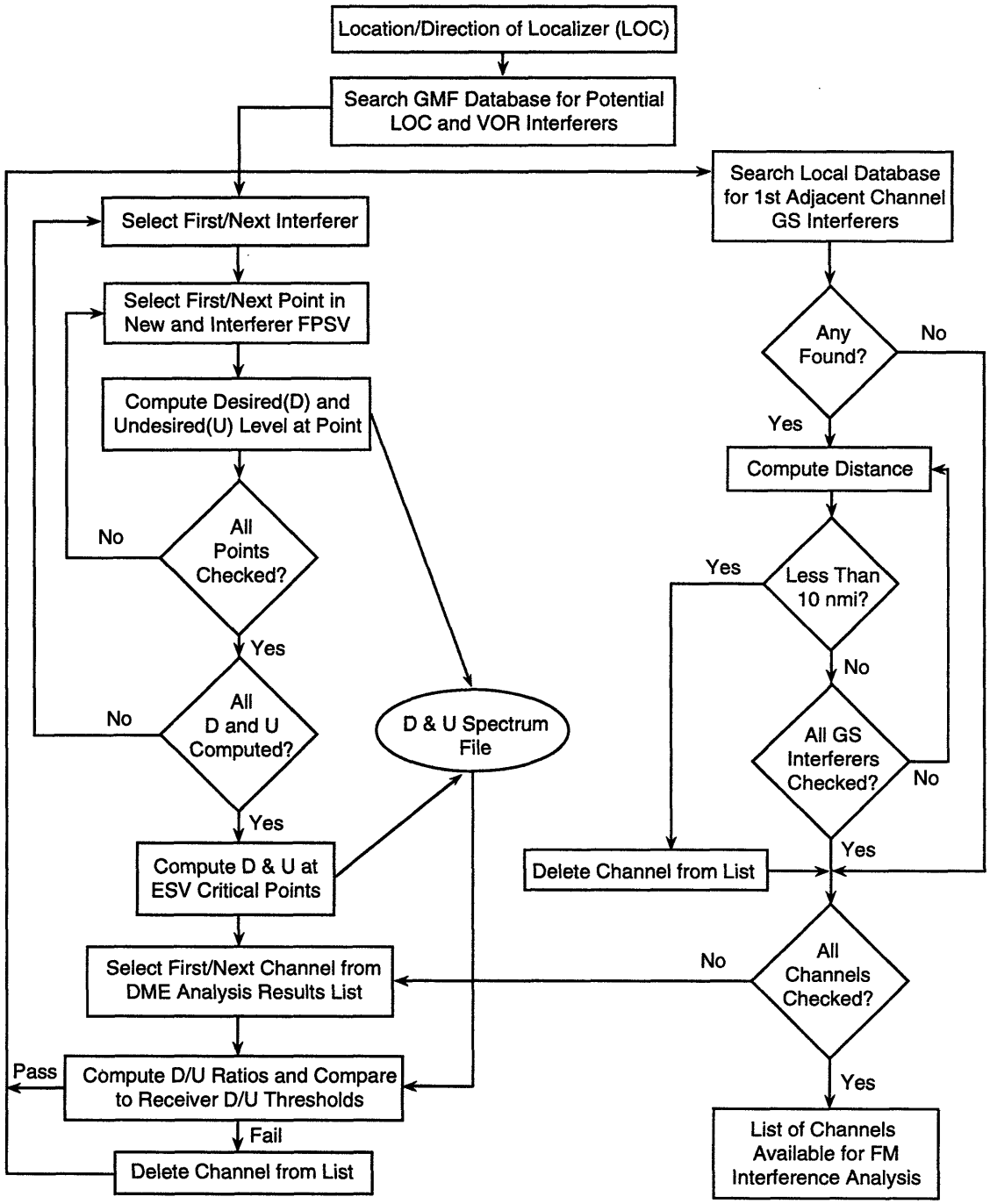

Figure 6.8: Flowchart of the keyhole analysis.

The interfering signal level (U) is computed at selected points within the localizer's FPSV. These points are scattered inside the FPSV at 0, 5, 10 and 35 degrees from the runway direction at distances of 5, 10, 15, and 18 nmi. The signal calculations are based on the propagation model used by the user as in the keyhole analysis. The FM stations are assumed to have a generic omni-directional radiation pattern in azimuth direction with a gain of 6 dBi. In elevation direction for angles from horizon up to 7 degrees, maximum gain is assumed, from 7 to 80 degrees a 14 dB decrease and for angles above 80 degrees a 20 dB decrease is assumed.

The power of different FM stations broadcasting at the same frequency are summed up at each point of the proposed localizer FPSV. For every critical point, 100 signal strengths each corresponding to an FM channel are stored in a temporary file. These signal levels are then checked against different interference mechanisms. The two main interference mechanisms involved are receiver-generated intermodulation (B1) and receiver desensitization (B2).

For B1 interference, all possible 2 and 3 signal third order intermodulation (IMOD) frequencies are computed, which can generate co-channel and adjacent channel interference. The signal strengths for those possible combinations are then compared with the threshold. In addition to the broadcasting signal strengths, the threshold is also a function of the product of the differences between FM frequencies and the localizer proposed frequency. Type B2 interference occurs when the receiver is overloaded by a single or multiple (same frequency) FM broadcasting station. The broadcasting signal levels are compared with the maximum permitted level, which is a function of the FM frequency.

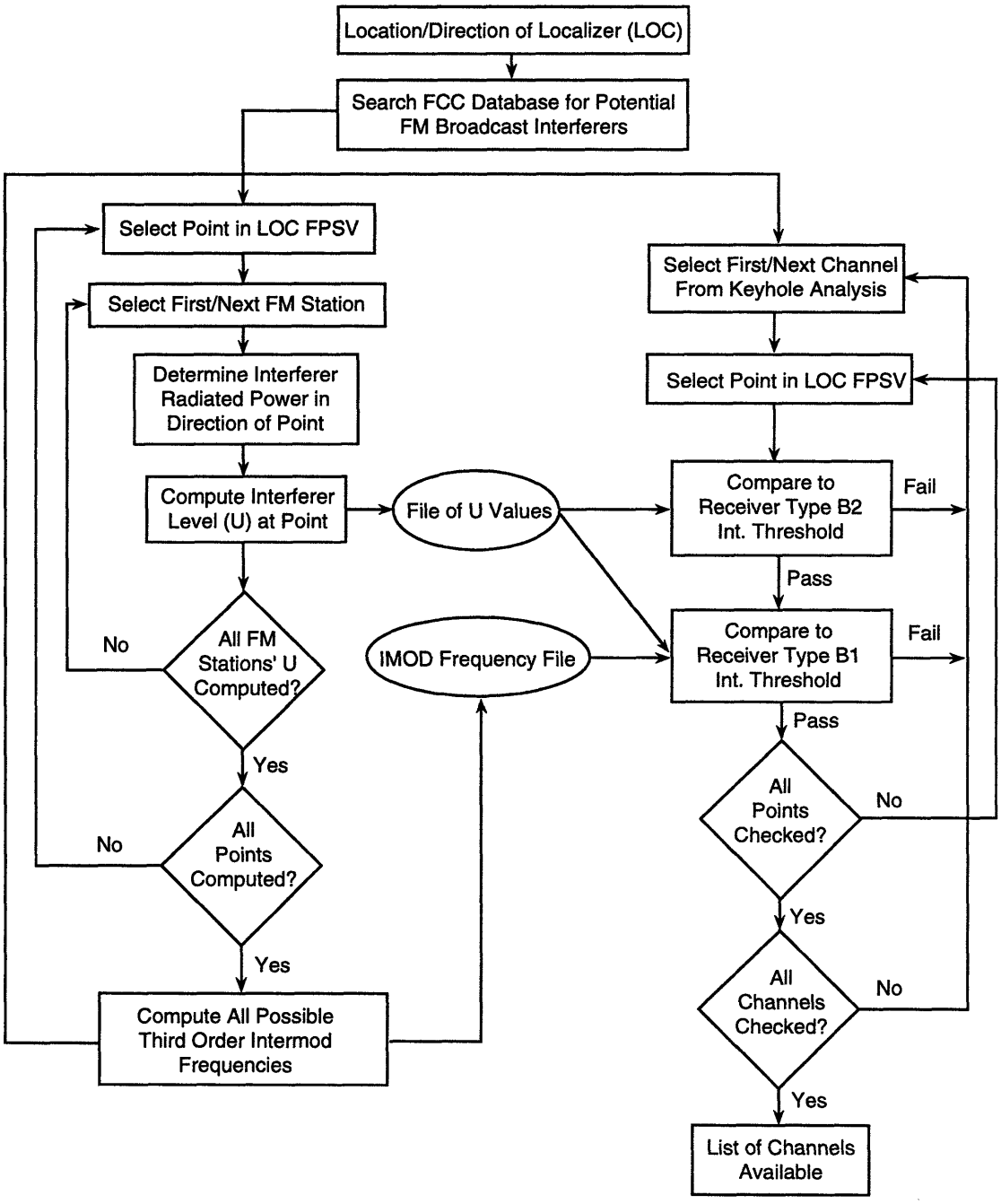

Figure 6.9: Flowchart of the FM interference analysis.

The channels determined to be free of types B1 and B2 interference are considered available for assignment to the proposed runway. They are free of interference from existing ILS facilities and FM broadcast stations and will not interfere with existing ILS facilities.

6.3.4 Channel Capacity Analysis

After all the proposed runways in a given area were analyzed through the above procedure, the corresponding allowable frequency lists will be available for the channel capacity analysis. The goal is to obtain a frequency assignment plan for the new proposed runways in the specified area. Since the allowable frequencies were obtained considering each proposed runway separately, some simultaneous assignment combination may not be allowed because of interference between the new sites.

Considering all the possible assignment combinations is impractical when the number of proposed runways and allowable frequencies is large. There are too many choices in determining the sequence of assignment. Hence a scheme is required to minimize the effort in obtaining the most number of assignments. The scheme used in our analysis is described below.

The proposed runway list is sorted according to the number of allowable frequencies in ascending order. The first frequency is assigned to the first runway in the list. The frequencies that may be interfered by this assignment are then identified and eliminated from the corresponding runway. The new list is sorted and the above assignment procedure is repeated until all the frequencies or runways are assigned. The final result is a list of proposed runways that can simultaneously be equipped

with precision landing system.

6.3.5 Case Study

The software EMSALS allows the user to conduct a channel capacity analysis and assign interference–free frequencies to new proposed runway sites. As an example, the New York–Philadelphia region where a high density of runways exist is selected.

A list is established by FAA and the aviation industry in 1988 to project the requirement for precision landing runways in the United States by year 2000. There are 35 runways in this list that are currently without instrument landing approaches and located within 100 nmi distance of New York city or Philadelphia. They are shown with arrows in Figure 6.10. The existing emitters within 225 nmi of these two cities are extracted from the GMF database and considered in the interference analysis with their current frequecies and power levels.

To obtain a list of possible frequencies for each of the new proposed runways, the whole sequence of DME analysis, keyhole analysis, and FM interference analysis is completed. The DME analysis is performed for all the 38 possible channels [68]. This process tests the co-channel and first adjacent channel DME interferences. In the New York–Philadelphia area, the number of frequencies that pass this test ranges from 8 to 20 for the proposed runways. For example in Teterboro runway 19, 10 channels pass the DME test and are available for the keyhole analysis.

The keyhole analysis is performed separately on each of the frequencies that has passed the DME interference test. The proposed localizer is assumed to have a transmitted power of 15 W and a log–periodic dipole antenna with gain of 17 dBi

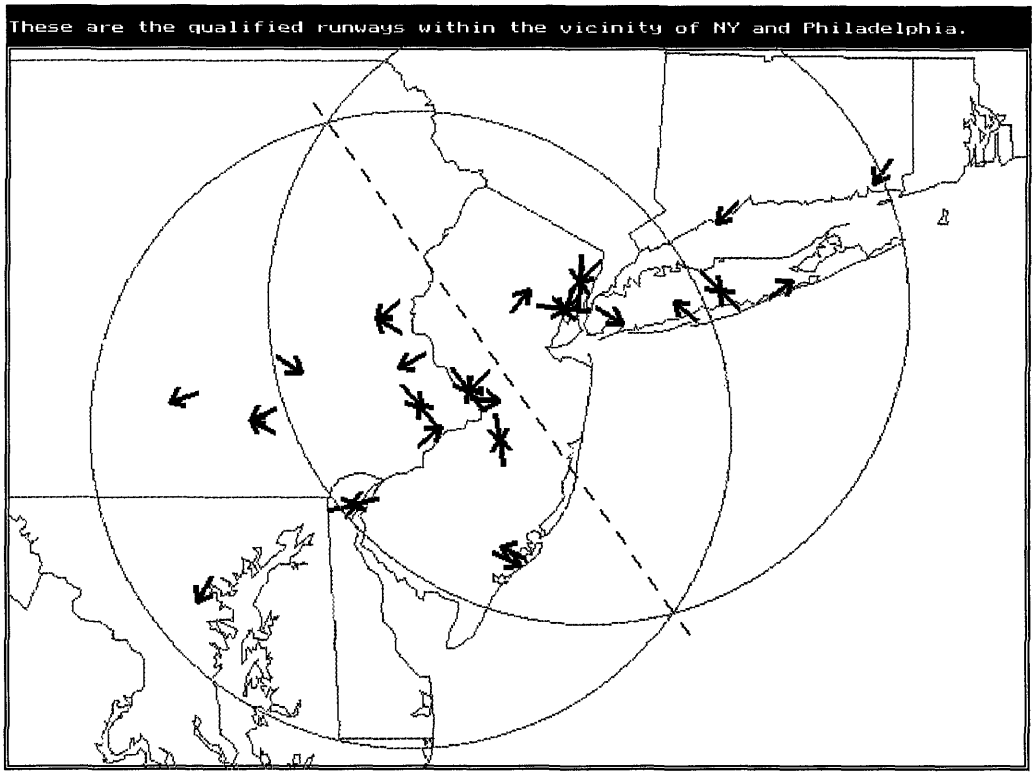

Figure 6.10: The distribution of the 35 proposed runways in the New York–Philadelphia region.

[68]. The results of this analysis are subsequently displayed in a color coded screen, indicating the interference situation. The display consists of the site being analyzed in the center and a map of the surrounding area with all the potential interferers. The site being tested as well as all potential co-channel interferers are displayed with the same color. Other potential interferers are color coded according to their frequency separation with the proposed frequency. Figure 6.11 displays the situation for Teterboro runway 19 with 110.35 MHz as the proposed frequency. The service volumes of existing localizer and VOR emitters with frequencies between 110.20 and 110.50 MHz are being displayed.

The critical points in all of the frequency protected service volumes are denoted by squares. If the D/U at the critical point exceeds the threshold at both altitudes, the point is colored green (shown as light grey squares in Figure 6.11). If at any altitude the D/U is less than the interference threshold, the point is colored red (shown as black squares in Figure 6.11). In the case of interference the signal strengths at the critical points can be investigated by the user. At 110.35 MHz, there are 5 critical points where the D/U is below the threshold and therefore this channel fails the keyhole test.

Performing the keyhole analysis for Teterboro runway 19 for the channels that has passed the DME analysis results in two channels of 109.95 and 111.15 MHz. The emitters in the adjacent frequencies of 111.15 MHz are shown in Figure 6.12. The calculated D/U ratios at all the critical points exceed the threshold value and they are displayed as light grey blocks in the figure.

These two frequencies are then passed to the FM interference analysis where

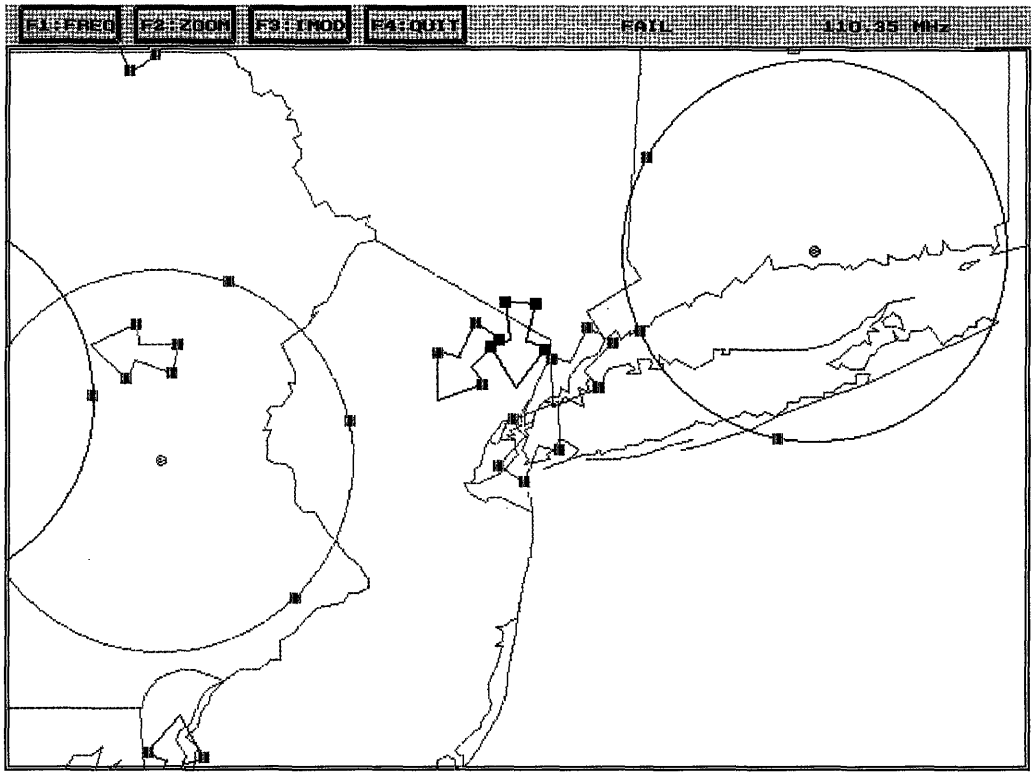

Figure 6.11: Graphical display of the keyhole analysis for Teterboro runway 19 with 110.35 MHz as the proposed frequency.

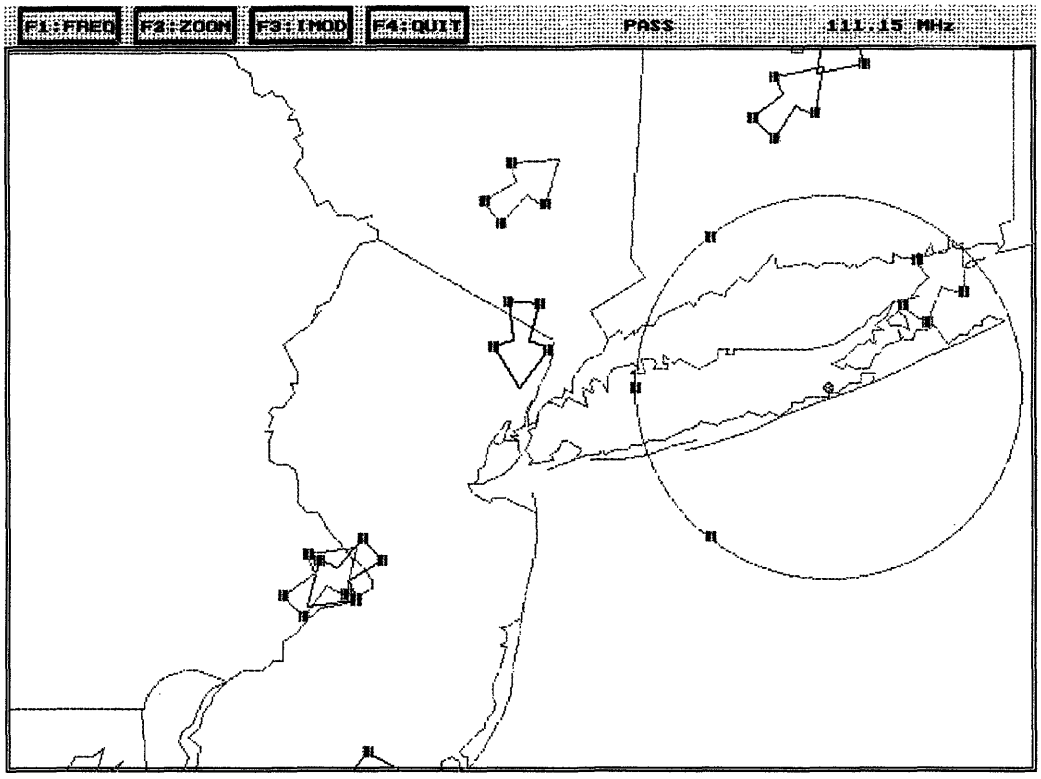

Figure 6.12: Graphical display of the keyhole analysis for Teterboro runway 19 with 111.15 MHz as the proposed frequency.

the intermodulation and desensitization is considered. Both of these channels pass the FM interference tests and can be assigned to the proposed runway. The above sequence of tests are performed separately for each proposed runway and a list of allowable channels is obtained.

Finally, the channel assignment process is performed to finish the channel capacity analysis. The proposed runway list was sorted according to several different ordering schemes. Among the 35 proposed runways in the New York–Philadelphia area, less than 15 runways can be assigned an ILS channel. This shows that ILS substantially fails to meet the precision landing runway requirement in the New York–Philadelphia area.

6.4 Summary

In this chapter the electromagnetic phenomenon in Instrument Landing System was studied. The potential interference sources were identified and located and an electromagnetic propagation model was used to calculate the desired and interfering signal strengths. An interference analyses based upon safety standards were performed, which are consistent with the receiver model. Finally, the interference analysis results for candidate locations were combined to make a channel capacity assessment.

A computer simulation tool, EMSALS, have been developed that performs channel assignment to candidate ILS runways. The analysis in EMSALS is performed in three major steps. First is the DME analysis where the allowable channels are tested against the existing DME stations. Second is the keyhole analysis where the inter-

ferences between localizers, localizer-VOR, and glide slopes are considered. A few critical points in the service volume of the desired facility are selected and examined. The assessment is made by comparing the signal-to-interference power ratio with the safety threshold. Last step is the FM radio stations interference analysis where intermodulation product and desensitization in the receiver is considered.

Chapter 7

Conclusions

In this thesis the effects of electromagnetic interference and coupling in circuits and systems have been analyzed. The coupling phenomena were demonstrated in nonuniform transmission lines and adjacent via structures in microelectronic circuits. Radiation from metallic enclosures with apertures and lined with resistive material was analyzed. Electromagnetic interference phenomenon on a larger scale was studied in the Instrument Landing System receivers, where in–band and out–of–band interference sources were considered.

A method for modeling and analyzing vias in multilayered integrated circuits was presented. The model of via structures was constructed based upon microwave network theory. The whole via structure, consisting of a vertical via passing through different layers and transitions from the microstrip lines and/or striplines to the vertical via, was divided into cascaded subnetworks. The parameters for each subnetwork were obtained from electromagnetic field analysis. Numerical results were presented in the frequency domain and the time domain. Validation of the model was carried out by both measurements and comparison with the finite–difference time–domain (FD–

TD) results. A comparison with the measurements showed good agreement within the frequency range for which the components of experimental model were within specification. The time domain simulation results matched well with the FD–TD results.

The electromagnetic coupling between two adjacent vias in a multilayered integrated circuit was analyzed by means of equivalent magnetic frill array models in combination with the even– and odd–mode approach. Closed–form expressions for the coupled noise on the passive via were derived. The coupling responses in the frequency domain and crosstalk waveforms in the time domain for some multilayered via structures were calculated based on these formulas. A 4–layer experimental model was constructed and measurements made for the transmission, reflection, and coupling responses. The measurements showed good agreement with the calculated results over a frequency range of up to 18 GHz.

A method based on the wave transmission matrix was presented to deal with nonuniform multiconductor transmission line system. This method has not only the ability of handling nonuniformity, but also the advantage of handling nonlinearity in the terminations efficiently. The wave transmission matrix was employed to characterize the multiconductor transmission lines. The nonuniform transmission line was treated as a cascade of many small segments of uniform transmission lines. The formulation for this method and approaches to calculation were discussed in detail. Numerical results were presented and comparison of them with previous work confirms the validity of the method.

The radiation properties of metallic enclosures were studied with a two dimen-

sional FD–TD method. The walls of the enclosure were lined with absorbing material to reduce the fields inside and the contained RF energy, thereby avoiding high Q resonances. The energy leakage from perforations (holes, slots) on the walls was also studied. The radiation properties of these structures were examined by varying the size and position of the holes in the enclosure.

Rectangular enclosures were studied to simulate computer packages. Resonances observed at frequencies of interest were due to modes created in the longer dimension of the enclosure. The lowest power radiated at resonant frequencies was in the examined configurations obtained for the case where the conductive material was placed on the side walls and perforations on the top plate. The optimum position of the perforation depended on the resonant mode and its corresponding field pattern. Also an increase in aperture width lowered the Q of the structure. The position of the source determined the modes excited in the enclosure. For example odd modes were not excited by a source located at the center of the enclosure.

A time domain surface impedance boundary condition for highly conducting sheets in FD–TD was formulated to model the walls of the metallic enclosure. An efficient implementation based on the recursive properties of convolution with exponentials was presented. The reflected fields were simulated and exhibited good agreement with the exact solutions. This model of the conducting sheet is valid for a wide frequency band from very low frequencies up to where the thickness is several skin depths.

In the study of EMI to Instrument Landing system receiver, a computer simulation tool, EMSALS, was developed. It performs quantitative analyses of in–band and

out–of–band electromagnetic interferences. Potential interference sources were identified and located. The desired and interfering signal strengths were calculated with an electromagnetic propagation model. An interference analysis based upon safety standards consistent with the receiver model was performed. Finally, the interference analysis results for various configurations were combined to make a channel capacity assessment.

Interference analysis in EMSALS was performed in three major steps. First was the DME analysis where the allowable channels were tested against the existing DME stations. Second was the keyhole analysis where the interference between localizers, localizer–VOR, and glideslopes was considered. Selected critical points in the service volume of a desired facility were examined. The assessment was made by comparing the signal–to–interference power ratio with the safety threshold. The last step was the analysis of interference with FM radio stations, in which intermodulation product and desensitization in the receiver were considered.

Bibliography

[1] A. Djordjević and T. K. Sarkar, "Computation of Inductance of Simple Vias between Two Striplines above a Ground Plane," *IEEE Trans. Microwave Theory Tech.*, vol. MTT-33, pp. 268-269, Mar. 1985.

[2] A. E. Ruehli, "Equivalent Circuit Models for Three-Dimensional Multiconductor Systems," *IEEE Trans. Microwave Theory Tech.*, vol. MTT-22, pp. 216-221, Mar. 1974.

[3] T. Wang, R. F. Harrington and J. R. Mautz, "Quasi-Static Analysis of a Microstrip Via Through a Hole in a Ground Plane," *IEEE Trans. Microwave Theory Tech.*, vol. MTT-36, pp. 1008-1013, Jun. 1988.

[4] P. Kok and D. De Zutter, "Capacitance of a Circular Symmetric Model of a Via Hole Including Finite Ground Plane Thickness," *IEEE Trans. Microwave Theory Tech.*, vol. MTT-39, pp. 1229-1234, July 1991.

[5] J. P. Quine, H. F. Webster, H. H. Glascock and R. O. Carlson, "Characterization of Via Connections in Silicon Circuit Boards," *IEEE Trans. Microwave Theory Tech.*, vol. MTT-36, pp. 21-27, Jan. 1988.

[6] M. E. Goldfarb and R. A. Pucel, "Modeling Via Hole Grounds in Microstrip," *IEEE Microwave and Guided Wave Letters*, vol. 1, pp. 135-137, June 1991.

[7] K. Nabors, S. Kim and J. White, "Fast Capacitance Extraction of General Three-Dimensional Structures," *IEEE Trans. Microwave Theory Tech.*, vol. MTT-40, pp. 1496-1506, July 1992.

[8] A. E. Ruehli and H. Heeb, "Circuit Models for Three-Dimensional Geometries Including Dielectrics," *IEEE Trans. Microwave Theory Tech.*, vol. MTT-40, pp. 1507-1516, July 1992.

[9] R. E. Collin,"*Field Theory of Guided Waves*," McGraw-Hill Book Company Inc.,

1960.

[10] D. V. Otto,"The Admittance of Cylindrical Antennas Driven from a Coaxial Line," *Radio Science*, vol. 2, no. 9, pp. 1031-1042, 1967.

[11] M. Abramovitz and I. A. Stegun,"*Handbook of Mathematical Functions*," Dover Publications Inc. New York, p. 75, 1965.

[12] K. S. Yee, "Numerical Solution of Initial Boundary Value Problems Involving Maxwell's Equations in Isotropic Media," *IEEE Trans. Antennas Prop.*, vol. AP-14, No.5, pp. 302-307, May 1966.

[13] B. Engquist and A. Majda, "Absorbing Boundary Conditions for the Numerical Simulation of Waves," *Math. of Comp.*, vol. 31, No. 139, pp. 629-651, 1977.

[14] K. H. Lau, "Loss Calculations for Rectangular Coaxial Lines," *IEE Proceedings*, vol. 135, pt. H, No.3, pp. 207-209, June 1988.

[15] J. R. Mosig, "Integral Equation Technique," *Numerical Techniques for Microwave and Millimeter-Wave Passive Structures* , Edited by T. Itoh, New York: Wiley, 1989.

[16] J. A. Kong, "*Electromagnetic Wave Theory*," John Wiley & Sons, Inc., 1990.

[17] G. Arjavalingam and B. Rubin, "Electrical Consideration for Interconnection Inside a Computer," *Fiber and Integrated Optics*, vol. 8, no. 3, pp. 235-244, 1989.

[18] Q. Gu, Y. E. Yang and M. A. Tassoudji, "Modeling and Analysis of Vias in Multilayered Integrated Circuits," *IEEE Trans. Microwave Theory Tech.*, vol. MTT-41, Feb. 1993.

[19] A. G. Williamson, "Analysis and Modeling of a Coaxial-Line Rectangular-Waveguide Junction," *IEE Proceedings*, vol. 129, pt H, no. 5, pp. 262-270, Oct. 1982.

[20] F. Y. Chang, "Transient analysis of lossless coupled transmission lines in a non-homogeneous dielectric medium," *IEEE Trans. Microwave Theory Tech.*, vol. MTT-18, pp. 616-626, Sept. 1970.

[21] M. K. Krage and G. I. Haddad, "Characteristics of coupled microstrip transmission lines with inhomogeneous dielectrics," *IEEE Trans. Microwave Theory Tech.*, vol. MTT-20, pp. 678-688, Oct. 1972.

[22] Y. E. Yang, J. A. Kong, and Q. Gu, "Time-domain perturbational analysis of nonuniformly coupled transmission lines," *IEEE Trans. Microwave Theory Tech.*, vol. MTT-33, pp. 1120-1130, Nov. 1985.

[23] J. E. Schutt-Aine and R. Mittra, "Analysis of pulse propagation in coupled transmission lines," *IEEE Trans. Circuit Syst.*, vol. CAS-32, pp. 1214-1219, Dec. 1985.

[24] Q. Gu, J. A. Kong, and Y. E. Yang, "Time domain analysis of nonuniformly coupled line systems," *J. Electromag. Waves Appl.*, vol. 1, pp. 109-132, 1987.

[25] H. You and M. Soma, "Crosstalk analysis of interconnection lines and packages in high-speed integrated circuits," *IEEE Trans. Circuit Syst.*, vol. CAS-37, pp. 1019-1026, Aug. 1990.

[26] A. R. Djordević, T. K. Sarkar, and R. F. Harrington, "Time-domain response of multiconductor transmission lines," *Proc. IEEE*, vol. 75, pp743-764, June 1987.

[27] A. J. Groudis and C. S. Chang, "Coupled lossy transmission line characterization and simulation," *IBM J. Res. Develop.*, vol. 25, pp. 25-41, Jan. 1981

[28] Q. Gu and J. A. Kong, "Transient analysis of single and coupled lines with capacitively-loaded junctions," *IEEE Trans. Microwave Theory Tech.*, vol. MTT-34, pp. 952-964, Sept. 1986.

[29] J. E. Schutt-Aine and R. Mittra, "Nonlinear transient analysis of coupled transmission lines," *IEEE Trans. Circuit Syst.*, vol. CAS-36, pp. 959-967, July 1989.

[30] J. F. Mao and Z. F. Li, "Analysis of the time response of multiconductor transmission lines with frequency-dependent losses by the method of convolution characteristics," *IEEE Trans. Microwave Theory Tech.*, vol. MTT-40, pp. 637-644, Apr. 1992.

[31] L. Carin and K. J. Webb, "An equivalent circuit model for terminated hybrid-mode multiconductor transmission lines," *IEEE Trans. Microwave Theory Tech.*, vol. MTT-37, pp. 1784-1793, Nov. 1989.

[32] G. Ghione, I. Maio, and G. Vecchi, "Modeling of multiconductor buses and analysis of crosstalk, propagation delay and pulse distortion in high-speed GaAs logic circuits," *IEEE Trans. Microwave Theory Tech.*, vol. MTT-37, pp. 445-456, Mar. 1989.

[33] J. P. Gilb and C. A. Balanis, "Pulse distortion on multilayer coupled microstrip lines," *IEEE Trans. Microwave Theory Tech.*, vol. MTT-37, pp. 1620-1628, Oct. 1989.

[34] R. Wang and O. Wing, "A circuit model of a system of VLSI interconnects for time response computation," *IEEE Trans. Microwave Theory Tech.*, vol. MTT-39, pp. 688-693, Apr. 1991.

[35] T. Itoh and R. Mittra, "Spectral-domain approach for calculating the dispersion characteristics of microstrip lines," *IEEE Trans. Microwave Theory Tech.*, vol. MTT-21, pp. 496-499, 1973.

[36] C. Wei, R.F. Harrington, J.R. Mautz, and T.K. Sarkar, "Multiconductor transmission lines in multilayered dielectric media," *IEEE Trans. Microwave Theory Tech.*, vol. MTT-32, pp. 439-450, Apr. 1984.

[37] E. G. Farr, C. H. Chan, and R. Mittra, "A frequency-dependent coupled-mode analysis of multiconductor microstrip lines with application to VLSI interconnection problems," *IEEE Trans. Microwave Theory Tech.*, vol. MTT-34, pp. 307-310, Feb. 1986.

[38] F. Medina and M. Horno, "Capacitance and inductance matrices for microstrip structures in multilayered anisotropic dielectrics," *IEEE Trans. Microwave Theory Tech.*, vol. MTT-35, pp. 1002-1008, Nov. 1987.

[39] N. Fache and D. De Zutter, "Rigorous Full-Wave Space-Domain Solution for Dispersive Microstrip Lines," *IEEE Trans. Microwave Theory Tech.*, vol. MTT-36, pp. 731-737, Apr. 1988.

[40] F. Olyslager, N. Fache, and D. De Zutter, "New Fast and Accurate Line Parameter Calculation of General Multiconductor Transmission Lines in Multilayered Media," *IEEE Trans. Microwave Theory Tech.*, vol. MTT-39, pp. 901-909, June 1991.

[41] A. J. Groudis, "Transient analysis of uniform resistive transmission lines in a homogeneous medium," *IBM J. Res. Develop.*, vol. 23, pp. 675-681, Nov. 1979.

[42] F. Y. Chang, "Waveform relaxation analysis of RLCG transmission lines," *IEEE Trans. Circuit Syst.*, vol. CAS-37, pp. 1394-1415, Nov. 1990.

[43] C. R. Paul, "Useful matrix chain parameter identities for the analysis of multiconductor transmission lines," *IEEE Trans. Microwave Theory Tech.*, vol. MTT-23,

pp. 756-760, Sept. 1975.

[44] A. R. Djordjević, T. K. Sarkar, and R. F. Harrington, "Analysis of lossy transmission lines with arbitrary nonlinear terminal networks," *IEEE Trans. Microwave Theory Tech.*, vol. MTT-34, pp. 640-666, June 1986.

[45] J. E. Schutt-Aine and R. Mittra, "Scattering parameter transient analysis of transmission lines loaded with nonlinear terminations," *IEEE Trans. Microwave Theory Tech.*, vol. MTT-36, pp. 529-536, Mar. 1988.

[46] Q. Gu, Y. E. Yang, and J. A. Kong, "Transient analysis of frequency-dependent transmission line systems terminated with nonlinear loads," *Journal of Electromagnetic Waves and Applications*, vol. 3, No. 3, pp. 183-197, 1989.

[47] Q. Gu, D. M. Sheen, and S. M. Ali, "Analysis of transients in frequency-dependent interconnections and planar circuits with nonlinear loads," *IEE Proc. Pt. H*, vol. 139, pp. 38-44, Feb. 1992.

[48] J. F. Mao and Z. F. Li, "Analysis of the time response of nonuniform multiconductor transmission lines with a method of equivalent cascaded network chain," *IEEE Trans. Microwave Theory Tech.*, vol. MTT-40, pp. 948-954, May 1992.

[49] J. E. Adair and G. I. Haddad, "Coupled-mode analysis of non-uniform coupled transmission lines," *IEEE Trans. Microwave Theory Tech.*, vol. MTT-17, pp. 746-752, Oct. 1969.

[50] O. A. Palusinki and A. Lee, "Analysis of transients in nonuniform and uniform multiconductor transmission lines," *IEEE Trans. Microwave Theory Tech.*, vol. MTT-37, pp. 127-138, Jan. 1989.

[51] S. Barnett, *Matrix Method for Engineers and Scientists,* McGRAW-HILL Book Company (UK) Limited, 1979.

[52] G. W. Pan, G. J. Wunsch and B. K. Gilbert, "Frequency-domain analysis of coupled nonuniform transmission lines using chebyshev pseudo-spatial techniques," *IEEE Trans. Microwave Theory Tech.*, vol. MTT-40, pp. 2025-2033, Nov. 1992.

[53] N. Orhanovic, V. K. Tripathi and P. Wang, "Time domain simulation of uniform and nonuniform multiconductor lossy lines by the method of characteristics," *1990 IEEE MTT-S Digest*, pp. 1191-1194, June 1990.

[54] W. T. Weeks, "Calculation of coefficients of capacitance of multiconductor transmission lines in the presence of a dielectric interface," *IEEE Trans. Microwave Theory Tech.*, vol. MTT-18, pp. 35-43, Jan. 1970.

[55] A. Taflove and K. R. Umashankar, "The Finite-Difference Time-Domain Method for Numerical Modeling of Electromagnetic Wave Interactions," *Electromagnetics,* vol. 10, no. 1-2, 105-126, 1990.

[56] A. Taflove and M. E. Brodwin, "Numerical solution of steady-state electromagnetic scattering problems using the time-dependent Maxwell's equations," *IEEE Trans. Microwave Theory Tech.*, vol. MTT-23, pp. 623-630, Aug. 1975.

[57] G. Mur, "Absorbing boundary conditions for the finite difference approximation of the time domain electromagnetic field equations," *IEEE Trans. Electromagnetic Comp.*, vol. EMC-23, pp. 377-382, Nov. 1981.

[58] C. F. Lee, K. Li, S. Y. Poh, R. T. Shin and J. A. Kong "Electromagnetic Radiation from a VLSI Package and Heatsink Configuration," *IEEE International Symposium on Electromagnetic Compatibility Symposium Record,* Cherry Hill, NJ, August 12-16, 1991.

[59] B. Engquist and A. Majda, "Absorbing Boundary Conditions for the Numerical Simulation of Waves," *Math. Comp.*, Vol. 31, No. 139, pp. 629-651., 1977

[60] K. Li, M. A. Tassoudji, R. T. Shin and J. A. Kong, "Simulation of Electromagnetic Radiation and Scattering Using a Finite Difference-Time Domain Technique," *Computer Applications in Engineering Education.*, Vol. 1, No. 1, pp. 45-63, 1992.

[61] J. G. Maloney, G. S. Smith, "The Use of Surface Impedance Concepts in the Finite Diference Time Domain Method," *IEEE Trans. Antennas Prop.*, vol. 40, pp. 38-48, Jan. 1992

[62] J. G. Maloney, G. S. Smith, "The Efficient Modeling of Thin Material Sheets in the Finite-Difference Time-Domain (FDTD) Method," *IEEE Trans. Antennas Prop.*, vol. 40, pp. 323-330, March 1992.

[63] J. G. Maloney, G. S. Smith, "A Comparison of Methods for Modeling Electrically Thin Dielectric and Conducting Sheets in the Finite-Difference Time-Domain Method," *IEEE Trans. Antennas Prop.*, vol. 41, pp. 690-694, May 1992.

[64] L. K. Wu, L. T. Han, "Implementation and Application of Resistive Sheet Boundary Condition in the finite-difference time-domain method," *IEEE Trans. Antennas Prop.*, vol 40., pp. 628-633, June 1992.

[65] R. J. Luebbers, K. Kunz, "FDTD modeling of Thin Impedance Sheets," *IEEE Trans. Antennas Prop.*, vol. 40, pp. 349-351, March 1992.

[66] R. J. Luebbers, "Lossy Dielectrics in FDTD," *IEEE Trans. Antennas Prop.*, vol. 41, pp. 1586-1588, Nov. 1993.

[67] Y. E. Yang et al. *Frequency Management Assessment,* Project Final Report for U.S. Dept. of Transportation Contract No. DTRS-57-88-C-00078, TTD13, Center for Electromagnetic Theory and Applications, Research Laboratory of Electronics, Center for Transportation Studies, M.I.T., Cambridge, MA, 1992.

[68] *Spectrum Management Regulations and Procedures Manual*, Federal Aviation Administration, Order 6050.32, U.S. Department of Transportation, September 1987.

[69] Report 929-1 from *Recommendations and Reports of the CCIR, 1986*, Vol. VIII-3 "Mobile Satellite Services (Aeronautical, Land, Maritime, Mobile and Radionavigation), Aeronautical Mobile Service," International Telecommunication Union (ITU), Geneva, 1986.

[70] G. D. Gierhart and M. E. Johnson, *The IF–77 Electromagnetic Wave Propagation Model*, FAA Technical Report DOT/FAA/ES–8313, September 1983.

[71] M. E. Johnson and G. D. Gierhart,*Applications Guide: Propagation and Interference Analysis Computer Programs (0.1 to 20 GHz)*, FAA Technical Report FAA–RD–77–60, March 1978.

[72] *International Standards, Recommended Practices and Procedures for Air Navigation Services – Aeronautical Telecommunications*, International Civil Aviation Organization (ICAO), Annex 10 to the Convention on International Civil Aviation, Volume I, Fourth Edition of Volume I, April 1985.

[73] A. G. Longley and P. L. Rice, *"Prediction of tropospheric radio transmission loss over irregular terrain, a computer method,"* ESSA Tech. Rept. ERL 79-ITS 67 (1968).

[74] D. E. Kerr, *Propagation of short radio waves*, Boston Tech. Pub.,Inc., Lexington, 1964.

[75] P. L. Rice, A. G. Longley, K. A. Norton, and A. P. Barsis, " Transmission loss predictions for tropospheric communication circuits," NBS. Tech. Note 101, I and II (1967).

[76] CCIR, Tropospheric wave transmission loss prediction, Int. Radio Consultative Committee Study, (1962).

[77] J. J. Tary, R. R. Bergman and G. D. Gierhart, GOES telecommunication study-197, OT Telecomm. Tech. Memo OT TM-64 (1971).

[78] Minimum Performance Standards - Airborne ILS Localizer Receiving Equipment, Radio Technical Commission for Aeronautics, Document DO-131, December 15, 1965.

[79] Minimum Performance Standards - Airborne ILS Localizer Receiving Equipment, Radio Technical Commission for Aeronautics, Document DO-131A, December 15, 1965.

[80] Minimum Performance Standards for Airborne ILS Localizer Receiving Equipment Operating within the Radio Frequency Range of 108 - 112 MHz, Radio Technical Commission for Aeronautics, Document DO-195, November 17, 1986.

[81] K. Bose, *Aviation Electronics*, Howard W. Sams Co., Inc., New York, 1970.

[82] *Technical Reference Guide to the Airspace Analysis Model, Version 3.05,* Federal Aviation Administration, Spectrum Engineering Division, ASM-500, May 1989.

[83] W. D. Phipps, *Users Manual for the Airspace Mathematical Model, Version 3.01,* OU/AEC 26-88TM00006/10-3, Avionics Engineering Center, Ohio University, Athens, Ohio, June 1988.

[84] *General Aviation Activity and Avionics Survey,* Center for Transportation Information, U.S. Department of Transportation, FAA-MS-87-5, December 1987.

[85] *General Aviation Equipment Survey,* Aircraft Owners and Pilots Association, 1988.

[86] *Report of the Future System Design Working Group,* U.S. Department of Transportation, 1990.

[87] S. Ayasli, "SEKE: A computer model for low altitude radar propagation over irregular terrain," *IEEE Trans. Antennas Prop.*, vol. AP-34, no. 8, pp. 1013-1023, August 1986.